Title

TOTAL AND DIFFERENTIAL CROSS SECTIONS FOR n-p u>nn FROM THRESHOLD TO 1300 MeV

Permalink

https://escholarship.org/uc/item/1879d86m

Author

Richards, Walter Bruce.

Publication Date

1965-11-17

UCRL-16195

University of California

Ernest O. Lawrence Radiation Laboratory

TOTAL AND DIFFERENTIAL CROSS SECTION FOR $\pi^- p \rightarrow \eta n$ FROM THRESHOLD TO 1300 MeV

Berkeley, California

DISCLAIMER

Research and Development

UCRL-16195

UNIVERSITY OF CALIFORNIA

Lawrence Radiation Laboratory
Berkeley, California

AEC Contract No. W-7405-eng-48

TOTAL AND DIFFERENTIAL CROSS SECTIONS FOR $\pi^-p \rightarrow \eta n$ FROM THRESHOLD TO 1300 MeV

Walter Bruce Richards
(Ph. D. Thesis)

November 17, 1965

Contents

II. Experimental Method and Equipment

Appendices

TOTAL AND DIFFERENTIAL CROSS SECTIONS FOR $\pi^- p \rightarrow \eta n$ FROM THRESHOLD TO 1300 MeV*

Walter Bruce Richards

Lawrence Radiation Laboratory
University of California
Berkeley, California

November 17, 1965

ABSTRACT

The reaction $\pi^- p \rightarrow \eta n$ has been observed through the decay mode $\eta \rightarrow 2\gamma$ at T_{π^-} = 592, 655, 704, 875, 975, 1117, and 1300 MeV. Details are given of the detection apparatus, a cubic array of six steel-plate spark chambers, completely surrounding a liquid-hydrogen target. Showers produced in the spark chambers by decay photons were recorded photographically for analysis. We identified events attributed to the decay of an η by the large c.m. opening angle between the two photons.

We have calculated the total cross section for η production, which is proportional to the number of events under the peak at large angles in the opening angle distribution. This rises steeply from threshold to a maximum of about 3 mb at 650 MeV, and then falls gradually to about 0.75 mb at 1300 MeV.

The differential cross section was obtained by taking the coefficients of a Legendre polynomial fit to the angular distribution of bisectors of selected two shower events, and converting them to the coefficients of the η c.m. angular distribution. The differential cross section is found to be isotropic at 592 MeV, to require terms through P_2 between 655 MeV and 975 MeV, and to have a forward peak fit by terms through P_3 at 1117 MeV and through P_4 at 1300 MeV.

It is suggested that production at threshold is predominantly through an S state, with some P_1 and D_3 waves entering by 655 MeV. Speculation about a possible enhancement in the P_3 wave at 1100 MeV is given. We suggest that all of the absorption in the S_{11} π^--N state can be explained by the η production, and briefly discuss the nature of the η-N S-wave interaction at the η threshold.

I. INTRODUCTION

One of the most unexpected features of contemporary high energy physics research is the "population explosion" that has taken place in the sub-nuclear particle world in the last two decades. With the first experimental observation of π mesons in 1947,[1] the list of particles slowly began to grow, and the rate of expansion increased after accelerators capable of producing particles in the GeV energy region went into operation at Berkeley and Brookhaven in 1953. In 1957 it was possible to make a tidy list of thirty objects which could qualify for the title of "elementary particle." Today, in view of the fact that the same list includes almost 100 particles, the meaning of the words "elementary particle" has become unclear.[2]

This explosion has confronted the theoretical physicist with a situation of ever-increasing complexity, which still awaits a breakthrough in understanding. Experimental physicists have been furnished a rich variety of objects to examine, with the aim of determining their properties and revealing the relationships which are present among them.

First observed in 1961, the η meson is the most recently discovered meson which is stable against decay by the strong interaction. A survey of the experiments from which the quantum numbers of the η were deduced to be

$$J^P I^G = 0^- 0^+$$

may be found in Ref. 3. Originally the η was seen as a peak at 550 MeV in the effective mass spectrum of three pions from the reaction[4]

$$\pi^+ d \rightarrow p_s p \; \pi^+ \pi^- \pi^0 .$$

A radiative decay mode, reported at the 1962 CERN conference,[5] was soon established to be $\eta \rightarrow 2\gamma$ by analysis of heavy liquid bubble-chamber film from two different experiments. This gave conclusive evidence that the C-parity of the η is +1, and that it has even spin, probably 0.

The most straightforward of the two experiments mentioned above involved measurement of the curvature of electron-positron pair tracks in a bubble chamber magnetic field.[6] Each electron-positron pair was produced by materialization of one of the γ-rays from the decay of a neutral meson in the reaction

$$\pi^- p \rightarrow X^0 n$$

where

$$X^0 \rightarrow 2\gamma .$$

Direct measurement of the energy of all four resulting leptons permitted direct calculation of the effective mass of the two γ-rays. Two peaks were found, one at the mass of the π^0 and one at the mass of the η.

This experiment, however, was only a confirmation of the results of an earlier bubble chamber experiment, which had also shown that the η meson has a 2γ decay mode.[7] Since the method of identification of the η among the events in this bubble chamber film was the same as is used in the present experiment, it will be described in some detail.

Again, the class of reactions to be considered is

$$\pi^- p \rightarrow X^0 n \tag{1}$$

where the X^0 subsequently decays into two γ-rays. The principal reaction which takes place is, of course, the charge exchange reaction

$\pi^- p \rightarrow \pi^0 n$. For any X^0, if the reaction is studied in the π-p center-of-mass system, the neutral meson has a fixed velocity. From kinematical considerations it then follows quite simply that in the center-of-mass system the angle subtended by the two decay photons, called the opening angle, Φ, follows a probability distribution given by the following equation:

$$\frac{dn}{d\Phi} = \frac{\cos \Phi/2}{2\beta_{X^0}\gamma^2_{X^0} \sin^2\Phi/2 \sqrt{\beta^2_{X^0} - \cos^2 \Phi/2}} , \qquad (2)$$

where β_{X^0} is the velocity of X^0 in units of the velocity of light, and

$$\gamma_{X^0} = \frac{1}{\sqrt{1 - \beta_{X^0}{}^2}} .^{8}$$

Inspection of the denominator shows that the distribution has an infinite peak at a minimum opening angle for which

$$\cos \left(\frac{\Phi \text{ min}}{2}\right) = \beta_{X^0} . \qquad (3)$$

In Fig. 1 is a graph of the theoretical distribution function. The other curve superimposed is the same distribution function, but folded into it are a typical angular resolution of measurement and the effect of the momentum spread of the incoming beam as determined in this experiment; therefore, it is broader and lower.

In the center-of-mass of reaction (1), the energy available is fixed by the kinetic energy of the incoming pion, independently of the mass of X^0. However, the partition of this available energy between X^0

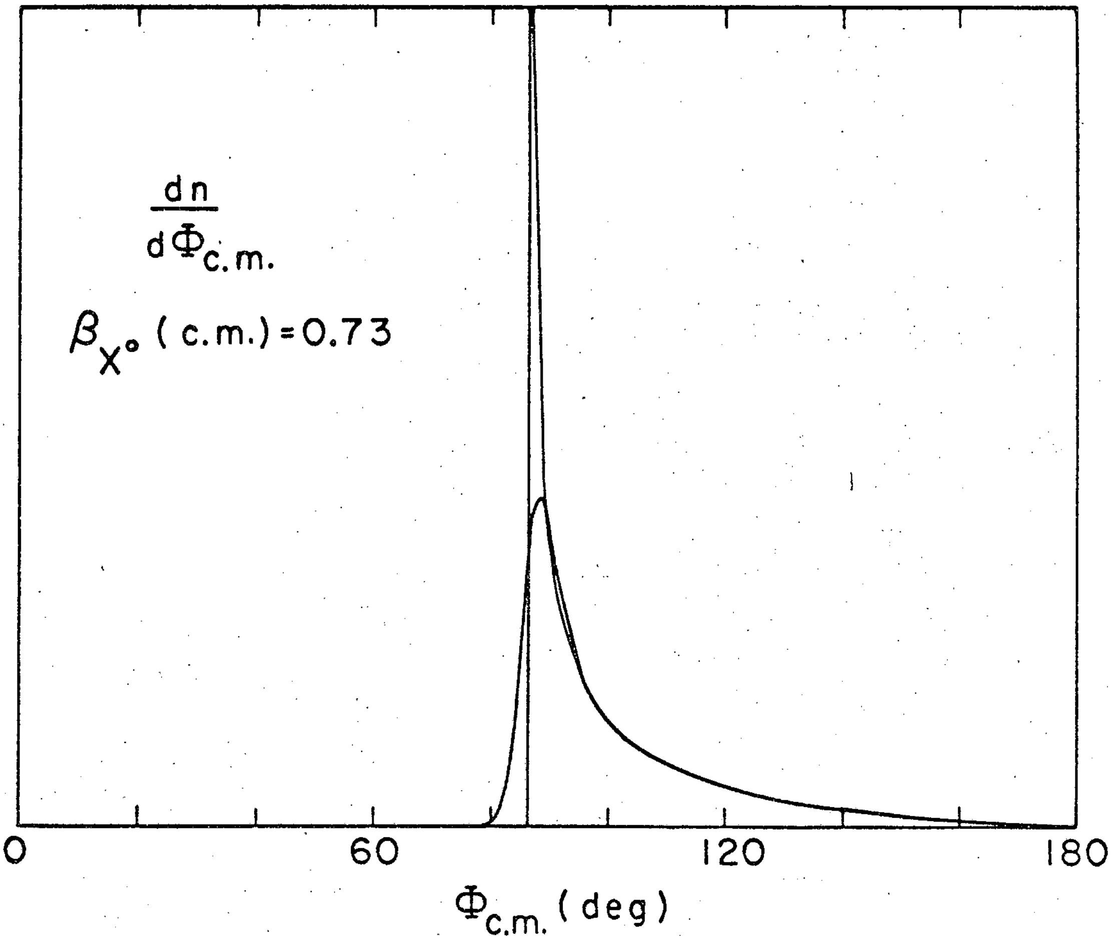

MUB-7411

Figure 1. Theoretical opening angle curves, showing one with a typical resolution function folded into it.

and the neutron in the final state--and hence the center-of-mass velocity of the X^0--does depend on the mass of the neutral meson. Roughly speaking, the greater the mass of the X^0, the more energy is taken up by rest mass and the less by its kinetic energy, or velocity. This implies that an X^0 of large mass will yield photons according to the distribution function (2) whose minimum opening angle is quite large, while an X^0 of small mass gives photons with a smaller opening angle.

Thus, if in an experiment there are several possible reactions of the type

$$\pi^- p \rightarrow X_1^0 n, \qquad X_1^0 \rightarrow 2\gamma;$$

$$\pi^- p \rightarrow X_2^0 n, \qquad X_2^0 \rightarrow 2\gamma;$$

where

$$m_{X_1^0} \neq m_{X_2^0},$$

the observed center-of-mass distribution of opening angles is a superposition of peaks, whose locations give the masses of the neutral meson, and whose relative magnitudes give the branching ratios among the different final states. In Fig. 2 an opening angle distribution from the present experiment is shown, where the peak due to π^0 decay is above the minimum at 30 deg, and the peak due to η decay is at 130 deg.

Turning now from the general discussion of the η meson, its background and how it may be observed, I would like to describe briefly some of the reasons why this experimental investigation was undertaken.[9]

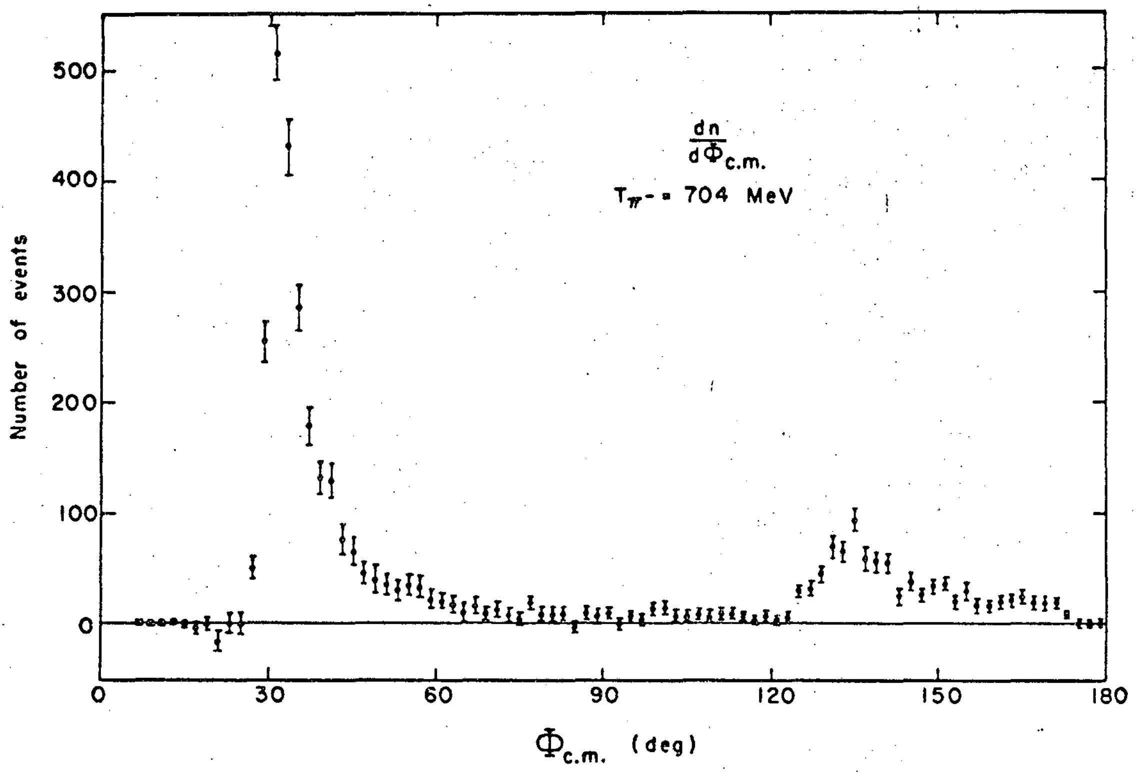

MUB-7410

Figure 2. A typical opening angle distribution from this experiment.

Prior to the performance of the present experiment in the summer and fall of 1963, there existed only a few isolated measurements of the total production cross section of the η meson in various reactions, and no significant differential cross section determinations at all. Peculiar behavior had been noticed in the total cross section in the reaction

$$K^-p \rightarrow \Lambda\eta, \ \eta \rightarrow \text{neutrals}$$

which was (500 ± 150) μb, 20 MeV above threshold in the center-of-mass system, and then dropped to (150 ± 100) μb, only 60 MeV above threshold.[10] This type of behavior is to be expected more from a composite system than from an elementary particle, and yet the substantial decay mode $\eta \rightarrow \pi^+\pi^-\pi^0$, which is forbidden by G-parity, seems to indicate the opposite. In view of this surprising observation, a systematic set of measurements of the production cross section in some other channel seemed important.

Another question concerns the interaction of the η meson with nucleons. Figure 3 shows the prominent resonances in the cross section of the π-N system in the isotopic spin 1/2 state at energies just above the threshold for η production.[11] Except for isotopic spin, and hence G parity, the η has the same quantum numbers as the pion. It would therefore seem quite fruitful to study the reaction $\pi^-p \rightarrow \eta n$ in the same energy region to see if the total η production cross section also passes through resonances. Measurement of the differential cross section in this region would considerably add to the knowledge of the production process. If the η cross section shares the same resonances, it would indicate that the excited nucleon isobar states can also decay

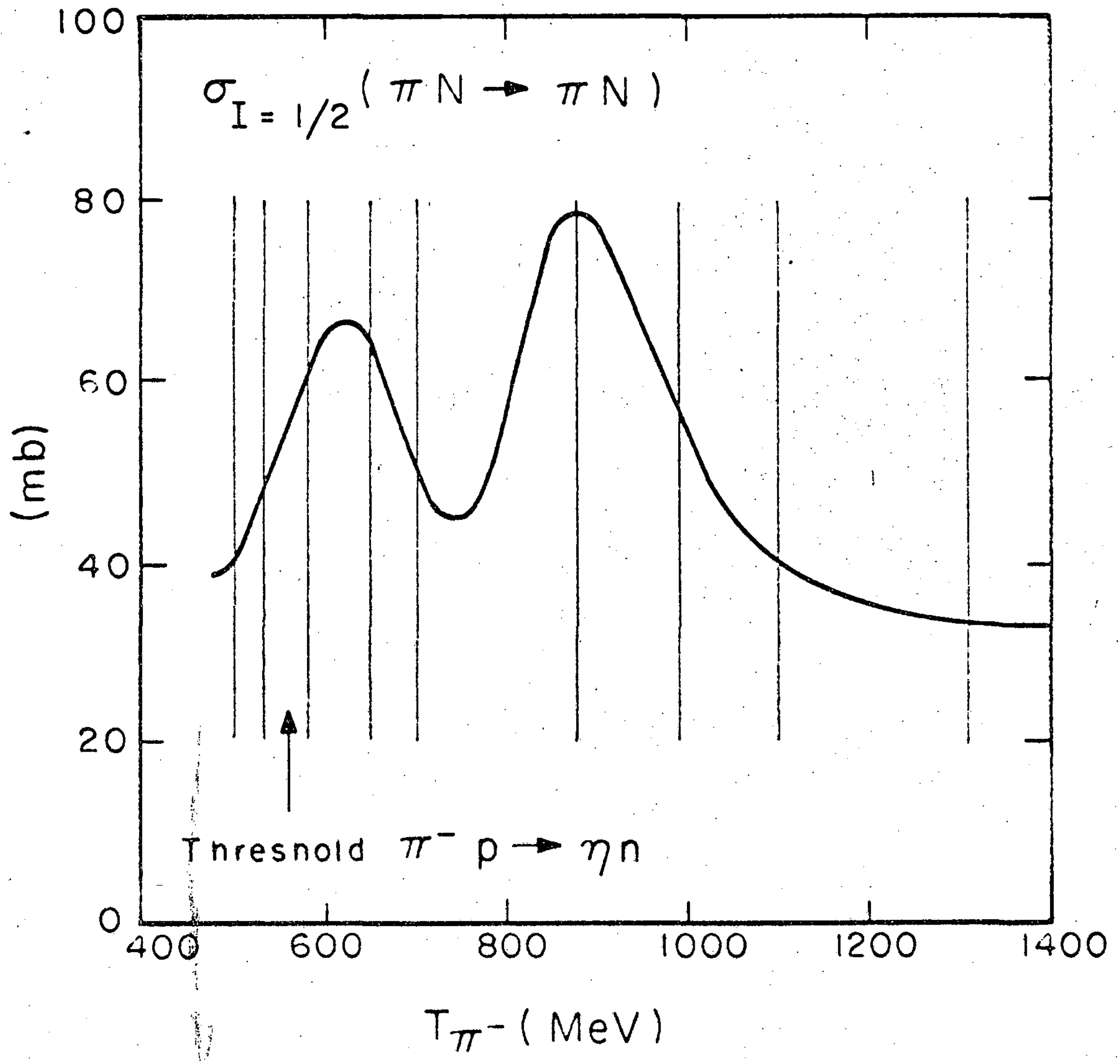

MU-36523

Figure 3. The total cross section for π-N scattering in the isotopic spin 1/2 state. The vertical lines indicate the energies at which data were taken in this experiment.

through an η particle. In view of the various theories of elementary particles based on symmetry principles, measurements of this kind are particularly important.

Finally, it was hoped that systematic study of the η-N interaction could give some insight into phenomena of π-N elastic scattering around 600 MeV. Since π-N scattering at this energy is highly absorptive, quantitative phase shift analyses of the important angular momentum states have been difficult and yield conflicting results.[12] To give an example, different workers have fit the elastic scattering data in this energy region with anywhere from 0 to 3 resonant amplitudes.

It follows from simple resonance theory that any S-matrix pole associated with a π-N resonance must be shared with all communicating channels, although there is no guarantee that the coupling strength will be the same.[13] Because the major two-body channel which communicates with the I-spin 1/2 π-N system around 600 MeV is η-N, it is possible that the existence and position of the resonances could be better analyzed in the inelastic η-N channel. Also, to reverse the argument, it might be revealed that an enhancement in the π-N cross section is fundamentally a reflection of a strong interaction in the η-N system.

For all of the above reasons, then, this research was begun. An experiment was planned in which neutral final states from π-p collisions were observed at nine energies in the region of the 600 and 900 MeV resonances. Steel plate spark chambers completely surrounding a liquid hydrogen target were used as detectors. The photons from the decay of the neutral mesons in the final state produced cascade showers in the steel plates, which could then be recorded photographically for analysis. The data on the ordinary charge exchange reaction $\pi^- p \rightarrow \pi^0 n$ is reported elsewhere,[14] while the analysis of the reaction $\pi^- p \rightarrow \eta n$ is the subject of this thesis.

In the next section the experimental method and apparatus used to observe the η meson will be explained, and following that will be a description of the data analysis and the results.

II. EXPERIMENTAL METHOD AND EQUIPMENT

A. General

The arrangement of the experimental apparatus is shown in Fig. 4. Pions produced in the Bevatron of the Lawrence Radiation Laboratory were conveyed to a liquid hydrogen target by a system of magnets which could be tuned to pass particles at any of nine different momenta. The kinetic energy range of the pions was from 500 to 1300 MeV, so that the behavior of the cross sections could be studied in the general region of the 600 and 900 MeV resonances.

A triple coincidence of signals from three monitor counters placed along the beam indicated that a negatively charged particle had entered the target. To count the number of these incoming particles, an electronic scalar was used. Placed around the hydrogen target on the downstream side was another group of nine counters, which served to determine if any of the particles emerging from the target after the interaction were charged. Since the experiment was designed to study only the neutral final states, this group of nine counters was put in anti-coincidence with the monitor counters, and the product was used to signal the occurrence of an acceptable neutral event.

Typical neutral final states selected by the anticounters were

$$\pi^- p \to \pi^0 n, \quad \pi^0 \to 2\gamma;$$

$$\pi^- p \to 2\pi^0 n, \; 2\pi^0 \to 4\gamma;$$

$$\pi^- p \to 3\pi^0 n, \quad 3\pi^0 \to 6\gamma;$$

$$\pi^- p \to \eta n, \quad \eta \to 2\gamma \text{ or } \eta \to 3\pi^0 \to 6\gamma;$$

$$\pi^- p \to \Lambda K^0, \; \Lambda \to \pi^0 n \to 2\gamma n, \; K^0 \to (2 \text{ or } 3)\ \pi^0 \to (4 \text{ or } 6)\gamma.$$

$$\pi^- p \to \omega n, \quad \omega \to \pi^0 \gamma \to 3\gamma\ .$$

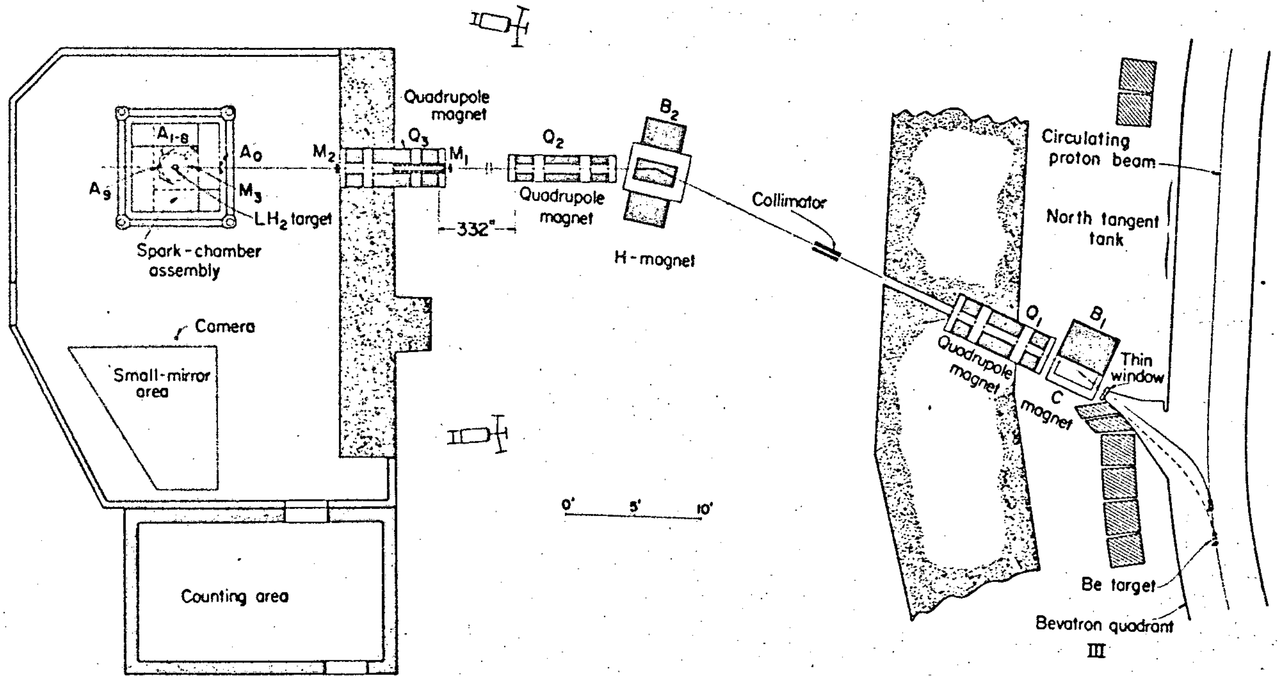

Figure 4. Plan view of the experimental arrangement. The counters, Be target, and camera are not drawn to scale.

Any decay products in the final state had to be neutral also, if the event was not to be rejected by the anticounters.

A second electronic scalar was used to count the number of neutral events. The ratio of the number of neutral events counted during any given period to the number of incoming beam particles counted during the same period is a quantity which is simply related to the total neutral cross section. That is, except for corrections, the total cross section for the process

$$\pi^- p \rightarrow \text{all neutral final states}$$

was determined in this experiment by the counters alone.

Inspection of the final states listed above shows that ultimately they all consist solely of neutrons and photons. Neither the π^0 nor the η travels any measurable distance from the point of production before the decay takes place. Therefore, to detect and record the direction taken by the decay photons was the function of the rest of the experimental apparatus. This was done through the process of electron-positron pair production in the presence of heavy nuclei, followed by the development of a cascade shower.[15]

When a high energy photon passes through a sufficient amount of matter, there is a high probability of its undergoing materialization, or conversion into an electron-positron pair. As the two particles then penetrate more material, they undergo accelerations, and hence radiate more photons. This leads to the production of more pairs, which also radiate, and in this fashion the particles continue to multiply into a shower. Another process which contributes to the number of charged particles in the shower is Compton scattering of a photon from an electron, in which the electron is ejected from the atom. The shower builds up until the original energy of the photon has been divided so many ways that each individual particle has a much lower energy. Then the predominant mechanism by which the electrons lose their remaining energy becomes excitation and ionization of atomic electrons, rather than radiation, and shower development ceases.

In this experiment the steel plates in the spark chambers provided the photon conversion material. The hydrogen target and anti-counter system were completely surrounded by an assembly of six large spark chambers, which formed the six faces of a closed cube. When the counters indicated that a neutral event had occurred, the spark chambers were triggered, and a photograph was taken, which contained two mutually perpendicular views of the sparks in each chamber. The incoming beam track was recorded in the entrance chamber, where there was a small aluminum region through which the beam could enter the cube. From zero to six photon-initiated showers were recorded in each frame, depending both on the number of photons in the final state, and the fraction of them having an energy above the detection threshold of the chambers.

The measurement and analysis of these pictures yielded the branching ratios among the various final states, and hence the total cross section for the reaction

$$\pi^- p \to \eta n \ .$$

In addition, the angular distribution characteristic of η production was obtained. The methods used to reduce the data will be described after a more detailed description of the elements of the experimental apparatus.

B. The Pion Beam

Pions for the beam were produced by bombarding a beryllium target plunged into the internal circulating proton beam of the Bevatron. The number of pions produced, N_π, is proportional to the effective number of nucleons per cm^3, $\rho/A^{1/3}$, where ρ is the density of the target material and A is the molecular weight. Electrons are also produced, mostly when photons from neutral pion decay convert to electron-positron pairs in the target. Hence, the number of electrons is proportional to $N_\pi \rho \, Z^2/A$, where Z is the charge on the target nucleus.[16] As a suitable material for the target, beryllium was chosen to maximize pion production while minimizing the ratio of the number of electrons produced to the number of pions produced.

In the shape of a rectangular solid, the target was 6 inches long in the direction of travel of the protons, 1/2-in. wide and 1/4-in. high, with a 1/8-in. thin lip at the upstream end, extending 1/4-in. into the path of protons traveling in orbits of larger radii. The lip degraded the energy of these protons so that they would fall to a smaller radius in succeeding revolutions and strike the main part of the target. This target, not drawn to scale, can be seen in Fig. 4, the plan view of the experiment.

The pions were transported from the internal target to the experimental area by the system of magnets shown in Fig. 4. The elements of the system were the magnetic field of the Bevatron itself; B_1, a 16 by 36-in. C-magnet, with an 8-in. gap; Q_1, Q_2, and Q_3, all 16 by 32 by 16-in. triplet quadrupole magnets, with an 8-in. diameter bore; the collimator, a lead cylinder, 24-in. long with a hole whose width was 2-in. in the horizontal plane, and which was bounded by an 8-in. diameter circle in the vertical direction; and B_2, an 18 by 36-in. H-magnet, with an 8-in. gap.

The internal target was mounted on a remotely controlled cart, which traveled inside Quadrant III of the Bevatron near the north tangent tank at a constant radius from the center of the quadrant. For each desired momentum, a combination of target position and Bevatron field strength was found that permitted pions near that momentum to leave the Bevatron vacuum tank through a thin aluminum window with an orbit which passed through a fixed point near the center of B_1. The IBM 650 computer program, ETHELBERT, was used to trace these orbits through the magnetic field of the Bevatron.[17] The total range of azimuthal travel was 2.56 deg (26.8 linear inches), and the variation in the time in the acceleration cycle at which the target was plunged was such that the internal magnetic field of the Bevatron was between 10 and 15 kg at spill time. At each beam energy the amount of deflection in B_1 was set at a different angle near 15 deg so that the different orbits from the internal target were all directed down the fixed center line of the rest of the magnet system.

In Fig. 5 the optical properties of the beam are shown schematically (not to scale). Quadrupole Q_1 produced a focus in the horizontal plane somewhere inside the collimator pipe, and a focus in the vertical plane a little before the collimator. The position of the vertical focus was chosen to minimize the vertical size of the beam envelope inside Q_2 and Q_3. The position of the horizontal focus inside the collimator differed at different beam energies, as will be

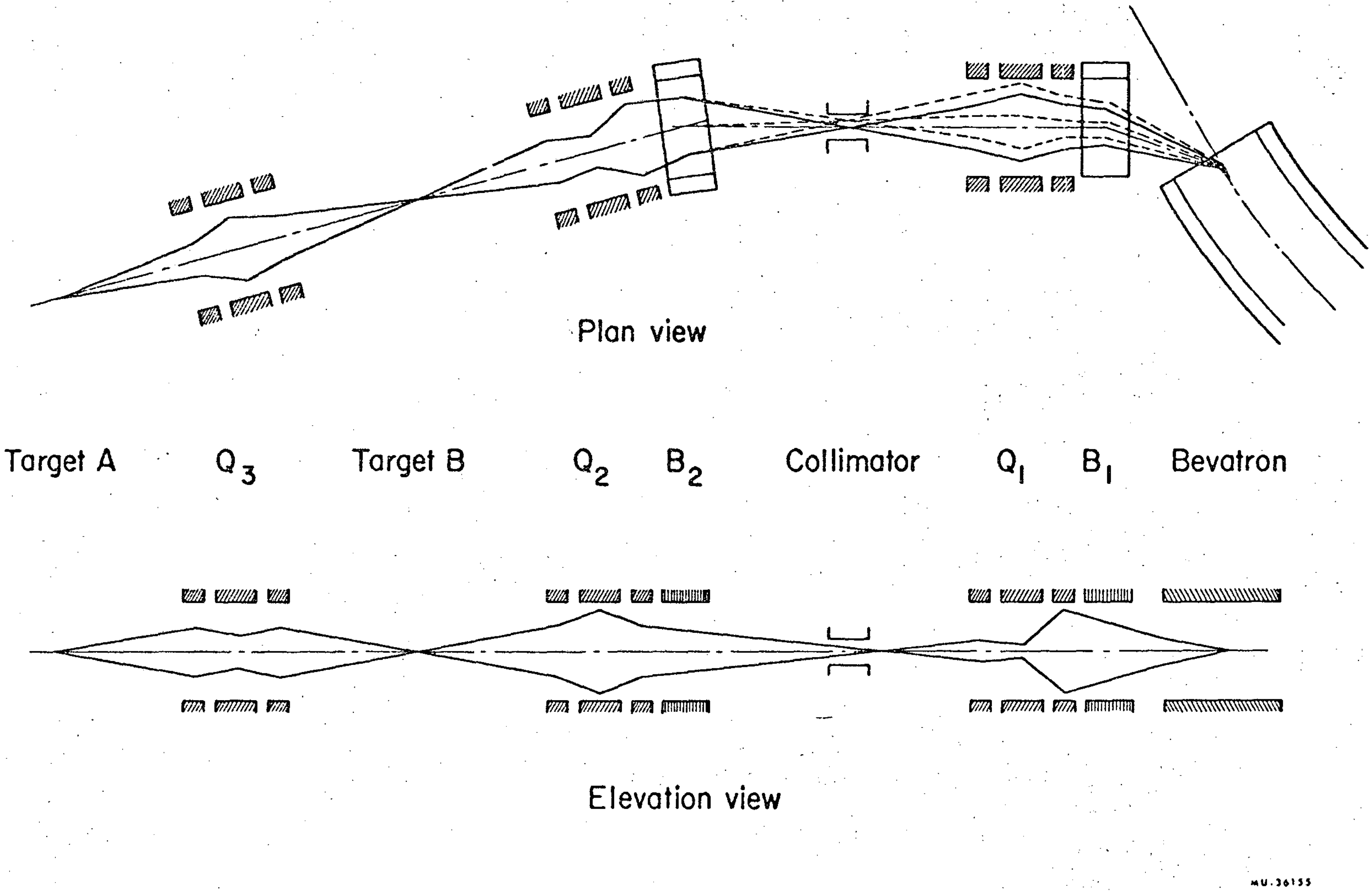

Figure 5. Schematic diagram of the beam optics, showing the focusing properties of the magnets.

explained below in the paragraphs on momentum selection.

Bending magnet B_2 turned the beam through an angle of 25 deg. Then quadrupole Q_2 focused the beam both horizontally and vertically at the position of target B, the liquid hydrogen target of another experiment which was in progress at the same time.[18] Finally, pions not scattered from target B were refocused by quadrupole Q_3 onto target A, the target for this experiment. This last quadrupole contained a brass collimator to reduce the pion flux at the final target. In order to decrease multiple scattering of the beam particles in the air, a bag containing helium slightly above atmospheric pressure was placed in the beam channel from the Bevatron through Q_2.

The Bevatron magnet and B_1 introduced dispersion into the first section of the beam; that is, only particles of the correct momentum were brought to a horizontal focus in the center of the collimator. Pions of slightly different momentum were deflected by a different amount and brought to a focus to the right or left of the center, and hence only a narrow momentum band with $\Delta p/p \leq 2.5\%$ could pass through the system. This is illustrated by the dotted lines in Fig. 5, for pions which have a momentum which is approximately 1% too high. There it is seen that since these rays of high momentum approach B_2 from an off-axis focus, a deflection of slightly less than 25 deg would make these rays coincident with the rays of correct momentum from there on. In fact, since these pions have a slightly higher momentum, they are <u>not</u> deflected by quite 25 deg in B_2, and the beam is achromatic from there on to the hydrogen targets.

The exact position of the horizontal focus within the collimator required to produce this achromatic effect was slightly different for the different locations of the internal Bevatron target, and was established with the use of the computer program, OPTIK.[19] OPTIK was used throughout in designing the external magnet system to estimate the currents required in the magnets to produce the desired optical properties. The final solution was checked with another computer program, TRANSPORT.[20]

Wire orbit measurements in B_2 were made prior to the experiment to determine within 1% the momenta passed by the system. The currents in the quadrupoles were then tuned to produce a beam of the desired characteristics at the target position. At the final current settings, the beam profiles were approximately Gaussian in shape, with full widths at the 1/e points between 1.5 and 2.6 in. in the horizontal plane, and between 2.0 and 3.2 in. in the vertical plane.

The solid angle acceptance of the system was 1 msr. The duration of the spill varied between 200 and 800 msec, while the average instantaneous rate of pions as determined by the three monitor counters in front of target A was maintained near 50,000 pions/sec.

C. Liquid Hydrogen Target

The pion beam passed through a target containing liquid hydrogen, which was located in the center of the experimental apparatus. Shown in Fig. 6 is a diagram of this target. The flask containing liquid hydrogen was made from 5-mil Mylar by joining two roughly hemispherical ends to a center band. This band was 3-3/4 in. in dia. and 1-3/4 in. wide, while the ends had a radius of 2-1/2 in. By making a weighted average of the actual flask length along possible beam paths, we determined the effective length of the flask to be between 3.92 and 3.94 in. The weighting factor, different at different energies, was given by the measured beam profile out to a distance from beam center determined by the radius of the last and smallest beam monitor counter.

The hydrogen flask was supported and serviced by two 1/2-in. stainless steel tubes, which ran from it through a 3-in. aluminum tube to a reservoir of liquid hydrogen on top of the apparatus. As can be seen in Fig. 11, of Sec. II. E., the outer aluminum tube approached the target from a direction that minimized the solid angle it subtended. One of the 1/2-in. tubes was the fill tube, which directly connected the bottom of the flask and the bottom of the reservoir, and continuously supplied liquid hydrogen to the target vessel. The other 1/2-in. tube was the boil-off tube, as shown in Fig. 6. This tube was open to the air above the liquid level in the reservoir, to allow evaporated hydrogen to escape from the system.

At the top the boil-off tube could be closed by a valve, in order to empty the liquid hydrogen from the target flask. When the

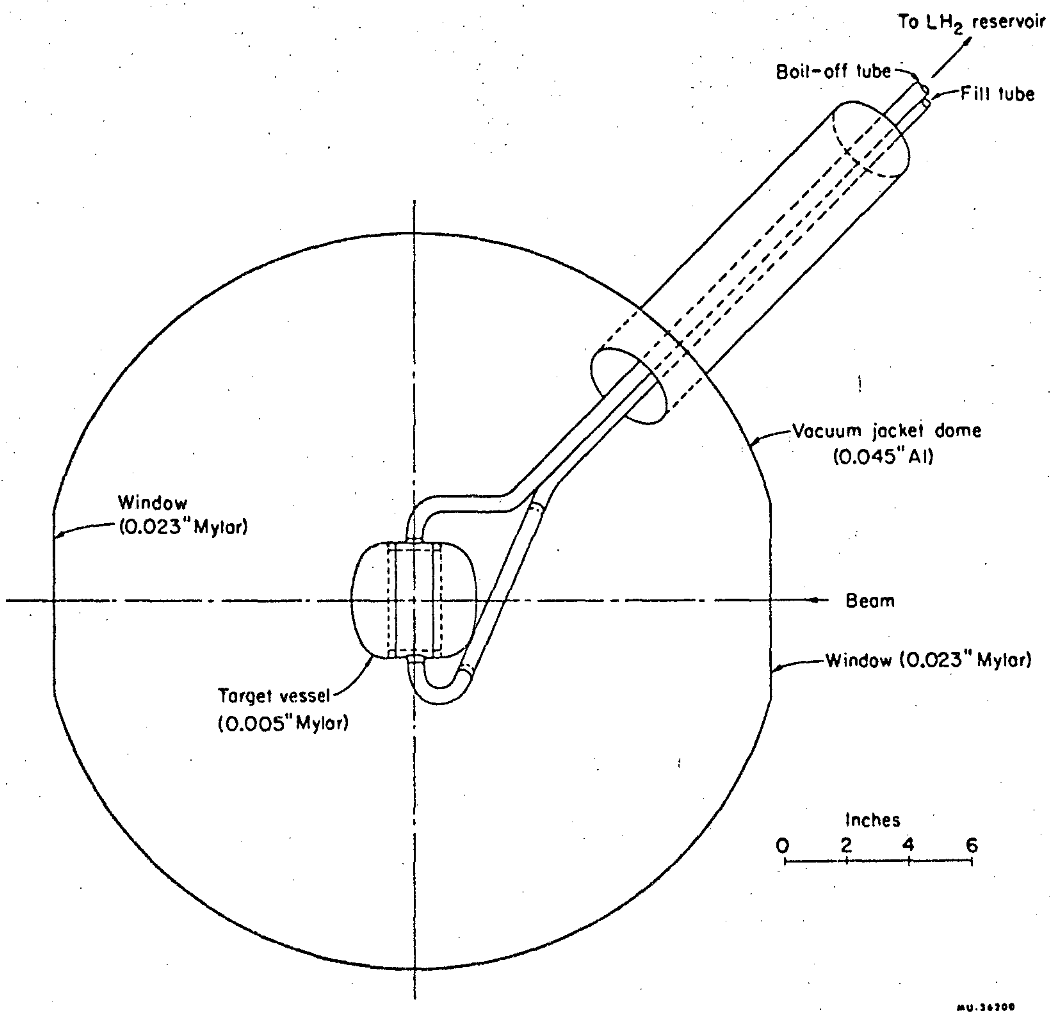

Figure 6. Elevation view of liquid-hydrogen target flask and surrounding vacuum dome.

valve was closed, the gradually accumulating gaseous hydrogen forced the liquid hydrogen out of the flask and back up the fill tube into the reservoir. At frequent intervals throughout the experiment, data were taken with the target empty in order to determine the background due to interactions of the beam in substances other than hydrogen.

To minimize the heat transfer to the target by conduction, the flask was contained in an evacuated aluminum dome. Where the beam entered and left the dome, there were windows of laminated Mylar, with a total thickness of 22.5 mils in each window. (The total amount of material in g/cm^2 traversed by the beam in the vicinity of the target was about one-third the amount of liquid hydrogen in a full target.) The thickness of the aluminum dome was 45 mils, the minimum considered safe. The diameter of the dome was 2-ft., thus placing the walls far enough from the hydrogen that interactions in the aluminum could be distinguished from interactions in the hydrogen. Aluminum was used because of its low Z, so that conversion of photons in the walls of the dome would be minimized.

Heat transfer by radiation was reduced by the addition of several layers of 1/4-mil aluminized Mylar around the flask. Even so, a significant amount of boiling of the liquid hydrogen was observed through the windows when the flask was full, and the density of the liquid was estimated to be $(5 \pm 3)\%$ less than the normal density, due to the presence of the bubbles. For calculation of the number of hydrogen nuclei available for interaction, this factor was taken into account.

D. Counters

1. Scintillation Counters

The scintillating material used for the counters in this experiment was a solid solution of terphenyl in polystyrene, and all light pipes were made of lucite. RCA 6810 photomultiplier tubes were used to view all the scintillators on the outside of the spark chamber cube, while inside the cube RCA 6199 photomultipliers, smaller 10-dynode tubes, were used to keep the amount of material between the hydrogen target and the spark chambers at a minimum.

According to function, the scintillation counters fall into two classes: a) those defining the beam, and b) those detecting a charged final state.

The beam-defining counters, M_1, M_2, A_0, and M_3, were positioned along the incoming beam as indicated in Fig. 4. M_1 and M_2, placed at the ends of Q_3, were 1/4-in. thick and large enough in diameter to detect all the pions passing through the quadrupole. M_3 had a thickness of 1/16-in. and was placed inside the spark chamber cube as close as possible to the vacuum jacket of the hydrogen target. With a diameter of only 2-in., M_3 insured that beam particles accepted by the system would traverse the liquid hydrogen and not the material of the walls of the flask. A_0, a 1/4-in. thick counter with a 4-in. diameter hole, was used in anticoincidence with $M_1M_2M_3$ to prevent a pion which scattered into M_3 from the steel portion of the entrance spark chamber from being accepted. The signature of an acceptable beam particle, then, was $M_1M_2M_3\overline{A}_0$.

To detect and suppress charged final states, anticounters A_1

through A_9 were placed around the hydrogen target inside the spark chamber cube, as shown in Fig. 4 and in Fig. 11 of Sec. II. E. In Fig. 7 is illustrated schematically (not to scale) the construction of the anticounter system, the size of which was determined by the requirement that it fit around the 2-ft. diameter vacuum dome enclosing the liquid hydrogen target. The separate counters, A_1 through A_4, were 1/2-in. thick, and each formed one side of the unit, while A_5 through A_8 were four phototubes attached to one 1/4-in. thick scintillator on the downstream end of the system. In this scintillator was a hole, slightly larger than the beam size and covered by another 1/4-in. thick circular counter, A_9. This last anticounter had by far the highest counting rate.

The anticounter unit covered a solid angle of slightly more than 2π sr on the downstream side of the hydrogen target. However, even though the anticounters did not completely surround the hydrogen target, the loss of efficiency in rejection of charged final states was estimated to be very small. It is kinematically impossible for the particles of a 2-body final state to go into the backward hemisphere. To estimate the efficiency for a three-body final state, data from an experiment on single pion production at these energies was used. These showed that in $\pi^+\pi^-n$ final states, those cases in which both charged particles went into the backward hemisphere constituted only 2% of the events.[21] These few events do not create a problem, because any charged particle events which were not eliminated by the anticounters can be recognized in the film. One can then reject these events and correct the electronic cross section measurements by the fraction of the events

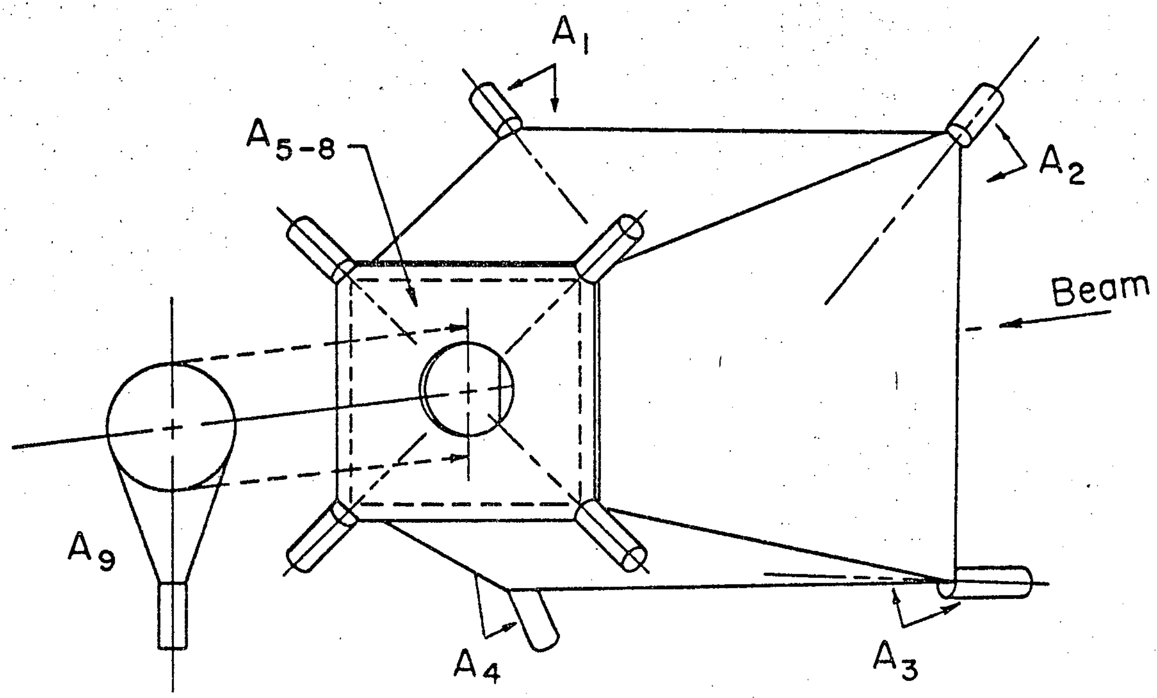

MU-36198

Figure 7. Drawing of anticounter system.

on film which contain charged particles.

2. Cerenkov Counter

Prior to and after the experiment, the electron and muon contamination of the beam was studied with a Cerenkov counter in which sulphur hexaflouride gas was the radiating medium. This counter was placed just downstream of Q_3, and was preceded and followed by 2-in. diameter scintillation counters, S_1 and S_2. To determine the contamination, the ratio S_1S_2C/S_1S_2, which gives the fraction of the beam particles with velocity above the threshold of the Cerenkov counter, was recorded as a function of the gas pressure.

The velocity threshold of a Cerenkov counter is at $v_{th} = \frac{c}{n(p)}$, where c is the velocity of light, and n is the index of refraction of the gas, which depends on its pressure. Since the beam is momentum-analyzed by B_2, particles of lower mass have higher velocities. Thus as the gas pressure is raised from atmospheric, the counter first responds proportionately to the lowest mass component, and then the higher mass contribution is added. A typical curve of the triples-to-doubles ratio vs. pressure of the gas is given in Fig. 8, where the three plateaus due to a) electrons alone, b) electrons plus muons, and c) electrons, muons, and pions, are visible.

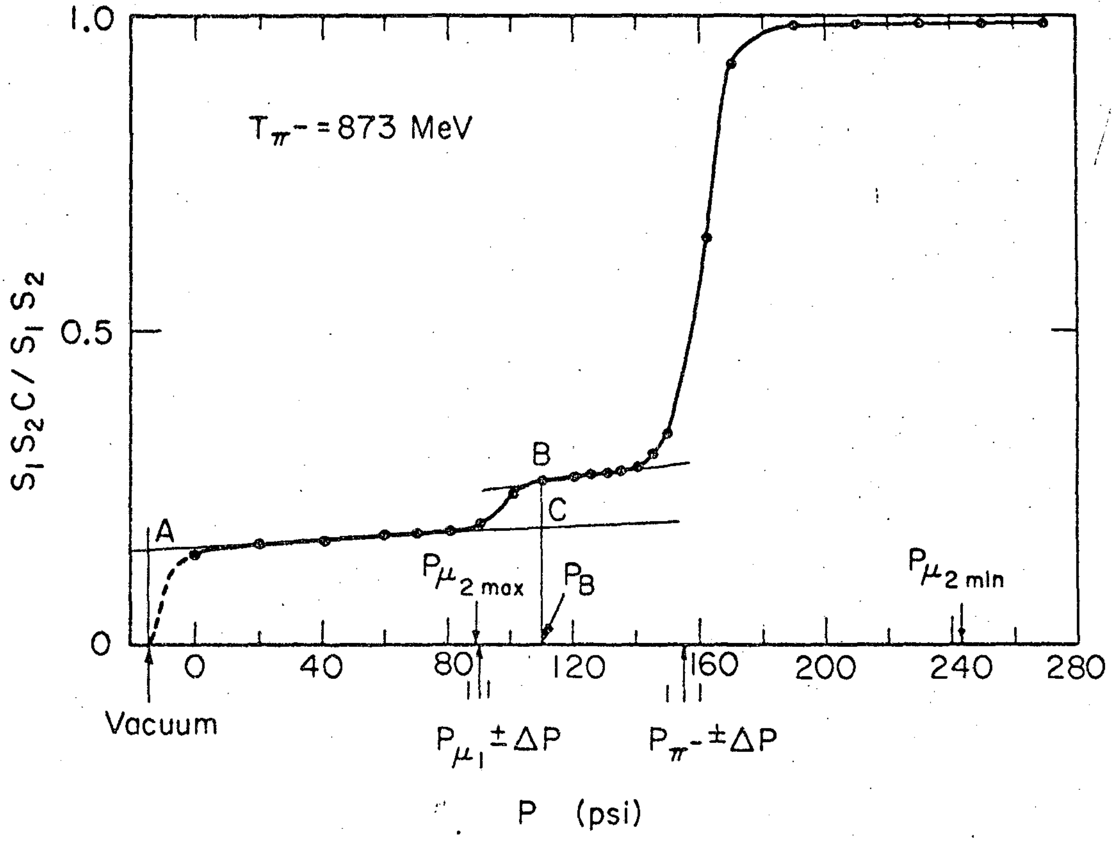

MU-36199

Figure 8. Gas Cerenkov counter pressure curves taken at T_{π^-} = 875 MeV. Plateau A is due to electrons, plateau B is from electrons and muons, and the high plateau at the right is from electrons, muons, and pions. The pressure threshold for detecting pions is at $P_{\pi^-} \pm \Delta P$, and the threshold for detecting muons which have been momentum-analyzed is at $P_{\mu_1} \pm \Delta P$. The threshold for detecting muons from pions decaying after the last bending magnet varies with their momentum from $P_{\mu_2 \max}$ to $P_{\mu_2 \min}$.

E. Spark Chambers

Six spark chambers, each weighing 2-2/3 tons, provided a γ-ray detector with 4π sr coverage around the hydrogen target and anticounter unit. Illustrated in Fig. 9 is the manner in which the chambers were arranged in a cube. Figure 10 shows the construction of one of the chambers. Each one had 41 plates: one 1/32-in. aluminum plate, four 1/16-in. aluminum plates, thirty-five 1/8-in. steel plates, and a 3/4-in. steel base plate. Lucite strips at the edges and four staggered lucite squares near the center maintained a gap of 5/16-in. between each pair of plates and also provided electrical insulation. The gap between the last 1/8-in. steel plate and the base plate was inactive. Also, the thin aluminum plate did not provide an active gap; its function was merely to prevent the first 1/16-in. aluminum plate from bulging under the internal pressure of the gas. In the chambers a mixture of 90% neon and 10% helium was maintained at an equilibrium pressure slightly higher than atmospheric pressure.

Of the thirty-eight active gaps, the first four were associated with the aluminum plates. The purpose of these gaps was to provide a visual check for charged particles. With the γ-rays, there was a relatively low probability that one would be converted in the aluminum region, in contrast to a charged particle, which would ionize the gas as soon as it entered the chamber. Therefore, the aluminum plates formed a second line of defense against charged particles not caught by the anticounters.

Taking into account the expected energy spectrum of the photons and the distribution of the angle of entrance of the γ-rays into the

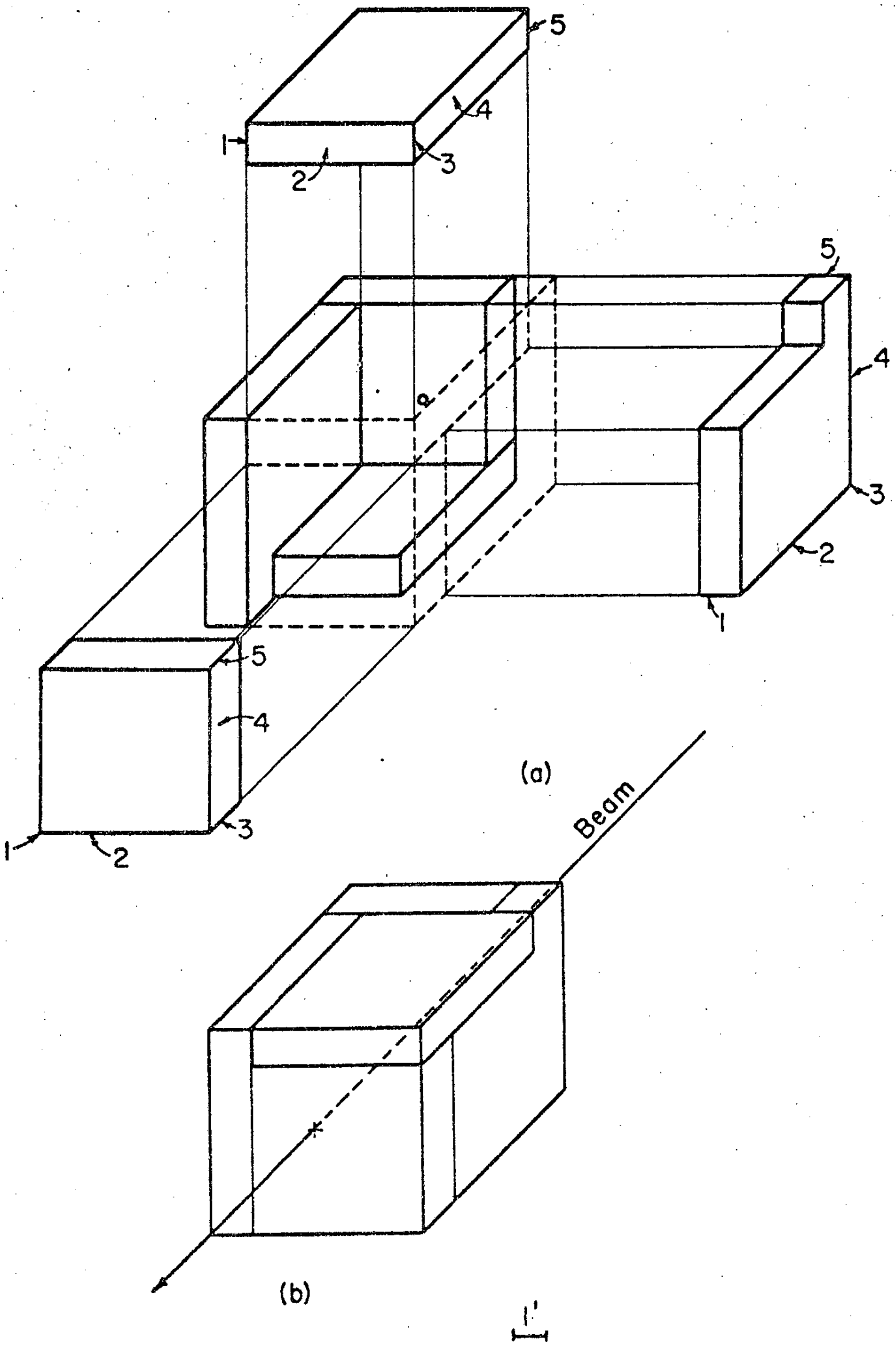

Figure 9. a. Exploded view of the spark chamber cube. A neon-helium gas mixture was introduced into each gap at "1," and run out again at "5." The optical faces, through which the sparks were photographed, are at "2" and "4," and the electrical connections were made to each chamber at "3."

b. The spark chamber cube assembled.

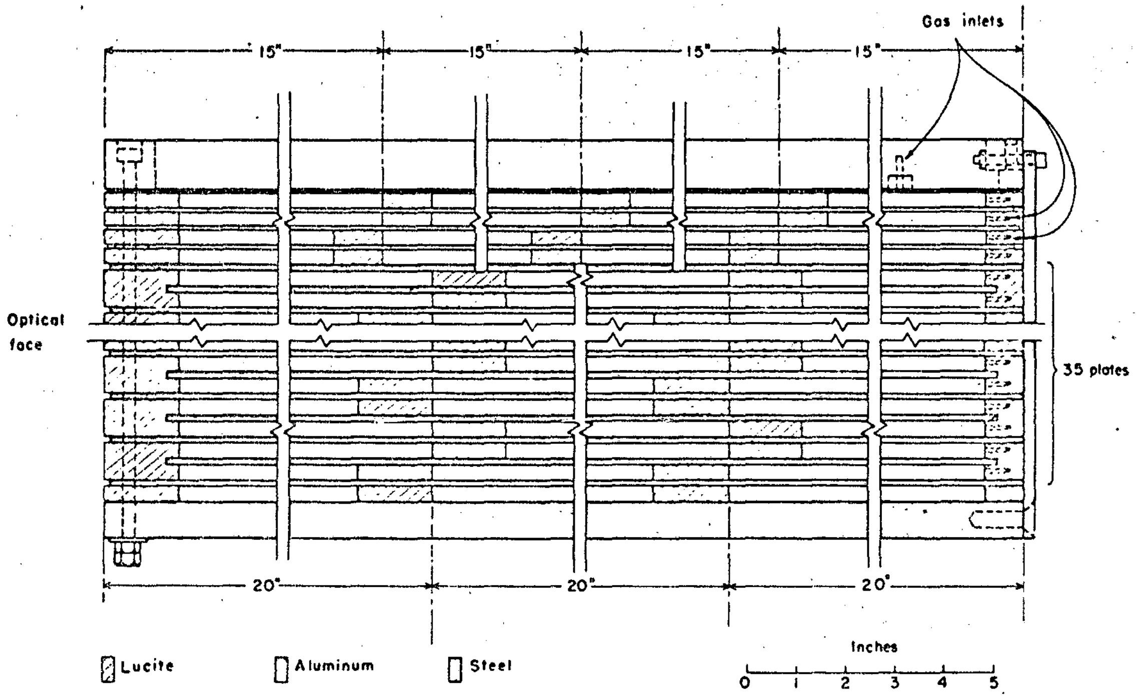

Figure 10. A schematic diagram showing in cross section the construction of one of the spark chambers.

plates, it was estimated in a Monte Carlo calculation that the 34 steel plates preceding the remaining 34 active gaps provided a total of 4.6 effective conversion lengths for pair production. This meant that there was less than a 2% chance that a photon would pass through the chambers without undergoing materialization.

In over-all size, the typical chamber was 5 by 5 by 1-1/2 ft. However, four out of the six chambers were not typical in some aspect:

a. Two of the chambers, on the left and right in Fig. 9a, had a small extra section appended at one corner. It was necessary to add this "dog-leg" in order to have a complete cube and yet have two edges of each chamber exposed to permit stereo observation of the sparks between the plates.

b. Not shown in Fig. 9, the top chamber had the corner opposite "3" cut off to allow the tubes which serviced the hydrogen target to enter the cube.

c. At the place where the pion beam passed through the entrance chamber, there was a region 4-in. in diameter where the plates were made of thin aluminum foil instead of thick steel to minimize spurious interactions of the beam with the chamber. This was the biggest area of the detector not capable of converting γ-rays, but it subtended a solid angle of only $\pi/100$ sr, which is negligible.

Figure 11 is a photograph of the assembly during set-up. Not yet in place are the top and entrance chambers, so the anticounter and hydrogen target vacuum dome and service pipe may be seen, in addition to the other four chambers. Partially hidden by the "dog-leg," the last monitor counter is seen in the lower center of the picture.

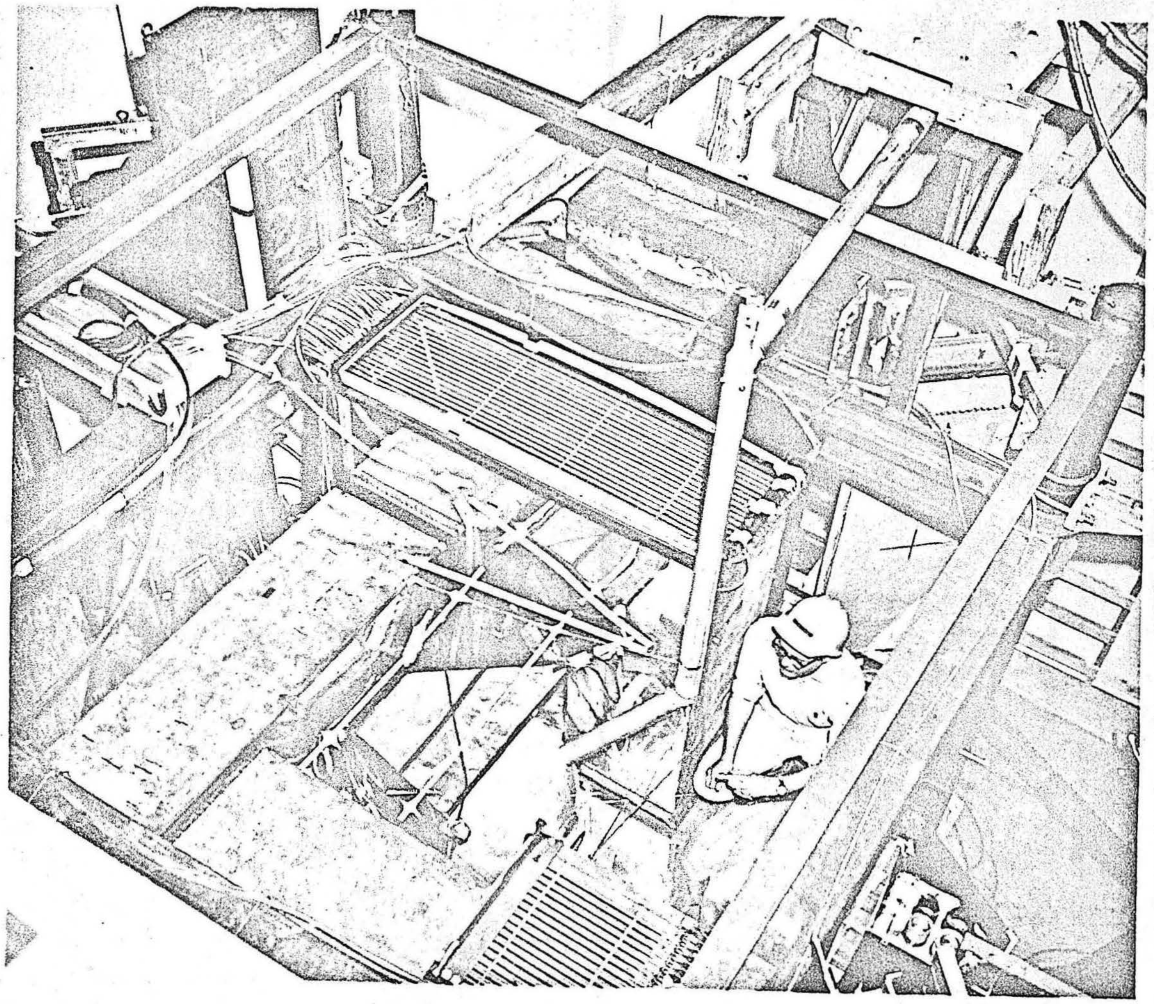

Figure 11. A photograph of the spark chamber assembly during setup. The top chamber and the beam-entrance chamber are missing. Out of view at top right is the liquid-hydrogen reservoir.

F. Optical System and Photography

The optical system used to photograph the six spark chambers is shown schematically in Fig. 12, where for simplicity each mirror and light path appears only once, either in the plan view or the elevation view, but not in both.

In the cube the chambers were arranged so that each one could be viewed from two mutually perpendicular stereo axes. Mounted on the optical faces of each chamber was a plano-convex lucite lens to enable the camera to see sparks at the far end of the thin parallel gaps from a point on the axis of the chamber. In order to eliminate spherical aberration, the curved surface of each lens was made a hyperboloid of revolution. Since the focal length of all the lenses was the same, namely 423-in., it was necessary to maintain that same distance from each face of each spark chamber along the light paths to the camera. This necessitated rather wide excursions of the light paths originating from chambers close to the camera.

In the system there were 36 plane front-surfaced mirrors, ranging in size from 4 by 5 in. to 24 by 80 in. For ease of adjustment, the smaller mirrors were attached to aluminum plates which had been mounted on camera tripod heads. The large ones were suspended from springs which were attached to metal blocks glued to the back and edge of the glass approximately every 12 in.

A double-frame 35 mm Flight Research Corp. camera (Model 207) with a cycle time of 90 msec. was used to photograph the sparks. Since the chamber and mirror system was contained in a darkened house, no shutter was necessary; the exposure time was simply the lifetime of the

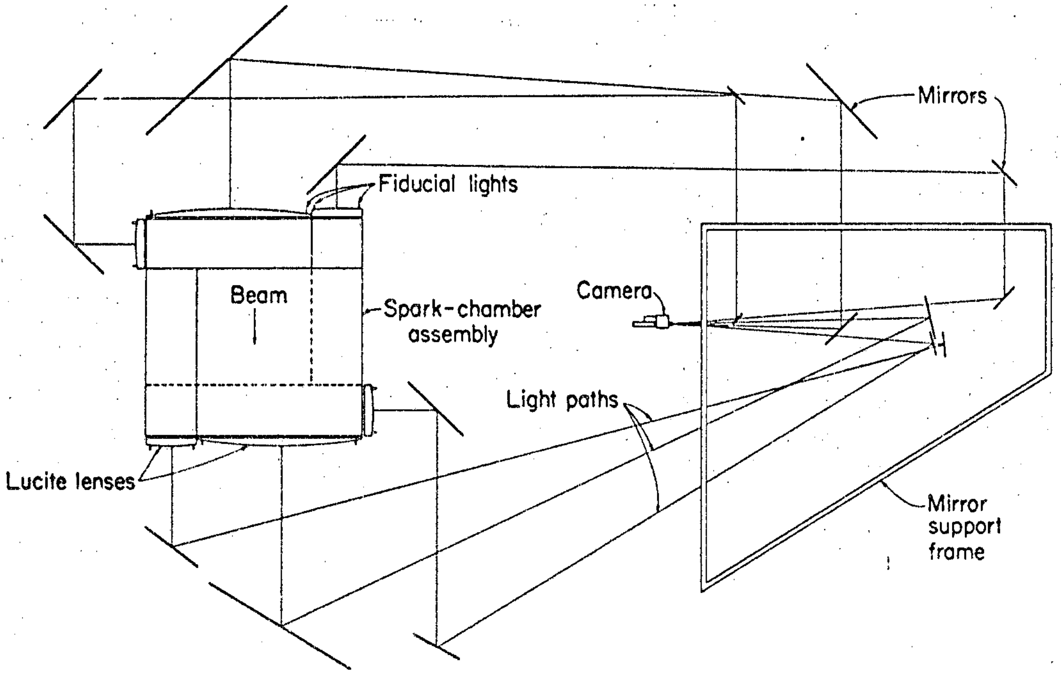

Plan view

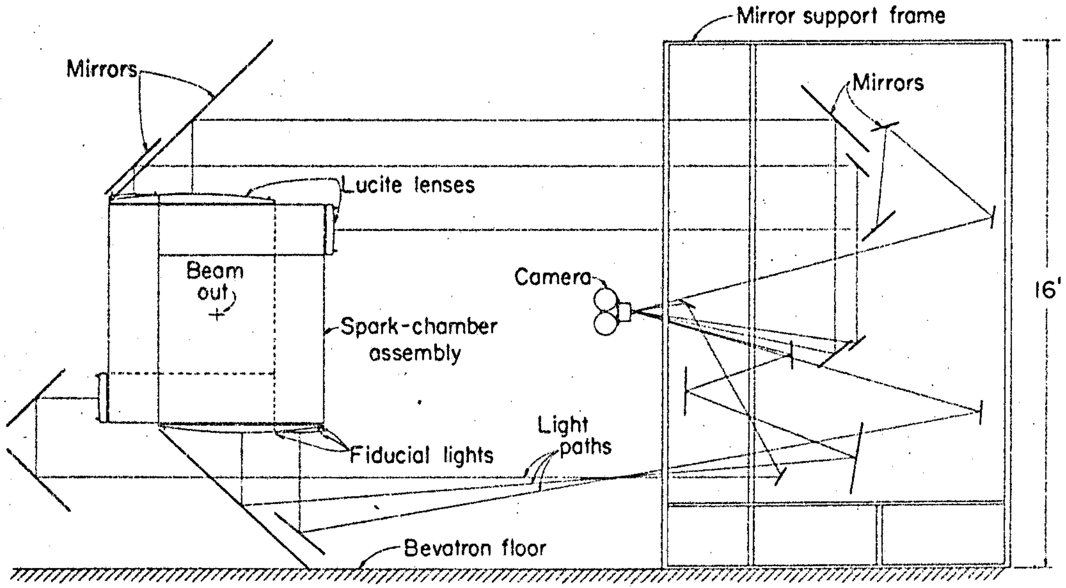

Elevation view

Figure 12. Diagram of the optical system. Each mirror is shown only once, either in the plan view or in the elevation view.

sparks, and the DuPont 140B film was advanced in the darkness between events. The trigger circuits were gated off for 90 msec. after each event to allow time for the film advance. During every event a stroboscopic lamp was triggered electronically and illuminated a data box behind the mirrors which contained information such as the roll number and target condition. The signal to advance the film also advanced a serial counter with nixie-light readout photographed on each frame. The camera lens had an aperture set at f/8, and a focal length of 58 mm, so that the reduction factor from the object space to the film was 185:1.

To provide reference fiducial marks on the film, incandescent flashlight bulbs covered with an L-shaped mask were mounted near the four corners of each lucite lens. Their position in space could be reconstructed from the film to an accuracy of 3/8-in. It was necessary to check all the bulbs periodically and replace the ones that had burned out since the last check, since switching them off between Bevatron pulses reduced their mean life to about 10 hours.

A photograph of a typical event is shown in Fig. 13. On it is superimposed a template, which was used during the scanning of the film to make clear the limits of the chambers, and the position of the target relative to each view. The views of the chambers were arranged in a format on the film in three groups of four views each, with each group of four being the views contained in one of the three possible cross sections of the cube.

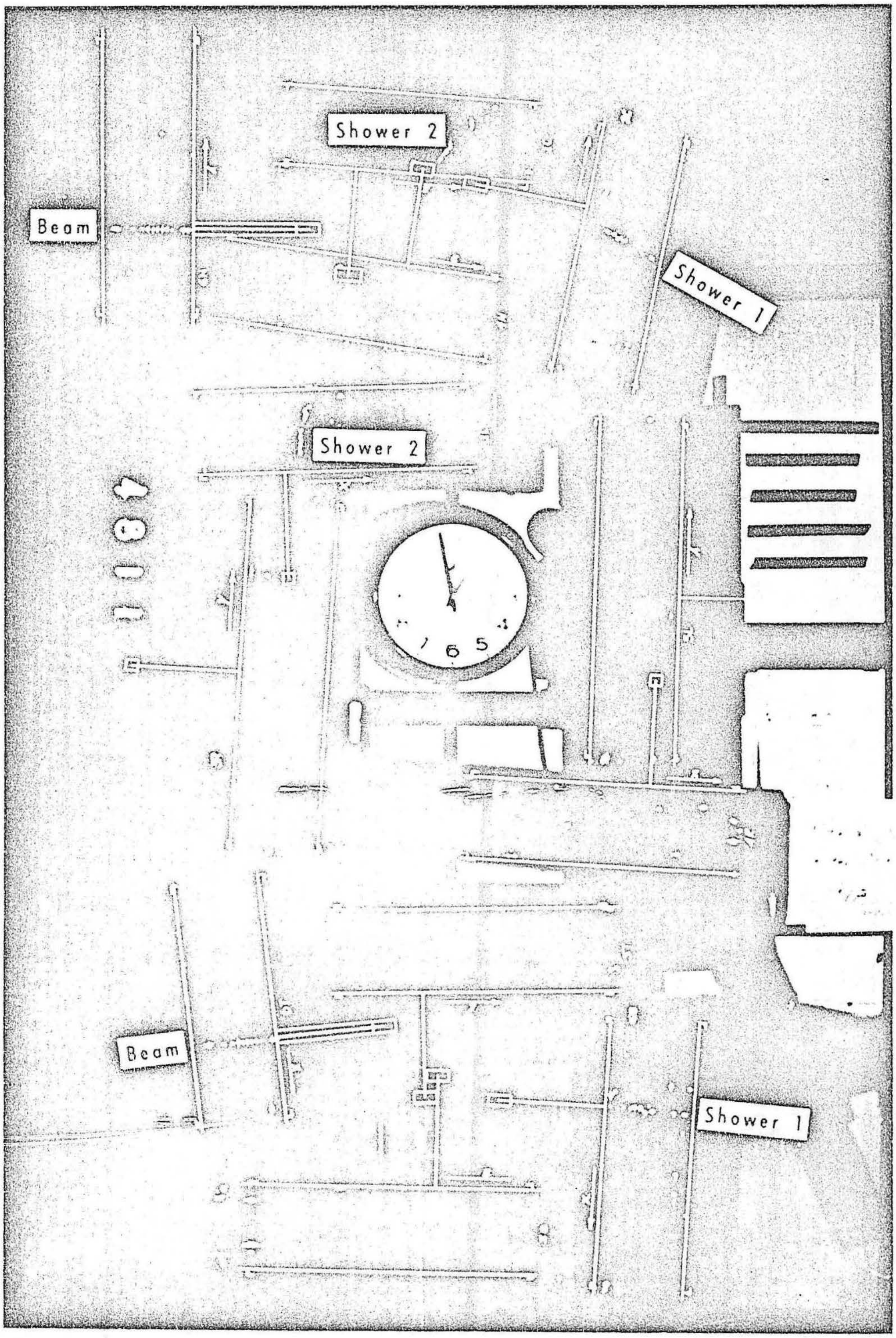

Figure 13. A sample event from the film. The straight white lines are on a template used during the scanning to indicate the limits of the views of the chambers.

G. Electronics

1. Elements of the Logic System

This section describes the simple electronic circuitry which acted as the central nervous system of the experiment. Having received pulses from the scintillation counters, this group of electronic components determined when a neutral event had occurred. It then sent a signal to trigger the spark chambers only if a) the camera had had enough time to advance the film since the last picture, and b) no other beam particle had previously passed through the counters within a time approximately equal to the sensitive time of the chambers.

Shown in Fig. 14 is a block diagram of the electronics system. The first Wenzel coincidence circuit, W_1, received signals from the beam monitor counters. A coincidence among M_1, M_2, and M_3, in the absence of a signal from A_0, defined an acceptable incoming particle and resulted in an output monitor signal from W_1. A 100 Mc scalar, labeled "Monitor Scalar" in the diagram, counted the number of output pulses from W_1.

Together with the summed signals from anticounters A_1 through A_9, the monitor signal was fed to the second Wenzel coincidence circuit, W_2. The anticounter signals, of course, were connected to the anticoincidence input of W_2. An output pulse from W_2 was the electronic definition of a neutral event, and these signals were counted by a 10 Mc scalar, the "Neutral Scalar."

A third coincidence circuit, W_3, was a standard LRL transistorized Jackson circuit which had been modified so that it had two anticoincidence inputs instead of only one. This enabled two separate

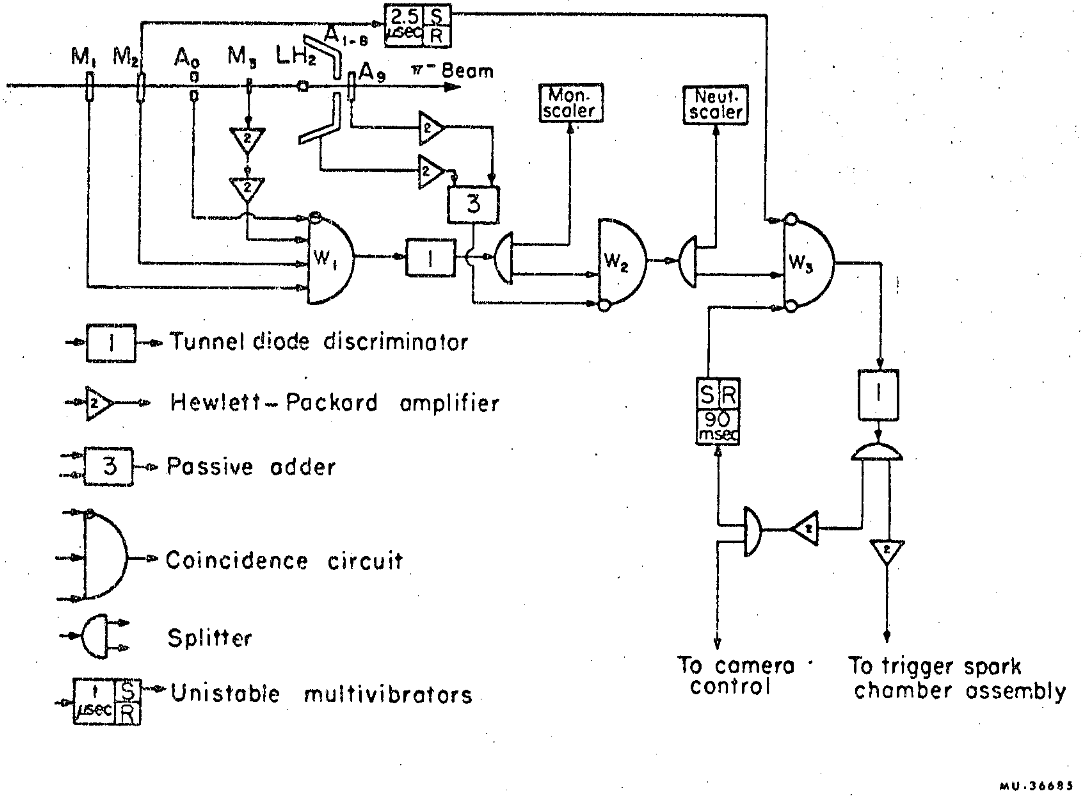

Figure 14. Block diagram of the electronics.

disabling gates to be imposed on the neutral signal from W_2 before it was used to trigger the spark chambers.

Each time a signal was sent to the camera control circuits, the first gate was turned on. The unistable multivibrator which generated the gating voltage had a period of 90 msec, which is the time required for the camera to advance the film; and this gate prevented neutral pulses from triggering the spark chambers faster than the camera could photograph the events. This camera cycle time imposed the upper limit on the rate at which data were taken.

By introducing the second gate at W_3, we were able to reduce the number of pictures in which there were two or more beam tracks. Frames of this type are not useful in the analysis, because it is not known what outgoing tracks to associate with which beam particle. In every picture of an event there is always one beam track due to the pion which produced the neutral event and triggered the chambers. However, if another beam pion had also entered the chamber within a short enough time before the triggering pion, its track would also appear. The critical time interval--the sensitive time of the chambers--depended mainly on how long it took the relatively low clearing field of the spark chambers to sweep out the ions of old tracks. By disabling the system after the passage of every beam particle for a time comparable with the sensitive time of the chambers, the number of double-beam pictures was minimized. Neutral events that had been preceded too recently by another pion were automatically rejected.

Pulses from monitor counter M_2 were used to trigger this gating signal, because this counter was large enough to intercept all of the pions in the beam. The length of the gate was set empirically at about 2.5 μsec during the experiment. This was the largest gate-width it was possible to use without slowing the rate of taking data. From the observed number of frames of film containing two or three incoming beam particles, together with this known gate length, the sensitive time of the chambers was estimated to be about 3 to 4 μsec.

With the exception of the modified Jackson coincidence circuit, all of the electronic components mentioned in this section are completely described in the Lawrence Radiation Laboratory Counting Handbook.[22]

2. Spark Chamber Triggering System

Figure 15 is a schematic diagram of the system used to apply a high voltage in a very short time to the plates of the spark chambers. To accomplish this high-speed switching, spark gaps were used.

In the quiescent periods between pulses of the chamber voltage, a 15 volt potential was maintained between all pairs of plates in the spark chamber to sweep away any ions formed in the gaps. Also, through the clearing field power supply, current was drawn to charge the capacitors C_2 to a high potential. Every C_2 capacitor was one of 19 strips of parallel condensers, which were contained in each of 6 boxes--one near every chamber. The 114 condenser strips, each having 24,000 pF capacitance, were connected separately by three-foot coaxial cables to the high-voltage plates in the chambers. By having separate storage of charge for every high voltage plate, problems associated with uneven distribution of the electrical energy among the plates were avoided. With each C_2 charged to approximately 9 kV, the chambers

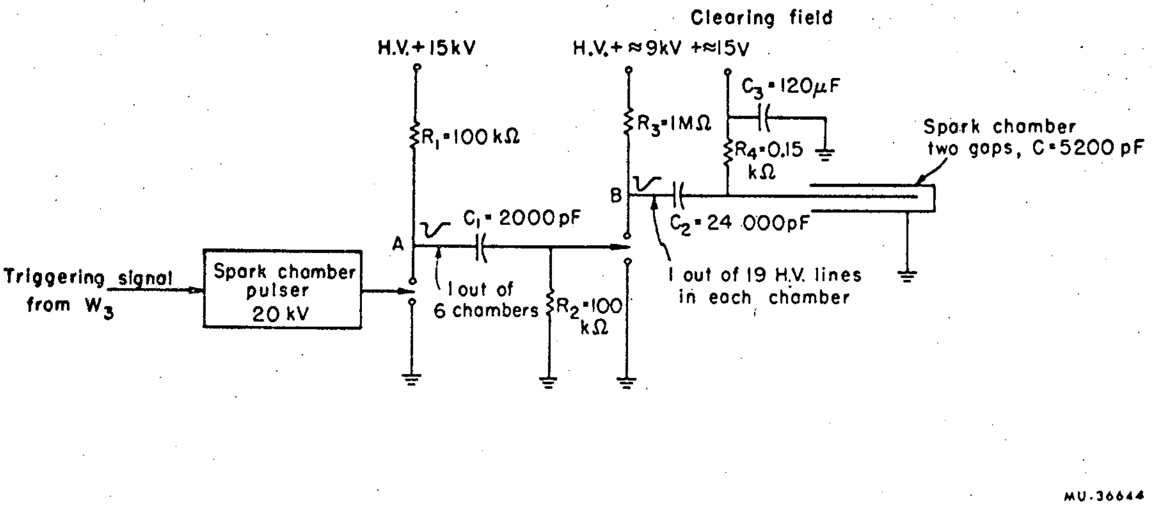

Figure 15. Schematic diagram of the spark chamber triggering system.

were ready to be used.

The triggering signal from the output of coincidence circuit W_3 was fed to the spark chamber pulser, which applied a 20 kV pulse to the trigger wire of the first spark gap. The high voltage pulse which resulted from the breakdown of this gap was split six ways and transmitted to the trigger wires of six spark gaps at the individual chambers. Thus all six chambers were triggered simultaneously. Shown at A in Fig. 15 is the circuit from this first spark gap to one of the six other gaps.

At B is the circuit from one of the chamber spark gaps through one C_2 capacitor to a single high voltage plate of the chamber. In the instant that the chamber spark gaps were fired, the high voltage side of C_2 was connected to the ground plates of the chambers, placing C_2 and the pair of chamber plates in parallel. Charge was rapidly transferred from C_2 to the plates until the voltage across both reached approximately 7.5 kV and sparks were formed along ion tracks left by the passage of high energy charged particles through the gas. If no particle had passed through the chamber in question, sparking occurred at random places between the plates, or sometimes at favorite breakdown points.

The elapsed time between the passage of a pion through the last monitor counter and the arrival of a signal at the spark chamber pulser was 175 nsec. After a delay of 250 nsec in the pulser, the spark gaps were fired. It then took 100 nsec for the voltage to rise from 0 to 7.5 kV on the plates.

III. DATA REDUCTION AND ANALYSIS

During the experimental run, nearly one-half million frames of film were exposed. This thesis is based on the analysis of approximately 50% of these.

The events recorded on film are assumed to be a completely random, and therefore representative, sample of all the interactions which the electronics have decided are neutral. Included among the pictures, for instance, are some events which contain charged particles, due to the inefficiency of the anticounters, but these were counted by the electronics as neutral events. Pictures which contain more than one beam track receive the following interpretation: One beam pion has entered the cube, produced a neutral event, and triggered the chambers; then before the voltage on the spark chamber plates has risen to its full value, one or more additional beam particles come along to enter the picture, and thus at least two beam tracks, and possibly several events, are seen. These frames are not useful for analysis, because one does not know which outgoing tracks to associate with which incoming beam particle, but the important thing is that the neutral events associated with multiple beam frames are not a unique type. In other words, a representative sample of neutral events as detected by the counters can be made from frames with only one incoming beam track.

The frames with a single incoming beam track may be divided into two categories: those with beam particles that enter the chamber cleanly, and those where the particles interact in passing through the entrance chamber. These differ in one important respect: there is a slightly higher fraction of outgoing charged particles in events initiated by interacting beams; presumably because the beam particle is often deflected and strikes a less efficient part of the anticounter. In all other respects, the frames with one good non-interacting beam track are assumed to be completely representative of all neutral events which occurred, and these form the basic sample for analysis.

A. Film Scanning

As the first step in the data reduction, a scanner examined all frames of film to make a record of the number of good events of each type and to select the subset of good events which were to be measured. Each scanner learned a basic set of precise criteria to use in making judgments about the film. In simplified form, the procedure used was as follows:

(a) First, on the basis of the quality of the incoming beam track, the frame was defined to be "good" or "bad." A "good" frame was one which contained two views of a single dark beam track passing all the way through the entrance chamber without any interaction in the chamber plates. "Bad" frames showed more than one beam track, or one track which had undergone some change on the way through the chamber, or occasionally no beam track at all. A record of the number of events in each beam category was kept, and only frames with one incoming track were considered further. On a typical roll of film, about 75% of the frames were good by these criteria.

(b) Then in frames with a single incoming beam track, either "good" or "bad," all the views of the chambers were examined for outgoing tracks. Taking into consideration both views of each track, the scanner looked for obvious, heavy charged particles which had been missed by the anticounter. They were dark and like an incoming beam track in appearance --long, straight, and clean. If there was any doubt about a borderline case, it was not considered to be a charged particle. Frames with charged particles were separately totaled according to whether the beam track was "good" or "bad."

(c) Only "good" frames with no obvious charged particles were considered in more detail. The total number of outgoing tracks in each frame was recorded, and each track was classified by appearance into two categories. A "Type-2" track was a well-developed shower, generally "bushy" looking, while a "Type-1" track did not appear to be a shower. A Type-1 track--not as straight, clean, and dark as a charged particle--was a minimum of three collinear sparks within four gaps. Anything less was not considered to be a track. Each chamber had several places which consistently broke down when the voltage was pulsed, but as this produced a spark in exactly the same place in every frame, there was no difficulty in recognizing that they were not minimal showers.

"Good" frames which were to be measured were then marked on the scan sheet. A large fraction of these frames were rescanned to check the accuracy of the original work and to attempt to foresee any difficulties which might arise in the measuring process.

B. Measurement of Film

All events which could possibly be the result of a meson decay into two photons were measured with a digitized protractor. One-track events occurred when one of the photons had too low an energy to produce a visible track. Two-track events were the expected type. Three-track events could sometimes be interpreted as a meson decay with two showers from photons, plus one track made by a proton knocked out of a steel plate by the neutron in the final state. Also, three-track events were useful in estimating the shape of the background in the two-track distributions. Hence, all "good" one, two, and three-track events which did not contain obvious charged particles were measured. In order to begin a roll of film, it was necessary to measure in several frames the position of as many of the 48 fiducial lights as could be seen. If two or three out of the four lights associated with a given view were visible, the film position of the missing light or lights could be reconstructed, using the measured separation of the lights on the chambers. If more than two of the four lights were missing, information from an adjacent roll of film was used to furnish the film coordinates of the missing lights. The several measurements for a given roll of film were averaged to produce a master set of fiducial measurements for that roll.

After this was completed, the events were measured. On each frame two fiducials were measured to indicate the orientation of the projected film image on the measuring table. The direction of the incoming beam track, and the beginning and end points of each outgoing track were measured in both views in which they occurred. Punched paper tape from the digitized protractor was read by the first of a series of computer programs which, by using the master set of film fiducial measurements and the coordinates of the fiducials on the chambers, reconstructed in three-dimensions the direction of the incoming beam particle and the position of the tracks in the chambers. This information and all the parameters of the measuring and reconstructing process were maintained in a library of magnetic tapes.

At the edges of the cube, a shower could begin in one chamber and end in another. Often the views of the two different chambers involved were widely separated on the film, with the result that the scanners thought there were two different showers instead of two pieces of only one shower. This situation was detected because of the extremely small angular separation of the two pieces when reconstructed in three dimensions, and corrected by the programs. In this manner, about 18% of the three-shower events measured were changed to two-shower events, and 2.5% of the two-shower events were changed to one-shower events.

The uncertainty in a coordinate measurement could be estimated by making use of the redundant information in the stereo views. For example, if one view was a projection in the x-z plane, the other view might be a projection in the y-z plane. In that case, measurement of a point in both views yields two independent determinations of the z-coordinate, which may be compared. Distributions of the difference between the redundant coordinates indicated that a mean error of 0.4 in. in chamber space was to be expected in each coordinate. This same magnitude of error was also present in repeated measurements of the same point by different measurers.

In large part, due to mistakes made by the measurers, only 70% to 90% of the events which were to be measured on a typical roll of film could be accepted by the analysis programs and put on the library tapes.

A list was made of the events which had been deleted by the programs, and these were remeasured at a later time.

A set of summary tapes, one for each energy, was made to use repeatedly as input for the various analysis programs. Only the geometrical information about the track positions for each event was contained in these tapes.

To calculate the laboratory scattering angle of each track, the following recipe was used: The origin of the coordinate system was taken to be at the center of the liquid hydrogen target, with the positive z-axis perpendicular to the exit spark chamber, pointing in the general direction of travel of the beam particles. Each event was assumed to originate at $z = 0$, with x and y coordinates of the particular beam trajectory of that event at $z = 0$. The line of travel of the decay photon was determined by two points--the origin of the event, and the beginning point of the outgoing track in the chamber. The cosine of the scattering angle was calculated by the dot product of the beam trajectory and the line of travel of the decay photon.

C. Selection of Data

Several criteria were used to select from all the measured events those to be used in the detailed analysis.

1. One-Shower/Two-Shower Ratio

To make a quick check on the operating condition of the chambers, the ratio of the number of one-shower events to the number of two-shower events on each roll of film as totaled by the scanners was compared with all other rolls of film taken at the same beam energy. If there was some malfunctioning of one or more chambers during a roll, the ratio would be abnormally high, and that particular roll would be discarded.

2. Aluminum Region Cutoff

As was explained in the section describing the spark chambers, the inside four plates of each spark chamber in the cube were made of 1/16-in. aluminum, instead of steel. This region of the chambers was intended to make the paths of any charged particles visible, but have a low probability of initiating photon showers. However, this probability of shower conversion was not negligible. Even if traveling perpendicular to the plates, each of the photons from η decay had to pass through slightly more than 1/4-in. of aluminum, and there was almost a 4% chance that each one would undergo materialization. Therefore, if all the tracks beginning in the aluminum region were rejected, about 8% of the good events would be lost.

In spite of this fact, an aluminum region cutoff was applied in the selection of data, in order to insure that the sample of events was not contaminated by charged particles. The number of good η events thrown out in the process could be calculated rather accurately and a correction applied to the data at a later stage.

The observed distribution of the number of showers which convert at a given depth of penetration in a spark chamber, as a function of the depth, is shown in Fig. 16. The zero of the axis giving the depth of penetration is chosen to be at the outside edge of the innermost steel plate, i.e., at the beginning of the first gap where showers which converted in a steel plate can be observed. Because of the resolution errors in measurement, the peak occurring at the first steel plate overflows into the aluminum region by approximately 0.75 in. Because of this, the aluminum region cutoff was chosen so as to include events in which one or both of the showers converted less than 0.75 in. before the first steel gap.

This cutoff was applied only in the portion of each chamber that was directly exposed to the hydrogen target. At the edges of the cube, it could happen that a photon would pass through part of one chamber, out the end of it, and into a second chamber. In the cases where the photon showered in the second chamber, the aluminum cutoff was not applied, because the photon had necessarily passed through a 1/4-in. steel plate at the end of the first chamber and would be expected to be showering already in the aluminum region of the second chamber.

3. Shower Deviation Angle Cutoff and Full-Empty Subtraction

In addition to passing through the liquid hydrogen, the beam particles also penetrate the ends of the Mylar flask containing the liquid hydrogen, the Mylar windows of the vacuum dome, and the counters in the vicinity of the hydrogen target. Therefore, a fraction of the interactions occur in those places. Since the scattering from a proton bound in a large nucleus is not the same as the scattering from a free proton, these events must be removed from the sample of data to be

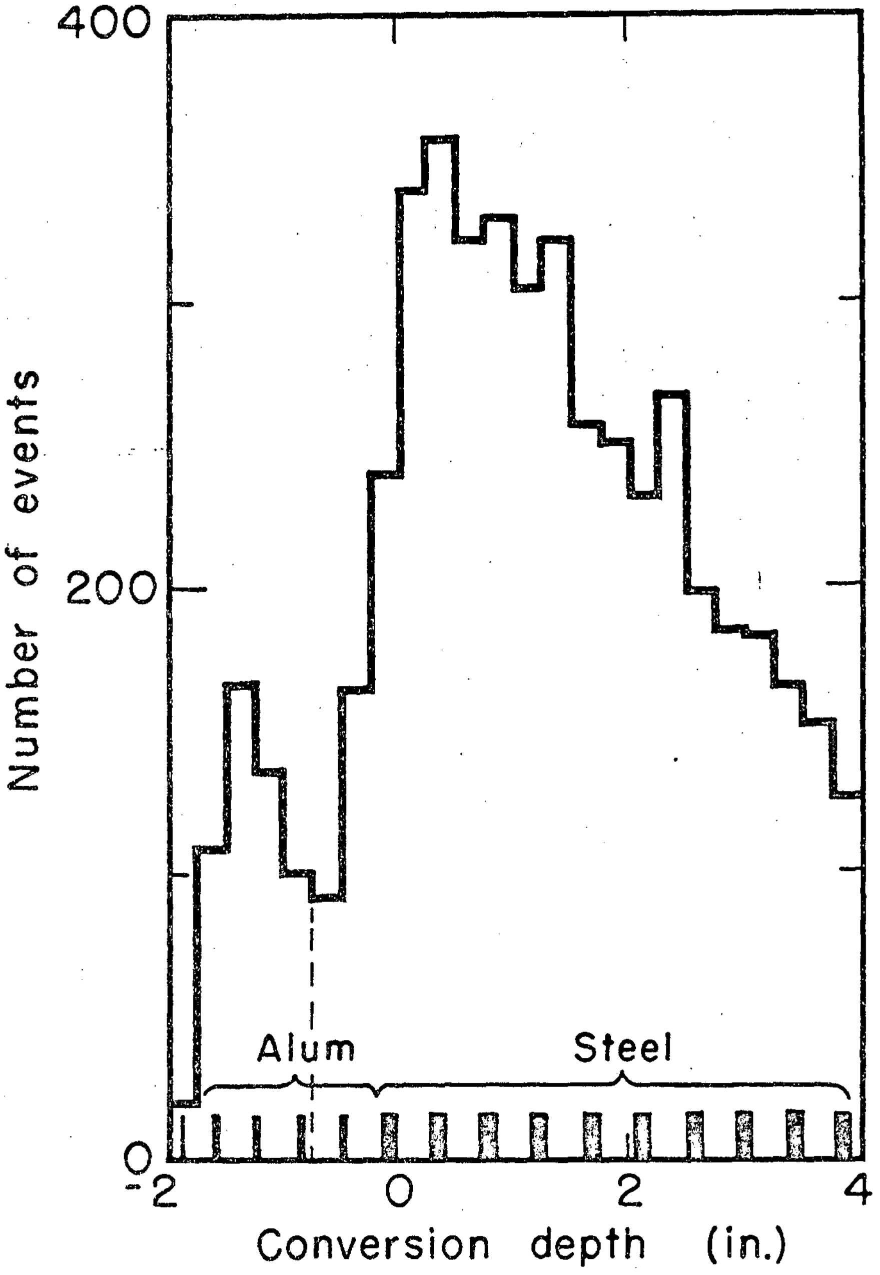

MU-36836

Figure 16. Distribution of the number of events which converted at a given depth of penetration into the spark chambers, as a function of depth. Events which converted before the depth indicated by the dotted line were rejected.

analyzed in order to eliminate any possible bias. Fortunately it is a simple matter to study these spurious interactions by taking data while there is no liquid hydrogen in the target.

An attempt was made to decide whether or not each individual event originated in the target, in order to reject those that did not. This was done by considering the deviation of the shower direction from a line between the center of the target and the beginning of the shower. Separate distributions of this angle of deviation for different intervals of shower lengths were made for both target-full and target-empty data, and a subtraction made. In each net distribution a deviation angle δ_{cut} could be chosen such that no shower produced by a photon originating in the target would be expected to deviate by more than that from the line to the center of the target. A graph of this cut-off angle as a function of length is given in Fig. 17, where it can be seen that the deviation angles become quite large.

However, this is to be expected, because of the following reason: Although showering does take place in a direction generally along the line of travel of the original photon, if the first few electrons undergo much multiple scattering, the shower may develop in a slightly different direction. The expected amount of multiple scattering can be roughly calculated as follows: If an electron of momentum p and velocity v passes through a thickness of material L with radiation length L_{rad}, the root mean angle of scattering is[23]

$$\theta_{rms} = \frac{21}{pv} \sqrt{\frac{L}{L_{rad}}} .$$

For a 50 MeV electron passing through one 1/8-in. steel plate, θ_{rms} = 11.5 deg.

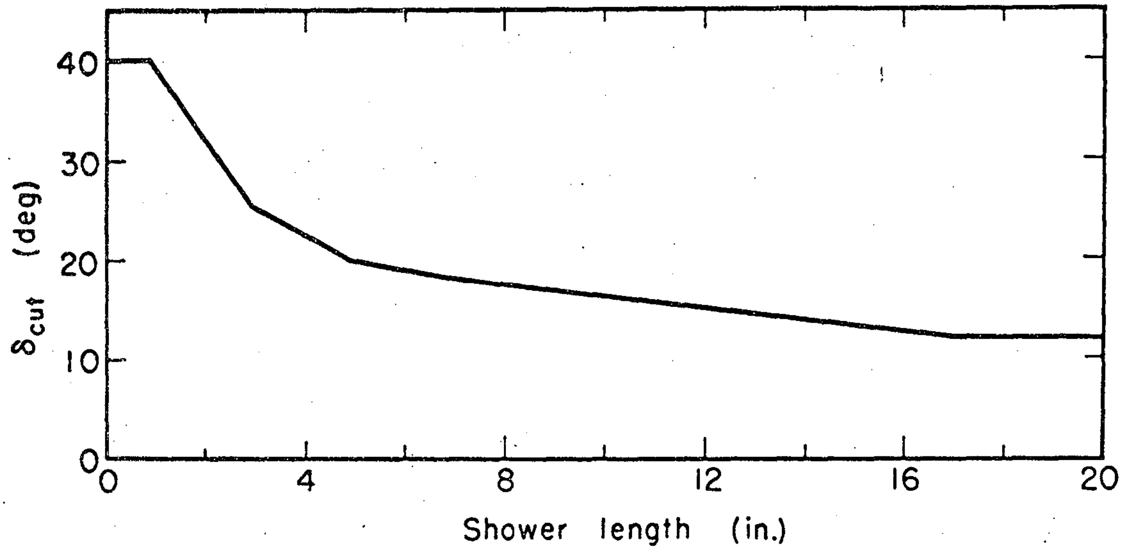

MU-36831

Figure 17. Maximum expected angle of deviation of a shower from the line of travel of the initiating photon, as a function of the length of shower. Events with a larger deviation angle were rejected.

It is apparent that one can never eliminate by a cutoff on deviation angle all events from the target-full data which came from interactions in the apparatus structure rather than in the hydrogen. First, an event which originates in some object on the beam line, with photons that scatter in the forward or backward direction, appears to have come from the target, regardless of whether it did or not. In addition, a photon which did not come from the target could produce a shower which, after large multiple scattering, appears to point towards the target. In fact, about 40% of the events with opening angles characteristic of η decay survived after the deviation angle cutoff was applied to a sample of data taken with the target empty.

Since the invalid events cannot be completely weeded out of the hydrogen data, it is evidently necessary to make all distributions from both the target-full data and the target-empty data, normalize properly the target-empty distributions, and subtract them from the target-full. However, because of the statistical fluctuations in the relatively small sample of target-empty data, it is still advantageous to apply the shower deviation angle cutoff to both full and empty samples before the subtraction. The length-dependent δ_{cut} of Fig. 17 was used in making this cutoff.

In Appendix A the derivation of the normalization factor for the full-empty subtractions is given.

D. Kinematical Information

Because there is no better place to put this section, the more or less logical development of the past few sections is interrupted at this point to provide various kinematical details. These are gathered together in tables and graphs to use for reference in the rest of the thesis.

Table I gives the numerical values of the particle masses used in all calculations.

Table I. Masses of particles

Particle	Mass (MeV)
π^-	139.6
p	938.2
π^0	135.0
η	548.7
n	939.5

In Table II are found the seven different energies of the pion beam at which data relevant to η production were taken, and also the pion energy at the η production threshold.

Table II. Beam energies of this experiment

Incoming pion kinetic energy (MeV)	Incoming pion momentum (MeV/c)	Total energy in c.m. system (MeV)	Momentum of η in c. m. system (MeV/c)	Velocity of η in c.m. system (c = 1)
561.3	686.8	1488.3	0	0
592.0	718.2	1507.5	115.9	0.2067
655.0	782.2	1546.2	202.9	0.3468
704.0	832.0	1575.7	250.7	0.4155
875.0	1005.0	1674.4	373.0	0.5622
975.0	1105.8	1729.5	429.1	0.6161
1117.0	1248.8	1804.9	498.5	0.6724
1300.0	1432.8	1897.6	576.1	0.7241

As described in the Introduction, the angle subtended by the two decay photons in the π-nucleon center-of-mass system obeys a distribution function which is sharply peaked at a minimum opening angle. The most important parameters which determine this distribution are the masses of the particles in the interaction and the kinetic energy of the beam particle. Together these fix the velocity of the neutral meson in the c.m. system, and as a result the minimum opening angle. Presented in Fig. 18 is a graph of the minimum angles for π^0 and η decay as a function of the incoming pion kinetic energy. The minimum opening angle for η decay is an especially sensitive function of the pion energy near threshold.

At each energy a range of opening angles about the η peak was defined from which to choose events for analysis. The upper limit of the region was chosen so that in a theoretical opening angle distribution, approximately 75% of all η's would have opening angles between the minimum angle and that upper limit. Since the observed distribution is slightly smeared because of the momentum spread of the beam and the experimental resolution in measuring the angles, there are events below the theoretical minimum. Therefore, the lower limit of the η region was set slightly below the theoretical minimum opening angle. Listed in Table III are the theoretical minimum η opening angle and the limits of the η region at each energy.

It is important to know the laboratory energy spectrum of the γ-rays from η decay when considering how many events are not seen because of the inefficiency of the spark chambers for detecting low energy photons. For η's that scatter into a fixed angle, this energy spectrum is flat between the limits $1/2(E_\eta \pm p_\eta)$, E_η and p_η being the laboratory energy and the momentum of the η at that angle.[8] Thus the complete energy

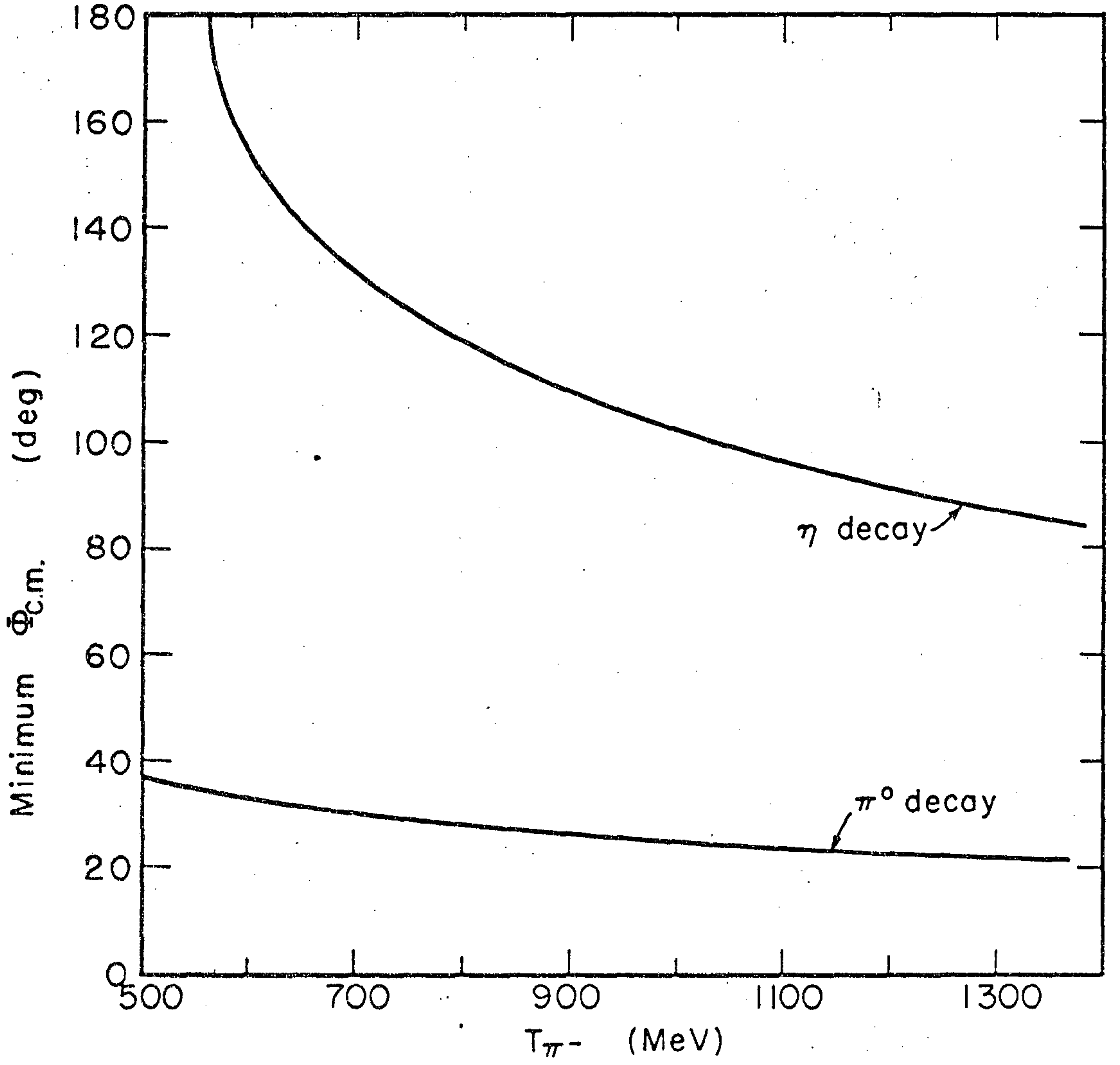

MU-36828

Figure 18. Minimum c.m. opening angle for γ-rays from π^0 and η decay, as a function of laboratory beam energy.

Table III. Opening angles of eta region.

Beam energy (MeV)	Lower limit of eta region (deg)	Theoretical min. opening angle (deg)	Upper limit of eta region (deg)	Theoretical fraction of events included (%)
592	152	156.14	168	87
655	136	139.42	154	78
704	126	130.90	148	78
875	106	111.58	134	78
975	100	103.94	126	76
1117	92	95.49	120	77
1300	84	87.21	110	75

spectrum is an integral over these flat spectra, weighted by the laboratory angular distribution of the η. In Fig. 19 the curve marked 100% is the complete spectrum for a beam pion energy of 1117 MeV.

At each η scattering angle, the extremes of the laboratory γ-ray energy spectrum occur in the case where one of the photons continues in the same direction that the η was traveling, while the other one goes exactly backwards. This situation also corresponds to the maximum 180 degree laboratory opening angle. While this opening angle is not the same when seen in the π-N c.m. system, it is still true that when events with the largest c.m. opening angles are not considered, the maximum and minimum possible laboratory photon energies are closer to the average. The spectrum labeled 75% in Fig. 19 corresponds to the laboratory energy spectrum when only the lowest 75% of the events, ordered by opening angles, are used for analysis.

Shown in Fig. 20 are the maximum and minimum laboratory γ-ray energies as a function of beam energy in the range of this experiment, for the cases that 100%, 80%, or 60% of the η events are taken, in order of increasing opening angles.

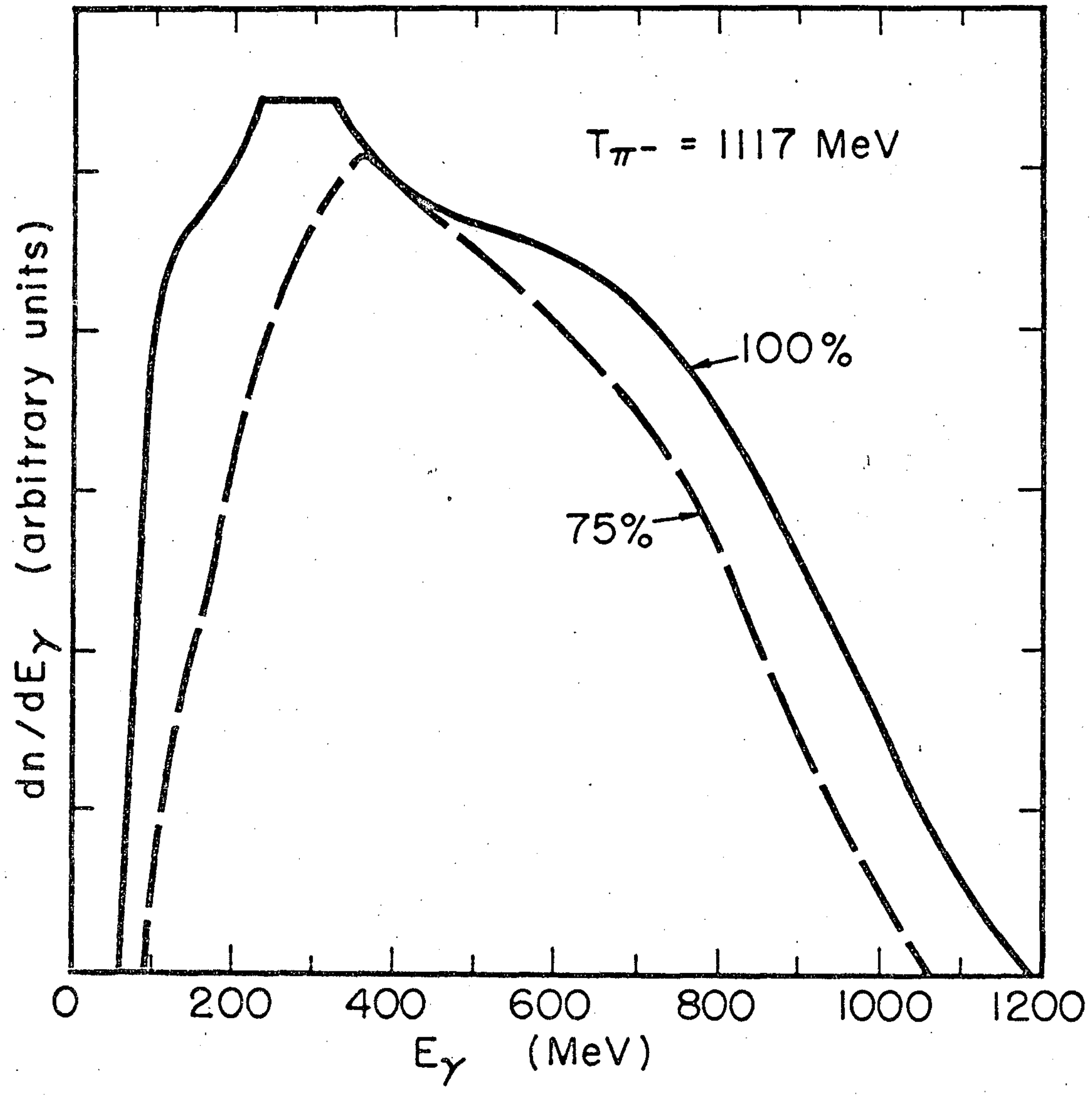

MU-36834

Figure 19. Laboratory energy spectrum of γ-rays from η decay at a beam energy of 1117 MeV. If only the 75% of the events with the smallest c.m. opening angles are considered, the energy spectrum shrinks to that given by the dashed lines.

It may be noted that when using a 75% cutoff, as is done in this analysis, only at the highest two energies are there any γ-rays at all with energy lower than 100 MeV, with the pleasant consequence that relatively few η events are lost due to the inefficiency of the spark chambers. This will be discussed quantitatively in the next section.

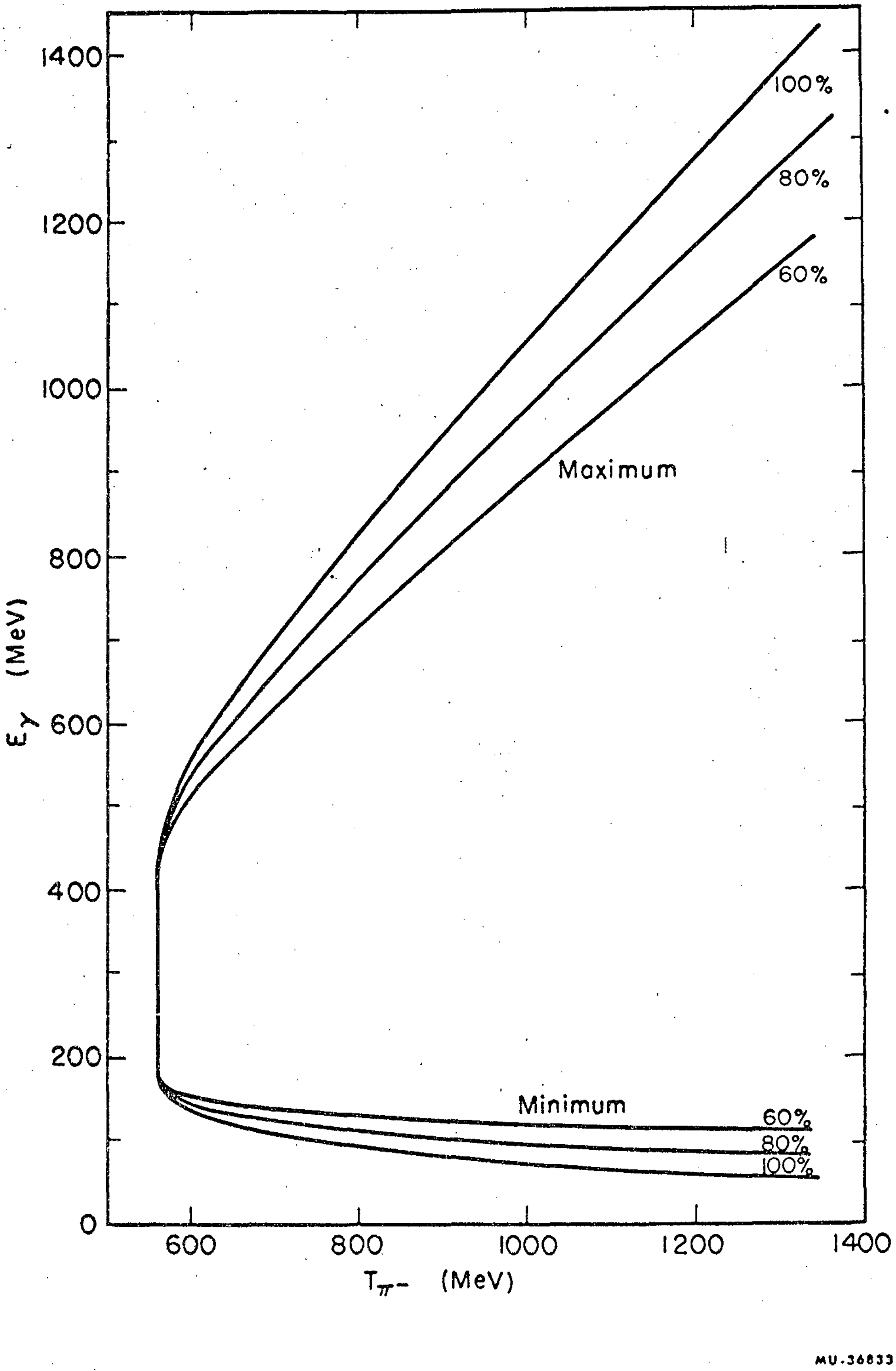

Figure 20. Maximum and minimum energies of photons from η decay as a function of beam energy, for various selections of opening angle range.

E. Detection Efficiency of the Chambers

1. Probability of Detecting a Shower

In order to be able to estimate the fraction of the η and π^o decays which produce two visible showers, a study was made of the detection efficiency of the chambers.[14a] This was done in terms of a particular model, according to which the probability that a given photon yields a visible shower is only a function of its energy.

Thus the local variations in detection efficiency of the chambers were ignored. For example, each spark chamber was slightly more efficient in the corner nearest the spark gap than in the diagonally opposite corner. Moreover, the neon gas had a slight tendency to accumulate at the bottom of the vertical chambers, so that they were less efficient at the top. Sometimes, because of insufficient gas supply to one gap, a chamber, or the whole cube, the efficiency of a larger area changed.

To get a quantitative estimate of the non-uniformities, the distribution in the number of showers detected as a function of the azimuthal angle was studied. Since the target was unpolarized, no preferred azimuthal direction existed, and therefore this distribution of final state photons must be uniform. For five different ranges of scattering angle, the distributions of showers detected vs. the azimuthal angle were made in eight bins. These were then least-squares fitted by a constant straight line. Typically, the χ^2/d parameter of the resulting best fits indicated only a 5% chance that the variations in the number of events in the various bins were due to purely statistical fluctuations.

Also ignored in this model was the angle at which the photon entered the chambers. However, this was not a serious approximation. Since for a trajectory normal to the plates, there were four mean conversion lengths of steel in each chamber, about a 2% chance existed that a high-energy photon traveling perpendicular to the plates would escape materialization. An angle of entrance to a chamber face of less than 45 deg to the normal could not increase the path length of material traversed enough to improve this significantly.

It is clear that simplifying the detection efficiency to merely a spatially isotropic energy dependence is somewhat of an approximation. However, it would be extremely difficult to try to include all of the above effects, some of which change with time, in any very exact fashion which would still be manageable in extensive calculations. The similarities in the results obtained when using various possible forms for the detection efficiency lead one to believe that the simple function to be described is adequate for the problem at hand.

The two salient features of the detection efficiency function are that it has an energy threshold, and that it becomes practically 100% for a high energy photon. Hence an exponential form was chosen for the probability ϵ that a photon with energy E_γ would produce a visible shower; namely

$$\epsilon = \begin{cases} 1 - e^{-\frac{(E_\gamma - E_t)}{E_c}} & \text{for } E_\gamma > E_t \\ 0 & \text{for } E_\gamma < E_t \, . \end{cases} \qquad (5)$$

There are two parameters: E_t is the detection threshold energy, and E_c determines how steeply the function rises toward unity. There is no physical reason to expect that the efficiency function should be exactly exponential, especially in the approximations used here. However, it has the correct general features stated above, and in addition is concave downward, which corresponds to the rapid decrease at low energies of the electron pair-production cross section.

In order to calculate the threshold detection energy E_t, the actual individual shower histories from Wilson's Monte Carlo calculations for lead[24] were adapted for steel. Since our definition of a minimum track required sparks in three consecutive gaps, the histories were used to study the probability that the longest range shower electron would travel through 3/8 in. of steel. As this probability was found to vanish for shower electrons produced by photons of less than 15 MeV energy, the value E_t = 15 MeV was fixed in all calculations.[25] This was an additional approximation, to the extent that the actual threshold varied somewhat in each case, depending on the amount of steel which had to be traversed to produce sparks in at least three gaps. An error would be introduced by this approximation if most of the photons had energies near the detection threshold, but it has been observed that γ-rays from η decay are of relatively high energy.

It remained to fix the shape parameter E_c by analysis of the experimental data. With the aid of Monte Carlo computer programs, this was done. Monte Carlo programs were used extensively in the study of the data of this experiment, to determine what would be observed in our spark chambers if various processes occurred with different detection efficiencies. In this case, the number of one-shower events and the number of two-shower events with opening angles in the region of the π^0 peak were calculated for charge exchange, $2\pi^0 n$, and $3\pi^0 n$ final states, assuming different values of E_c. By comparison with the experimentally observed ratio of one-shower to two-shower events (in π^0 peak) a value of E_c was chosen at each beam energy of the experiment.

These values of E_c are listed in Table IV. All are within 7 MeV of 72 MeV except at T_{π^-} = 704 MeV, where it is 92 MeV. Differences in the value of E_c at different beam energies reflect the variations in operating conditions, and the approximate nature of the efficiency function used. To give an indication of the resultant detection efficiency, also given in the table are the calculated probabilities of detecting the lowest energy photon which could come from an η decay, when events with opening angles in the peak regions defined in Sec. III. D. are analyzed.

Table IV. Parameters of efficiency function.

T_{π^-} (MeV)	E_c (MeV)	Detection efficiency for minimum energy photon (%)
592	73	84
655	70	82
704	92	70
875	69	73
975	66	72
1117	75	66
1300	72	65

2. Probability of Conversion in Aluminum Region

To include the probability that the photons impinging on the chambers produce a shower beginning in the aluminum plates, the results of a Born approximation calculation of the pair-production cross section were used.[26] This probability was expressed

$$p_{Al} = 0.0159 \cdot f(E_\gamma) \cdot t(\text{in}), \qquad (6)$$

where $f(E_\gamma)$ is an energy-dependent factor plotted in Fig. 21, and t is the thickness of aluminum penetrated, in inches. In calculating the numerical factor, the term Z^2 in the theoretical result was replaced by $Z(Z + 0.8)$, (where $Z = 13$, the atomic number of aluminum), to account for the contribution of the atomic electrons, with screening.

3. Monte Carlo Efficiency Calculation

The results of subsections 1 and 2 above were combined in one large Monte Carlo calculation to investigate the effect of the fractional probability of detecting the photons in our chambers, and the effect of throwing away all events which began in the aluminum region. Fake π^0 and η events were generated according to the preliminary experimental angular distributions at each beam energy. Also included was the momentum spectrum of the beam particles. Then the neutral meson decayed isotropically in its rest frame into two γ-rays. After a Lorentz transformation into the laboratory frame, the probability was calculated that each photon was observed, and that it converted in the aluminum or steel region of the chamber. The total conversion probability depended only on the laboratory energy of the photon, while the aluminum conversion probability depended both on the energy and also on the amount of aluminum it had traversed outside the cutoff line, a function of the angle at which the photon entered a chamber.

The results were expressed as a function of c.m. opening angle, Φ, in terms of the ratio of the original number of events generated in a particular opening angle bin to the number of these events which would

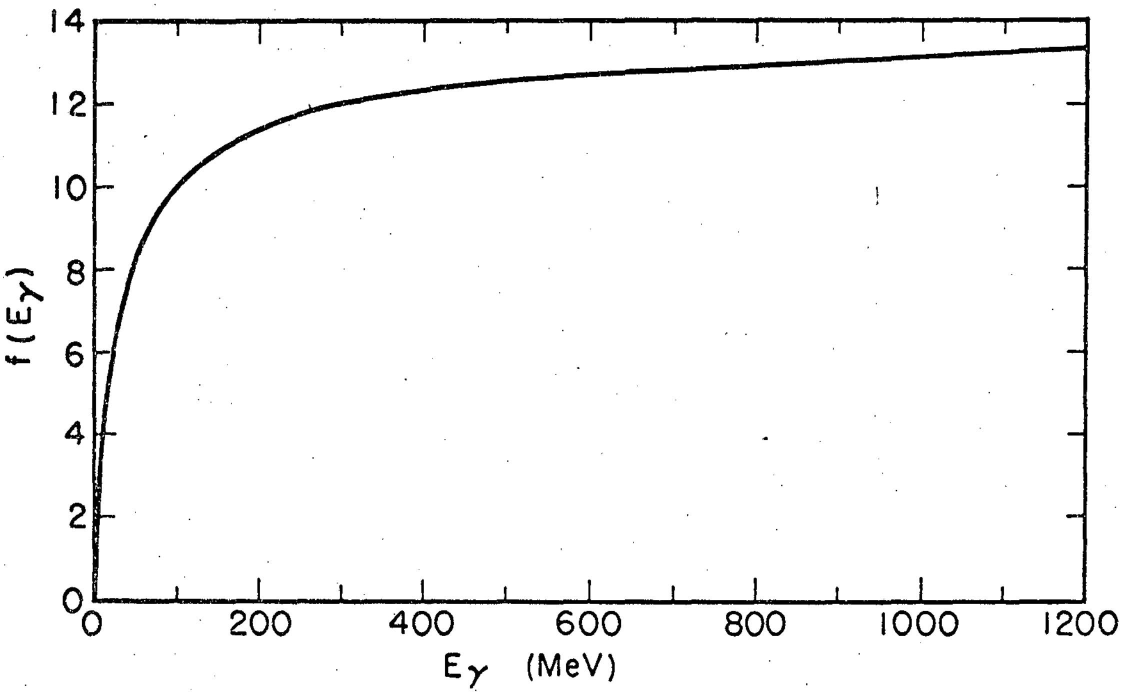

MU-36835

Figure 21. The factor $f(E_\gamma)$ used in Eq. (6).

be detected as two-shower events with both showers beginning in the steel plates. Shown in Fig. 22 is a plot on a logarithmic scale of this ratio for π^0 and η events at one energy. The spread in the data points at large opening angles arises because of the low statistics in the calculation; very few events have opening angles in that region. In each case the line is a graph of the expression

$$\text{Ratio} = e^{A + B\Phi + C\Phi^2} \tag{7}$$

where the variables, A, B, and C, have been determined by a least squares fit to the data points, and are listed in Tables V and VI. This fitted line was used in the total cross section calculation, as will be described in Sec. III. H.

Another way of expressing the result of this Monte Carlo calculation is to give the fraction of the η events in the peak regions of Table III which are observed as two-shower events with at least one shower converting in the aluminum region; and the fraction observed as two-shower events where both showers convert in the steel. These fractions are given in Table VII.

The final product of this program was a determination of the amount of distortion in the angular distributions of the γ-ray bisector caused by the inefficiencies and aluminum cutoff. In Sec. III. I. is explained the reason for considering the bisector. This distortion was expressed again as a ratio of the number of originally generated events in each angular bin to the number which were observed as two-shower events in the steel. At all energies, this ratio, as a function of bisector angle, was constant within ± 2%, so it is not given in detail.

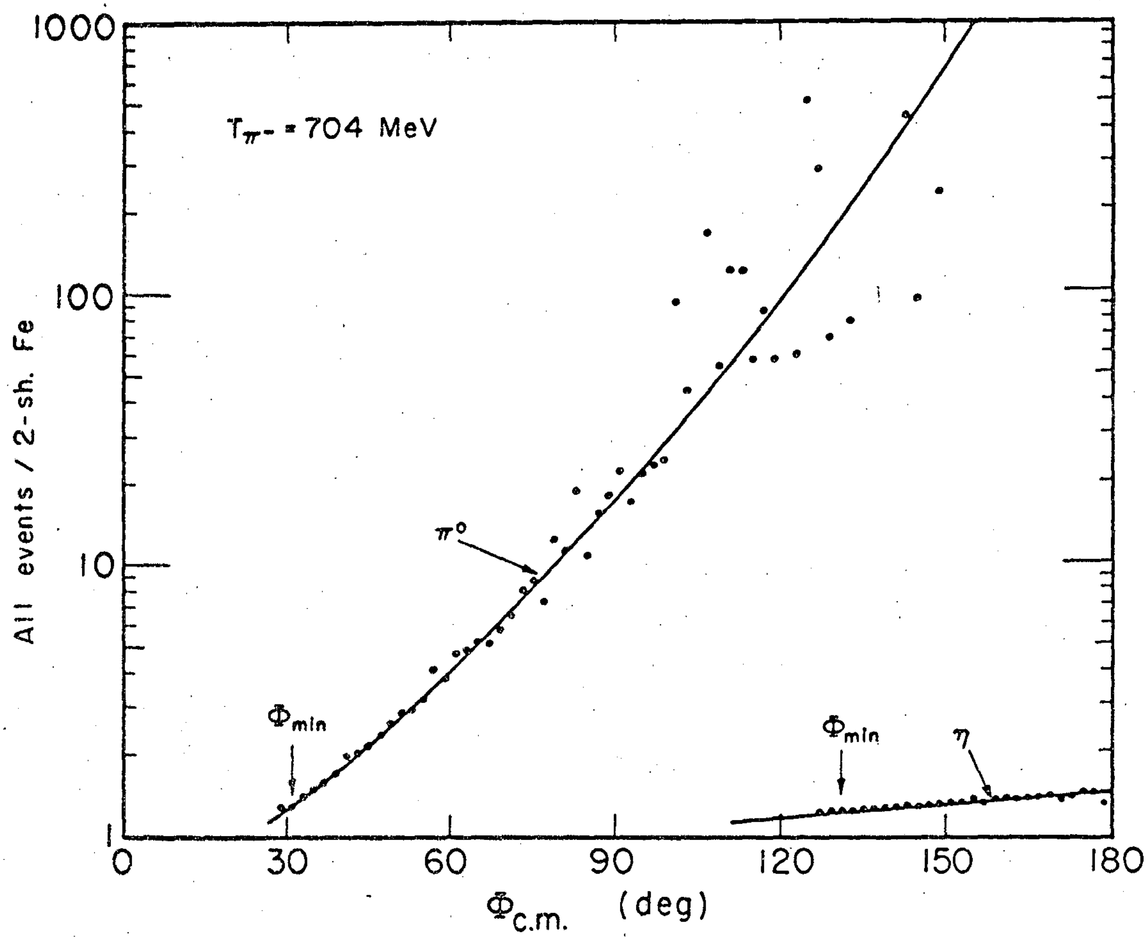

MU-36832

Figure 22. Ratio of the original number of events to the number that would survive to be seen as two-shower events in the steel region of the chamber. The lines are least-squares fitted to the data points, which were calculated for each opening angle by a Monte Carlo program.

Table V. Coefficients of the fit to the inefficiency ratio - π^0

T_{π^-} (MeV)	A	B (deg^{-1})	C (deg^{-2})
592	-0.34073	0.00515	0.00028
655	-0.44707	0.01168	0.00023
704	-0.68763	0.02604	0.00015
875	-0.40172	0.01424	0.00024
975	-0.36120	0.01273	0.00027
1117	-0.26059	0.00929	0.00034
1300	-0.21458	0.00768	0.00038

Table VI. Coefficients of the fit to the inefficiency ratio - η

T_{π^-} (MeV)	A	B (deg^{-1})	C (deg^{-2})
592	-0.04272	0.00215	-0.00001
655	-0.32657	0.00461	-0.00001
704	-0.58794	0.00803	-0.00002
875	-0.20619	0.00286	0.00000
975	-0.17766	0.00238	0.00000
1117	-0.31339	0.00459	0.00000
1300	-0.14976	0.00174	0.00001

Table VII. Observed fractions of η events in peak region as calculated by Monte Carlo efficiency program.

T_{π^-} (MeV)	Fraction observed as 2-showers in aluminum (%)	Fraction observed as 2-showers in steel (%)
592	9.29	84.56
655	9.47	85.71
704	8.96	81.02
875	9.62	86.35
975	9.78	87.31
1117	9.68	86.30
1300	9.81	87.74

F. Neutron-Proton Recoils

The neutral final states in this experiment include a neutron in addition to the mesons. Usually the neutron, being a long-lived neutral particle, escapes without having been detected. But occasionally it makes its presence known by colliding with a proton in one of the steel plates of the spark chambers, with a momentum transfer high enough to eject the proton, which then leaves a track in the spark chamber. This phenomenon is known as an n-p recoil.

As it turns out, it is not possible to distinguish visually between a low-energy, short-range proton track and a minimum electron shower. Consequently, there are among the sample of three-shower events some which really consist of two genuine showers and one proton track. The frequency with which these occur needs to be studied, because they represent a sub-sample of the two-shower events--both π^0 and η--which are not observed.

Therefore all three-shower events were tested to see if they would fit the n-p recoil hypothesis. Each possible pair of tracks in turn was assumed to be showers, and the direction of flight of the corresponding neutron was calculated. As will be explained in Sec. III. I. on the differential cross section, there are actually two solutions for the neutron direction. If the three following conditions were satisfied, then the event was accepted as an n-p recoil: 1) either of the two solutions was within 10 deg in the laboratory of being in the direction of the third track; 2) the third track was not a "bushy" shower; and 3) the calculated neutron energy was sufficient to eject a proton that could penetrate three steel plates. In such events, some correlation was found between the length of the third track and the range of the proton expected under the assumption that the n-p scattering was elastic. Also, the distribution of the depth in the chamber at which the alleged proton tracks began was much flatter than the distribution of shower starting points as pictured in Fig. 16, consistent with a low probability of occurrence.

In Table VIII the final results of this analysis are given, where the number of two-shower events in the peak opening angle regions (with both showers converting in the steel region) that also had an accompanying proton track are listed for π^0 and η mesons for each energy. These are used in the calculation of the total cross section.

In addition, there were in the sample of two-shower events a few fakes which were really one-shower and a proton track, the second shower not having been detected. These tended to lie at the upper end of a two-shower opening angle plot, because usually the high energy photon detected was from a π^0 decay, and was traveling in almost the same direction as the pion. Hence the angle between it and the neutron direction in the c.m. system was close to 180 deg.

Table VIII. Summary of 3-shower n-p recoil results

T_{π^-} (MeV)	No. of events in π^0 peak region	No. of π^0 n-p recoils in π^0 peak region	No. of events in η peak region	No. of η n-p recoils in η peak region
592	2070	24	220	3
655	1387	80	325	15
704	2474	183	664	34
875	1597	116	153	9
975	986	89	173	8
1117	1129	105	326	19
1300	2559	321	423	21

In an analysis which is to be based only on genuine two-shower events, these represent a contamination, and therefore must be treated as background. In order to study the characteristics of these events, a computer program was written to test all two-shower events for this hypothesis. Each "non-bushy" track in turn was assumed to be a proton track, and the other a shower. The event could be reconstructed as either a π^o or an η, and the energy of the hypothetical missing photon calculated. If the calculated energy was low enough that it was reasonable that the photon had been missed, and if the length of the alleged proton track was in reasonable agreement with a predicted range, a distribution was made of the opening angle of the two observed tracks. The result was always a broad peak with very few events below 150 deg, which corresponded to a definite observed excess of events in this region of the raw opening angle distributions of all two-shower events. After all subtractions and cutoffs were applied, these events may still be seen at 160 deg in Fig. 26. Use was made of this distribution as a background subtraction when calculating the total cross section. In Fig. 30 of Sec. III. H. will be found an example of this distribution.

G. Determination of T_{π^-}, $\Delta\Phi$, and $\Delta p/p$.

As was illustrated in Fig. 18, the minimum opening angle for η decay is an especially sensitive function of the beam energy near threshold. Thus one might expect to be able to determine the beam energy rather accurately by a careful study of the opening angle distribution. Even more information than that, however, can be gleaned from the distributions.

At any particular energy of the experiment, the detailed shape of the experimentally observed opening angle curve depends on the resolution of the spark chambers and optical system, and the momentum spectrum of the incoming beam particles. Either a momentum spread or a significant mean error of measurement results in a somewhat broadened distribution. These effects can be folded into the theoretical opening angle curve by numerically performing a double integration

$$\left.\frac{dn}{d\Phi}\right|_{\text{observed}}(\Phi,p) = \iint r(\Phi,\Phi',\Delta\Phi)\,s(p,p',\Delta p)\left.\frac{dn}{d\Phi}\right|_{\text{theoretical}}(\Phi',p')\,d\Phi'\,dp' \quad (8)$$

where $r(\Phi,\Phi',\Delta\Phi) = e^{\frac{-(\Phi-\Phi')^2}{2(\Delta\Phi)^2}}$ is the resolution of measurement, assumed Gaussian, which depends on $\Delta\Phi$, the mean error of measurement; and $s(p,p',\Delta p)$ is the momentum spectrum of the beam, which was taken to be trapezoidal in shape, with half-width at half-height of Δp. The spectrum s dropped from 1 to 0 in a 1% interval of $\Delta p/p$.

At each setting of the beam magnet currents, then, it should have been possible to determine the kinetic energy of the beam pions, the width of the beam momentum spectrum, and the angular resolution of the apparatus, by considering the location and shape of the η peak in the opening angle distribution. However, the statistical fluctuations in the experimental data did not allow differentiation between a large momentum spread with small error of resolution, and the reverse. The only really significant shape factor was the height of the peak for a given number of events.

Therefore the following procedure was adopted: At each energy the angular resolution was first estimated by a Monte Carlo calculation, which simulated the process of measuring the events. Mock events were generated according to the preliminary experimental distributions. Then the beginning of the showers and the x-y coordinates of the origin of the event were perturbed at random by an amount which obeyed a Gaussian distribution, with a standard deviation determined by studying the errors of measurement on the digitized protractor. For the showers, this was a standard deviation of 0.4 in. in space, and for the beam, it was 0.25 in. The result was a slightly smeared opening angle distribution, which could be fit by a theoretical curve with an angular resolution folded in to it. The best fit determined the estimate of the angular resolution of the apparatus to be used in all ensuing calculations.

Next, with a ± 2.5% momentum spread and the estimated angular resolution folded in, a theoretical curve and the experimental opening angle distribution were formed for a sequence of incoming pion kinetic energies. With the goodness of fit characterized by χ^2 summed over the region of the η peak, the theoretical curve which best fit the data determined the beam energy.

It has been shown in the previous section that over this range of opening angles, the inefficiency of the chambers did not alter the shape of the observed opening angle distribution by more than a few percent, which was well within the statistical fluctuations.

Then, with the estimated angular resolution and the kinetic energy for the theoretical curve set as described above, momentum spectra from 1% to 6% were fit to the experimental shape and the momentum spread of the beam determined, again by minimizing the χ^2. A summary of the results of this fitting procedure is presented in Table IX.

Table IX. Results of the opening angle curve fitting for T_{π^-}, $\Delta\Phi$, and $\Delta p/p$.

T_{π^-} by wire orbits (MeV)	T_{π^-} by fit (MeV)	$\Delta p/p$ (%)	$\Delta\Phi$ in π region (deg)	$\Delta\Phi$ in η region (deg)
581	592±3	2.75±0.75	1.87±0.15	3.02±0.07
650	655±5	2±1	1.79±0.15	2.86±0.15
698	704±4	3.75±1	1.73±0.15	2.74±0.15
873	875±10	2.50±1*	1.71±0.15	2.97±0.15
990	975±10	2.50±1*	1.71±0.15	2.76±0.15
1100	1117±8	2.50±1*	1.70±0.15	2.53±0.15
1311	1300±20	2.50±1*	1.59±0.15	2.72±0.15

*These values were assigned by studying the beam transport system, because the fit to the opening angle curve was not conclusive.

H. Eta Production Cross Section

The cross section for η production in the reaction under study is also calculated by fitting the opening angle distributions with theoretical curves, using the method to be described in this section. However, the fundamental quantity which can be derived by analysis of this distribution alone, is not the total η production cross section, but the ratio

$$R = \frac{f_\eta \cdot \sigma\,(\pi^- p \rightarrow \eta n)}{f_\pi \cdot \sigma\,(\pi^- p \rightarrow \pi^0 n)} \qquad (9)$$

where f_η is the branching ratio

$$f_\eta = \frac{\Gamma(\eta \rightarrow 2\gamma)}{\Gamma(\eta \rightarrow \text{all decays})} \cong 1/3\ , \qquad (10)$$

and f_π is the branching ratio

$$f_\pi = \frac{\Gamma(\pi^0 \rightarrow 2\gamma)}{\Gamma(\pi^0 \rightarrow \text{all decays})} = 98.8\%. \qquad (11)$$

The ratio, R, is the ratio of the number of events in the opening angle plot from η decay to the number due to π^0 decay; and it is free from all of the numerous possible errors which arise in measuring the total neutrals cross section with the counters, or in scanning and measuring the film, or in determining the η branching ratio. This branching ratio is particularly difficult to measure because the 2γ decay mode is only one of the neutral modes of η decay. In determining R, the main errors arise from the estimation of the detection efficiency of the chambers and the background reactions.

Once R has been determined, it can be multiplied by the charge exchange cross section, also measured in this experiment,[14a] to yield the partial η production cross section

$$f_{\eta} \cdot \sigma\,(\pi^- p \to \eta n). \tag{12}$$

To evaluate R a scheme is used which is a slight generalization of the well-known method of least squares.[27] The usual least-squares formalism is used to find the coefficients of a power series, or a Legendre polynomial series, which best fit a set of experimental data in the sense of a minimum X^2. Exactly the same method, derived by setting the derivatives of the expression for X^2 equal to zero, may be used to find the values of coefficients for a linear combination of any set of functions which best fit a set of data. Furthermore, the errors in the coefficients are automatically calculated in the process as part of the so-called error matrix.

The experimental data points were the final opening angle distributions at each energy, formed by applying the cutoffs of Secs. III. C. 2 and III. C. 3 to both target-full and target-empty distributions, and then making a full-empty subtraction. The data were binned in intervals of 2 deg, from 0 to 180 deg, so that there were 90 data points to be fitted in each distribution. Shown in Figs. 23 through 29 are these final opening angle distributions.

The functions used in linear combination to fit the experimental points were the following:

a. The η opening angle curve. To obtain the theoretical distribution, Eq. (8) was numerically integrated with the parameters fixed at the values in Table IX. Each point on this theoretical curve was then divided by the value of the fitted efficiency curve which had been calculated as explained in Sec. III. E. 3. Doing this distorted the shape of the opening angle curve slightly because large opening angle events were less likely to be detected than those near the peak. It also

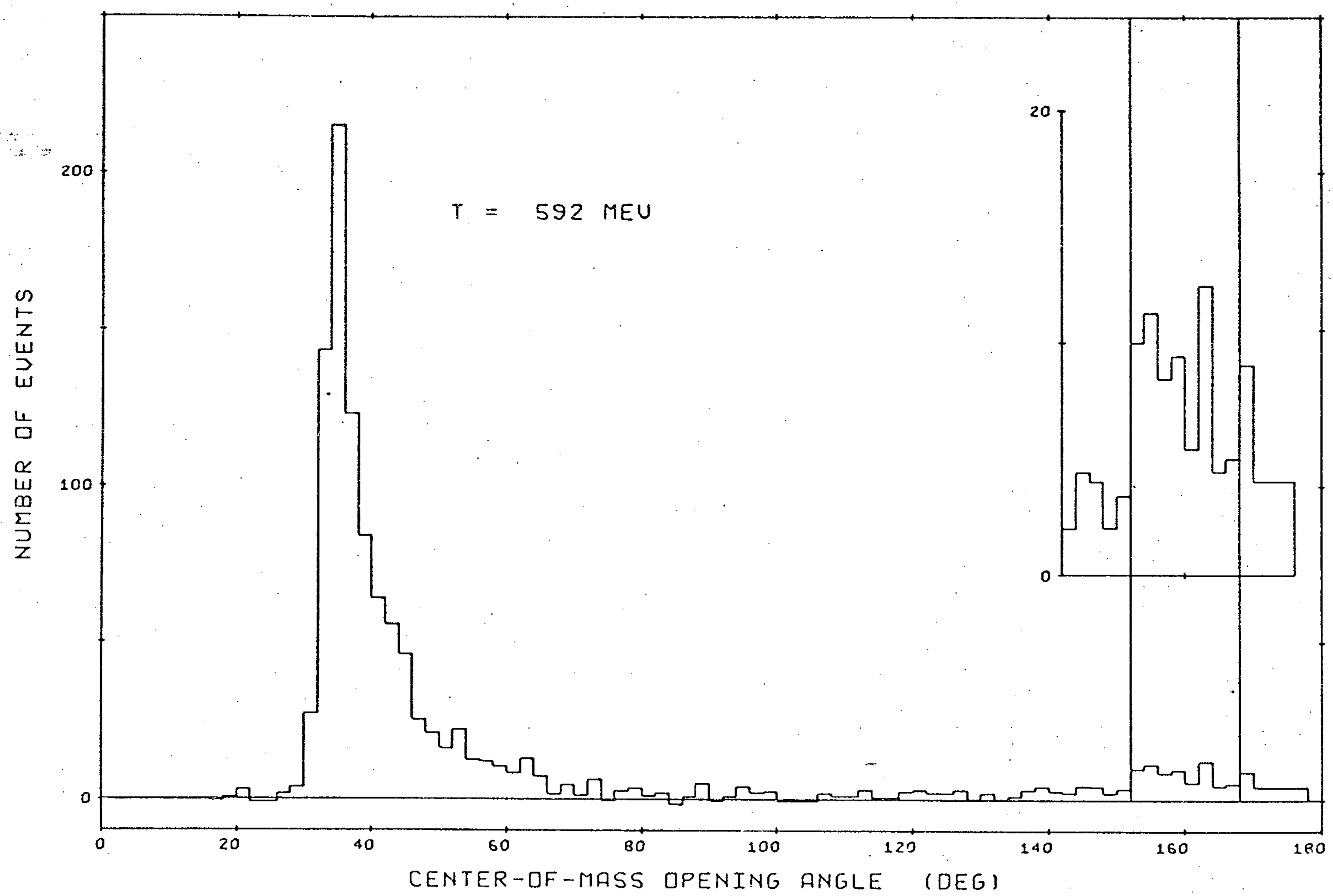

MU-36824

Figure 23. Experimental opening angle distribution for T_{π^-} = 592 MeV. The inset shows the region of the η peak with an expanded vertical scale. Events were chosen from the region between the vertical lines for the η differential cross section.

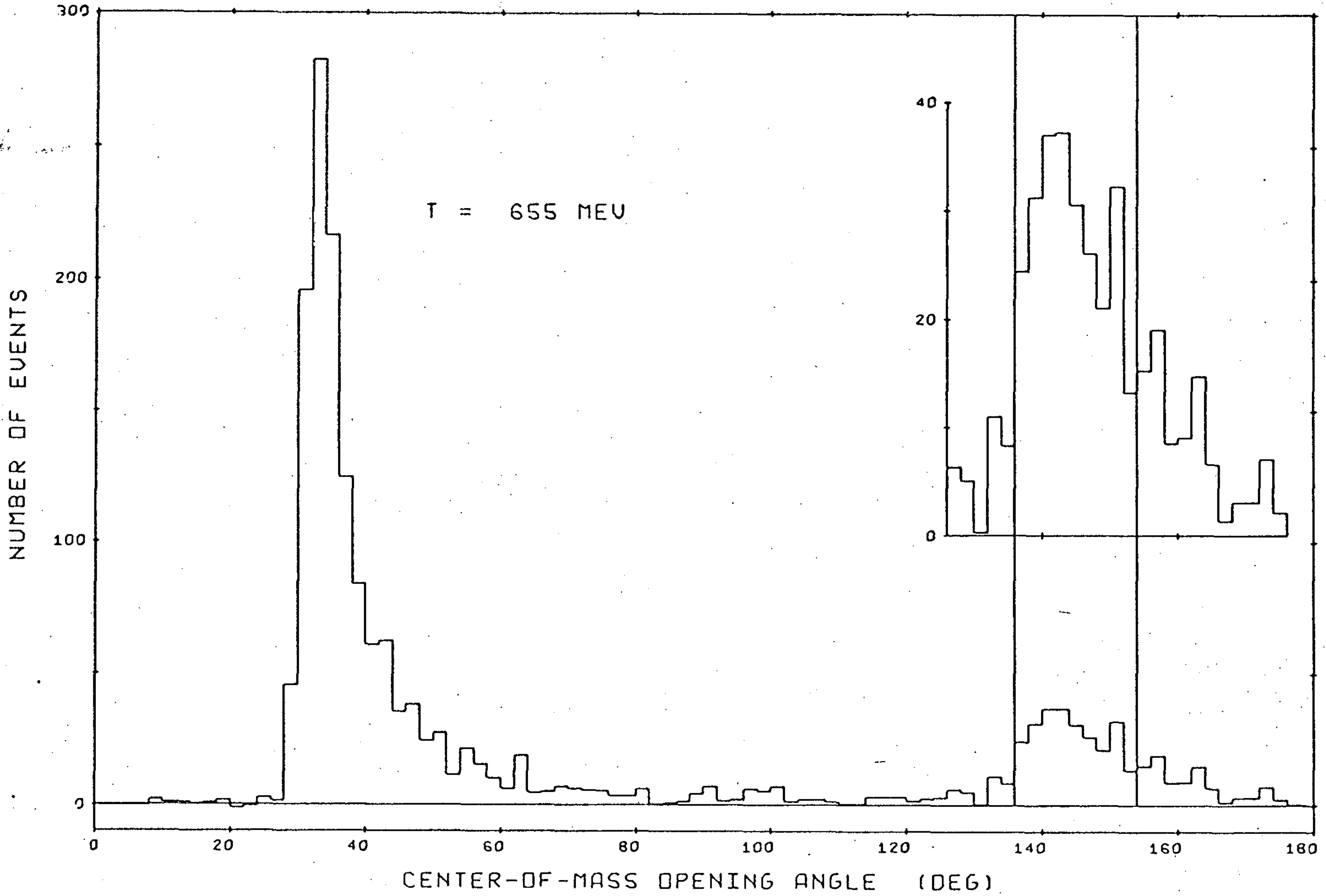

MU-36821

Figure 24. Experimental opening angle distribution for T_{π^-} = 655 MeV. The inset shows the region of the η peak with an expanded vertical scale. Events were chosen from the region between the vertical lines for the η differential cross section.

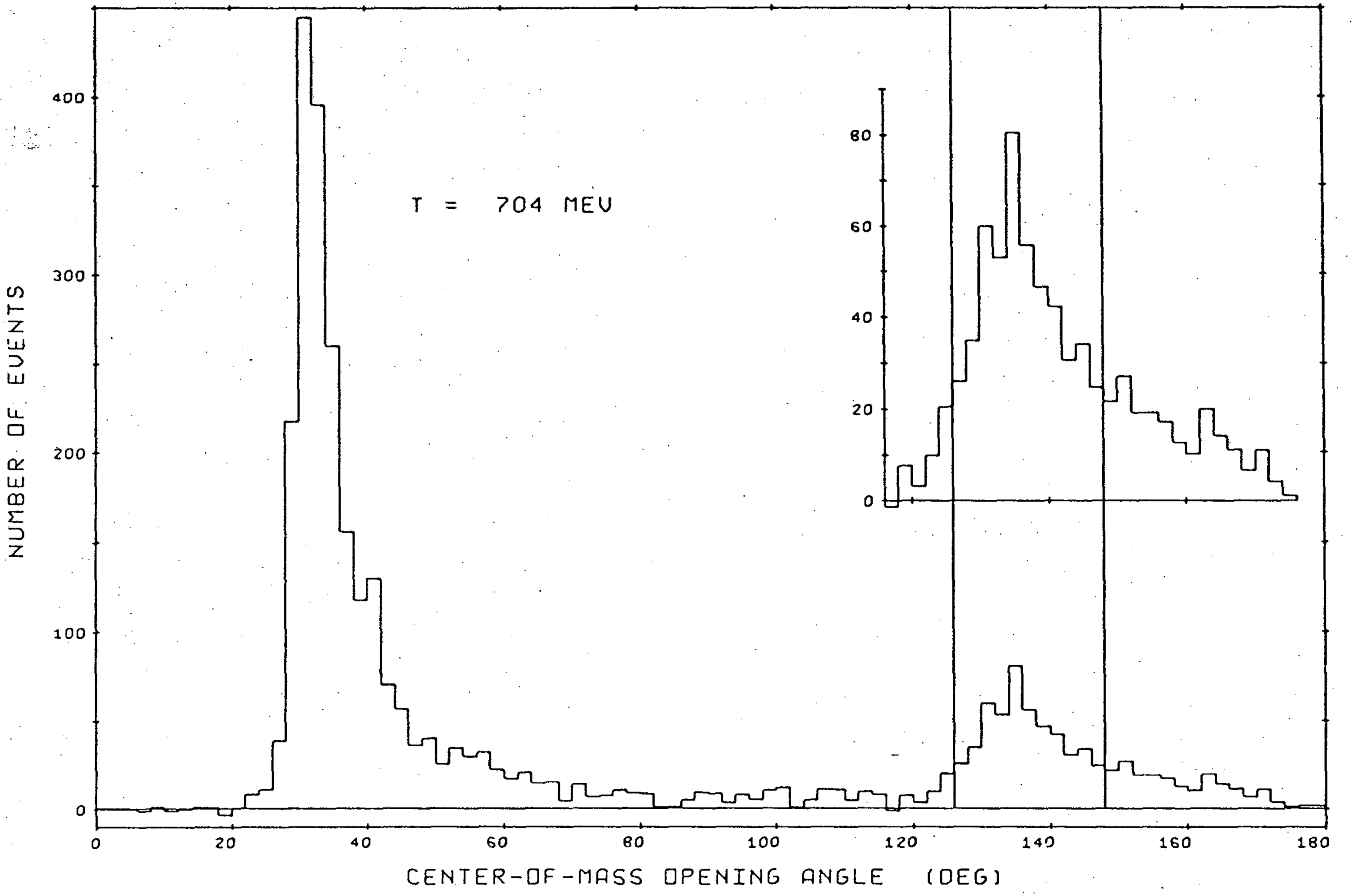

MU-36825

Figure 25. Experimental opening angle distribution for T_{π^-} = 704 MeV. The inset shows the region of the η peak with an expanded vertical scale. Events were chosen from the region between the vertical lines for the η differential cross section.

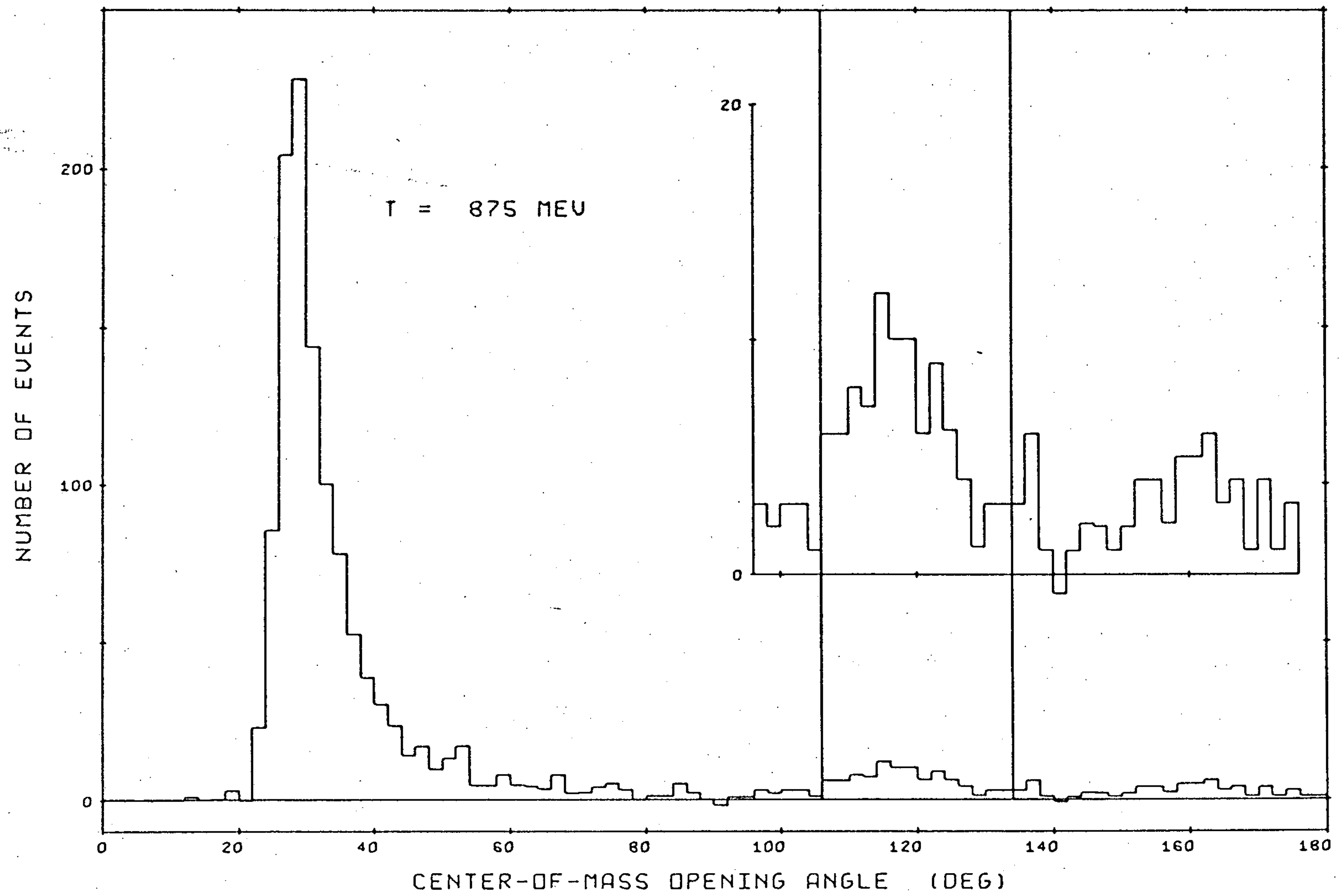

MU-36822

Figure 26. Experimental opening angle distribution for T_{π^-} = 875 MeV. The inset shows the region of the η peak with an expanded vertical scale. Events were chosen from the region between the vertical lines for the η differential cross section.

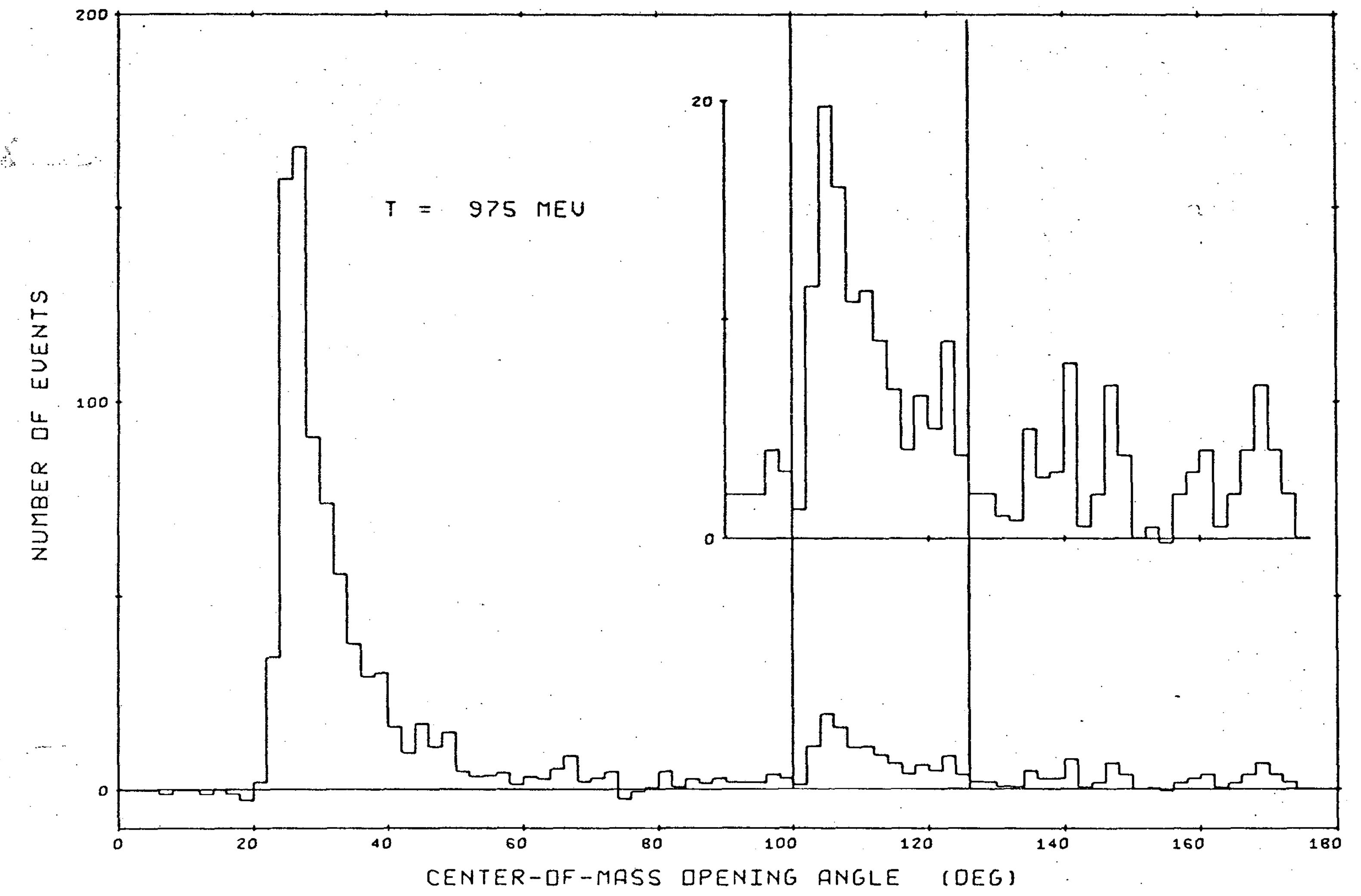

MU-36820

Figure 27. Experimental opening angle distribution for T_{π^-} = 975 MeV. The inset shows the region of the η peak with an expanded vertical scale. Events were chosen from the region between the vertical lines for the η differential cross section.

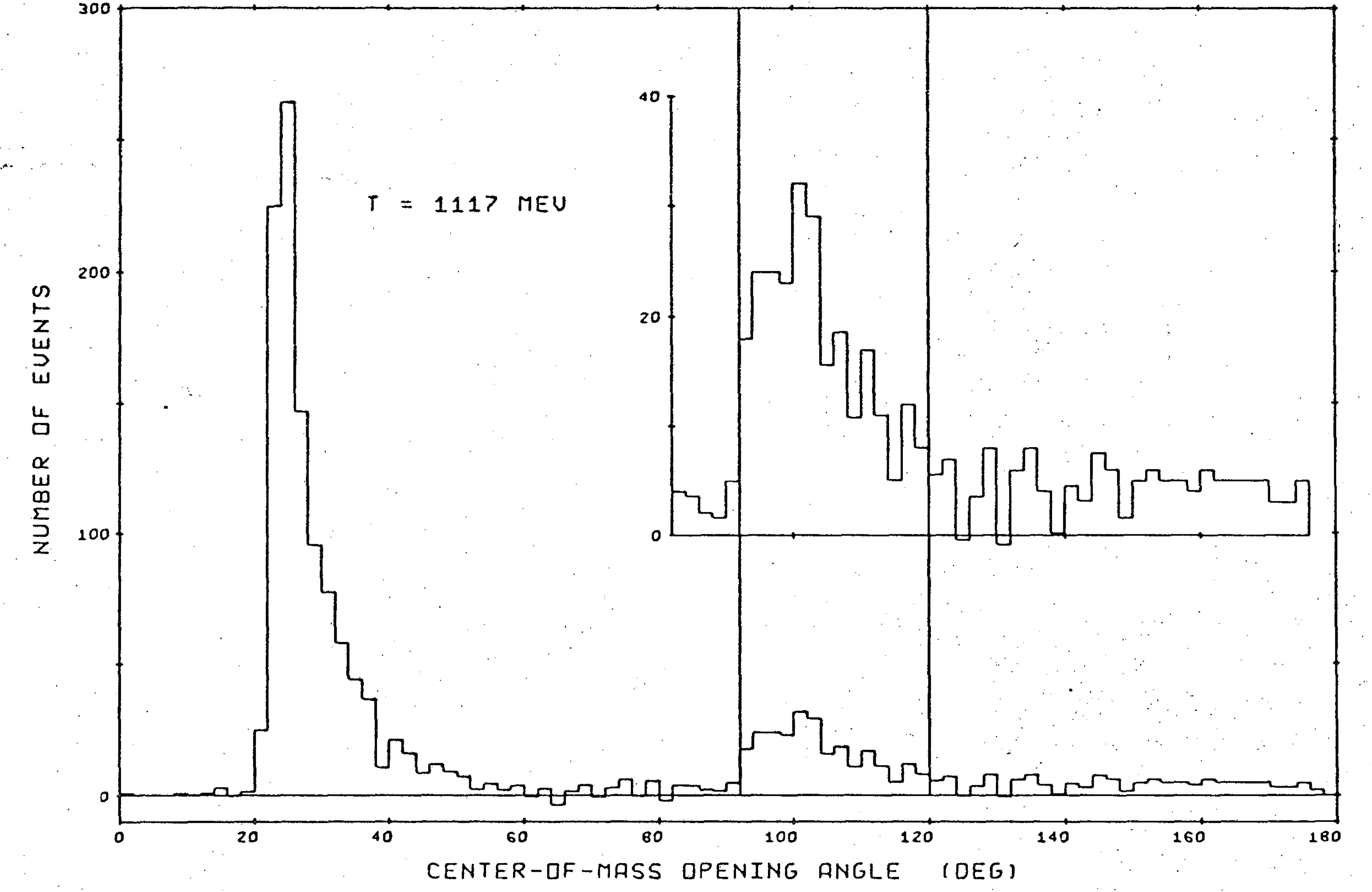

MU-36826

Figure 28. Experimental opening angle distribution for $T_{\pi^-} = 1117$ MeV. The inset shows the region of the η peak with an expanded vertical scale. Events were chosen from the region between the vertical lines for the η differential cross section.

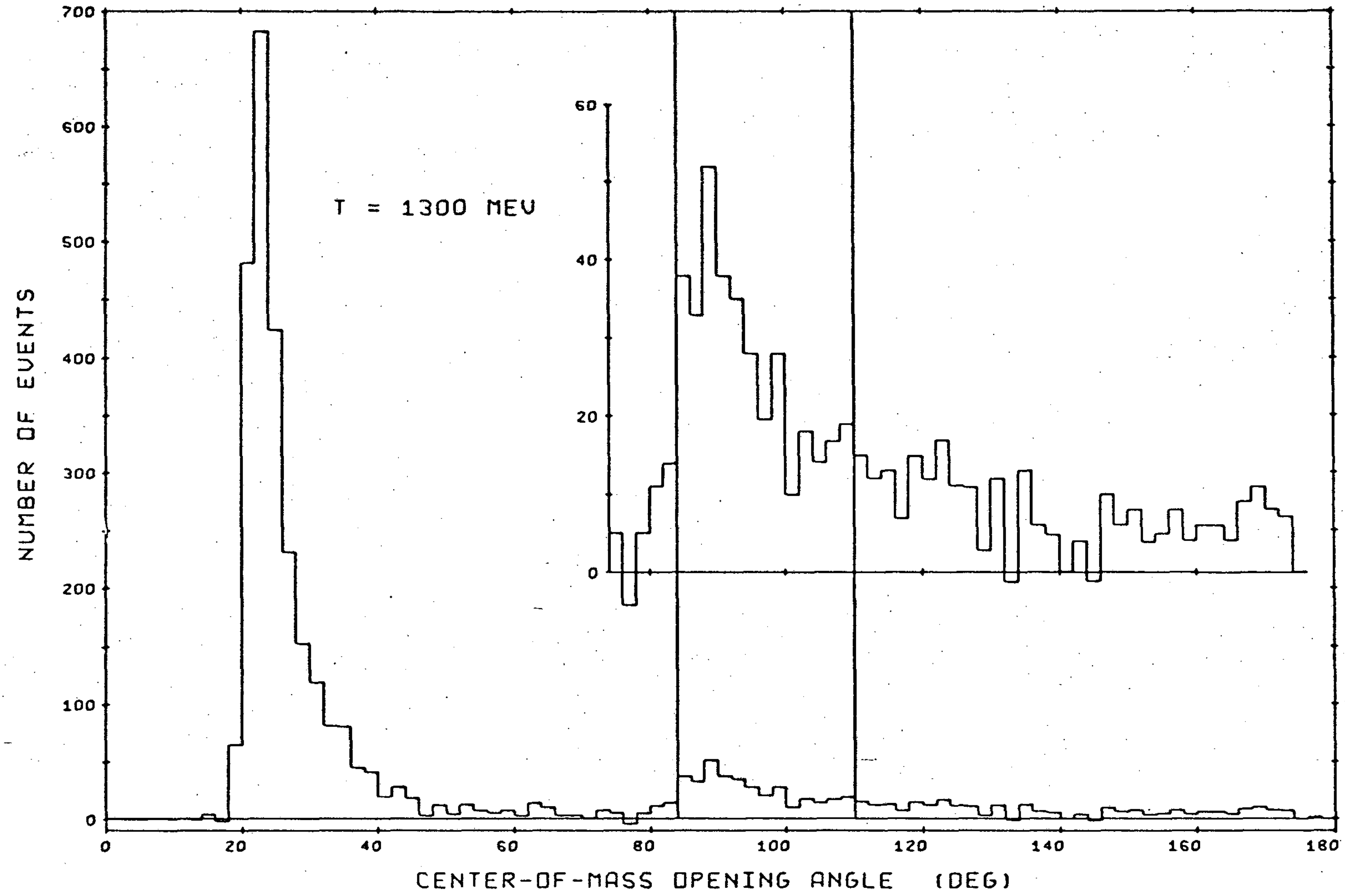

MU-36823

Figure 29. Experimental opening angle distribution for T_{π^-} = 1300 MeV. The inset shows the region of the η peak with an expanded vertical scale. Events were chosen from the region between the vertical lines for the η differential cross section.

determined the over-all fraction of the η events which would not be detected as two-shower events.

b. The π^0 opening angle curve. This was calculated in exactly the same way as the η opening angle curve, except that the π^0 parameters were used.

c. The $2\pi^0n$ background curve. Monte Carlo programs were used to estimate the shape of the contribution of various possible background reactions. In this case a sample of $2\pi^0n$ events was generated according to a three-body phase space distribution. In its rest frame each π^0 decayed isotropically into a pair of photons. Then the chamber detection efficiency function of Eq. (5) along with the aluminum region conversion function in Eq. (6), were used to calculate the probability that each possible combination of two out of the four photons would be the only ones detected, specifically in the steel region of the chambers. That is, if P_i^{Sh} is the probability that photon i produces a shower, and P_j^{Al} is the probability that photon j is converted in the aluminum plates, then the probability that photons 1 and 2 contribute a background two-shower event was calculated to be

$$P_{2\text{-}Sh} = P_1^{Sh} \cdot P_2^{Sh} \cdot (1 - P_3^{Sh}) \cdot (1 - P_4^{Sh}) \cdot (1 - P_1^{Al}) \cdot (1 - P_2^{Al}). \quad (13)$$

The opening angle between photons 1 and 2 was calculated and the probability $P_{2\text{-}Sh}$ was then added to the appropriate bin of an opening angle distribution. In this fashion an estimate of the shape of the two-shower background from $2\pi^0n$ production was formed.

d. The $3\pi^0n$ background curve. This was calculated by Monte Carlo methods in a similar fashion. It has been inferred from the rapid change in the cross section for six-shower events observed in this experiment as the η threshold is crossed that most of the $3\pi^0 n$ events are produced by the $3\pi^0$ decay of the η.[28] Therefore, in this calculation the $3\pi^0$'s were generated on the basis of this assumption, as resulting from η decay according to three-body phase space. The η's themselves were generated according to the preliminary angular distributions.

e. The ΛK background curve. At the four energies above the threshold for the reaction $\pi^- p \rightarrow \Lambda K^0$, this process was a possible contributor to the background.[29] A two-shower event resulted if the K^0 escaped from the chambers as a long-lived $K_2{}^0$, and the Λ decayed into $\pi^0 n$, the π^0 furnishing two photons. As the π^0 is of relatively low energy, the opening angles could be in the η peak region. A Monte Carlo calculation was done to estimate the shape of the opening angle distribution from this reaction, as it would be observed in our chambers. For simplicity it was assumed that the Λ's were produced with a c.m. angular distribution of $(1 - 0.8 \cos \theta_\Lambda)$, and the Λ decay asymmetry was ignored.

f. The ωn background curve. Our three highest energies lie above the threshold for ω production, and this is a possible background through the $\pi^0\gamma$ decay of the ω, if one of the photons is not detected. The γ-ray which comes out opposite the π^0 has a fairly high energy, so that it is usually one of the two photons from the π^0 decay which has the largest probability of being missed. The two detected γ-rays are then heading in generally opposite directions, and hence yield a large angle contribution to the opening angle distribution. In a Monte Carlo calculation the shape of this contribution was estimated using the assumptions that the ω production angular distribution is isotropic, and that there is no decay asymmetry.

g. The n-p recoil background curve. The origin of these events is described in Sec. III. F. Of concern here are the proton tracks that occur in conjunction with only one shower, the other shower not having been detected, so that what should be a one-shower event masquerades as a two-shower event. Fortunately, since the recoiling proton tends to be scattered at an angle to the neutron direction, a large fraction of these events are removed from the sample by the shower deviation angle cutoff of Sec. III. C. 3. In order to fit the ones that remain, however, the opening angle distribution of those events that fit the two-shower n-p recoil hypothesis in the analysis of Sec. III. F. was included for a background curve, when calculating the total cross section.

The coefficients of the linear combination of the above set of curves which best fit the experimental data were found directly by the method described at the beginning of this section. Frequently the first fit to the data produced a set of coefficients in which one or two of the small background terms were slightly negative. For example, a positive $2\pi^0n$ distribution combined with a smaller negative $3\pi^0n$ distribution, often resulted in the best fit. This was not physically meaningful, however, so the fit was repeated with the negative term constrained to be zero, i.e., it was left out of the fit. The parameter $\sqrt{\chi^2/d}$, which indicated the goodness of fit, was imperceptibly changed by the omission.

Since the most significant background resulted from final states containing more than two photons, the shape of the background estimated by the Monte Carlo calculations could be compared with an experimental estimate of this distribution. For this purpose, events were selected from the experimental sample of three-shower events in which the shortest of the three showers was less than three inches long. These short showers were considered to be "almost missing," and opening angle distributions were made from the remaining two showers as if they might well have been a background two-shower event. The background distribution calculated by the Monte Carlo method compared quite favorably with this experimental estimate. In fact, this experimental estimate of the background might have been used directly, except that better statistics were available in the Monte Carlo calculations, so that smoother curves could be used in the fitting. Figure 30 shows the various components of the background at $T_{\pi^-} = 1300$ MeV, normalized for the actual background subtraction from Fig. 29, a typical case.

These calculations of the different background curves were regarded as an enlightened attempt to make a reasonable subtraction of events from the opening angle distribution to get the π^0 and η contributions. They were not designed to derive the $2\pi^0 n$, $3\pi^0 n$, ΛK, or ωn cross sections. The absolute number of background events was comparatively small, so that the relative statistical errors in the background coefficients were fairly large. Further, it is not known exactly what effect the simplifications made in the Monte Carlo calculations would have on the results. Much better knowledge of the cross sections for most of the background processes could be obtained from analysis of the three, four, five, and six-shower events recorded in this experiment rather than analysis of the two-shower residue in the opening angle plots.

To check the sensitivity of the results to the various assumptions made, fits were made 1) with an absolutely flat opening angle background, 2) with a background proportional to the sine of the opening angle, as would be expected for completely uncorrelated pairs of showers, and

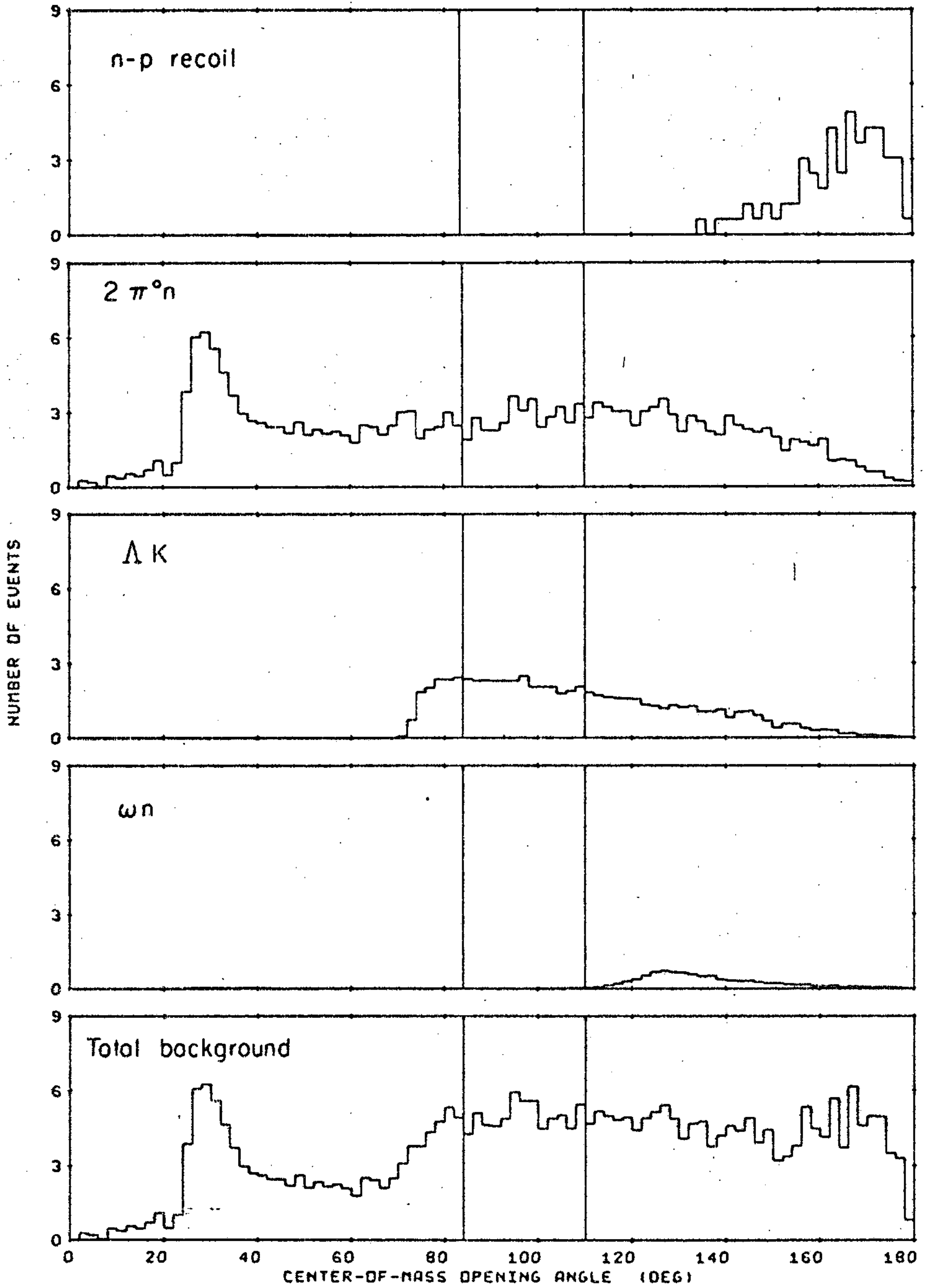

Figure 30. Components of the background subtraction at $T_{\pi^-} = 1300$. Shown in the histograms are the actual number of events used in the subtraction from the opening angle distribution of Fig. 29.

3) with no efficiency corrections to the π^0 and η opening angle curves. In all cases these were significantly poorer fits to the data than the ones using the Monte Carlo estimations, while in cases 1 and 2 the value of the ratio, R, did not vary more than one standard deviation. When using no efficiency correction, the fit was extremely poor.

The only phenomenon not taken into account in the efficiency calculations was the occurrence of the n-p recoil events, described in Sec. III. F. A certain fraction of both the π^0 and the η two-shower events is missing because a proton track imitated a third shower. Hence, after the number of π^0's and η's producing each opening angle distribution was calculated by the least squares fit, each number was corrected, using the number in Table VIII to account for the missing two-shower events. As the opening angle in the meson decay is not correlated with the scattering angle or energy of the neutron, this correction could be properly made after the fitting.

Table X contains the final results of the fitting. The fraction of events in the η opening angle region attributed to background events is shown, along with the total number of η's as obtained from the normalization of the theoretical opening angle curve. At each energy the ratio R is given, along with the goodness of fit parameters. The charge exchange cross section is taken from Ref. 14 a, and thus the quantity, $f_\eta \cdot \sigma(\pi^- p \rightarrow \eta n)$ is calculated and listed in the last column. Given in Fig. 31 is a graph of this partial eta production cross section as a function of beam energy.

Table X. Ratio R and Eta partial cross section

T_{π^-} (MeV)	Fraction of background in η region (%)	Number of eta's in fit	$\sqrt{\chi^2/d}$	R (%)	$f_\pi \cdot \sigma(\pi^- p \to \pi^0 n)$* (mb)	$f_\eta \cdot \sigma(\pi^- p \to \eta n)$ (mb)
592	4	82±11	0.991	7.2±1.0	7.73±0.48	0.56±0.08
655	5	313±20	0.924	19.1±1.4	5.44±0.35	1.04±0.10
704	13	553±30	0.989	19.8±1.2	4.79±0.30	0.95±0.08
875	24	82±18	0.848	6.1±1.4	6.39±0.40	0.39±0.09
975	16	117±21	0.925	12.5±2.0	2.96±0.25	0.37±0.08
1117	14	247±23	1.000	19.5±1.9	2.18±0.20	0.43±0.06
1300	19	373±36	1.158	12.0±1.2	2.12±0.19	0.26±0.03

*See Ref. 14a

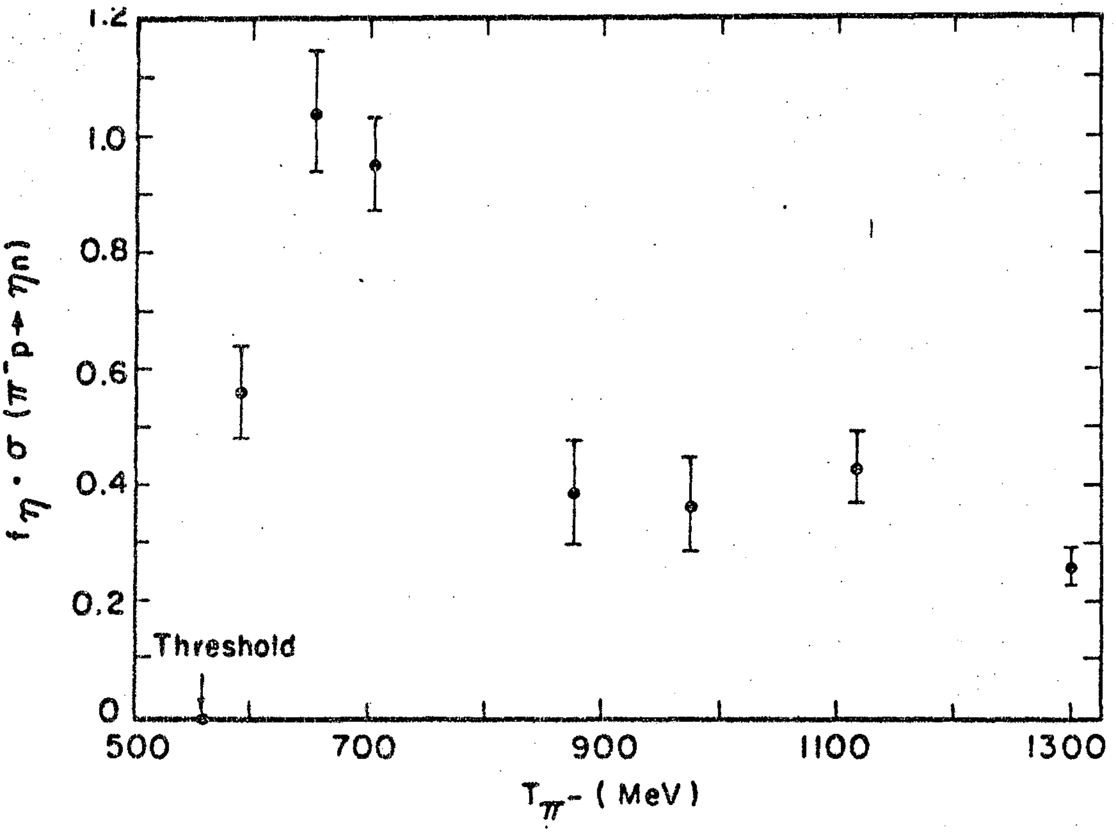

MUB-8543

Figure 31. Partial cross section for η production in $\pi^- p$ scattering. This represents only the fraction of the η's that decay into two γ-rays.

I. Differential Cross Section

The production angular distributions are formed by analysis of two-shower events which have a γ-ray opening angle characteristic of η decay. Previously listed in Table III is the specific opening angle range used at each energy.

It is almost possible to calculate directly the center-of-mass scattering angle of the η for each event. Assuming that the masses of the four primary particles in the interaction, and the kinetic energy of the incoming pion are known, the measurement of the angular position of the two decay photons provides enough information to calculate the direction of travel of the η to within one of two possible directions. The physical meaning of this ambiguity is illustrated in Fig. 32. Given a particular opening angle, Φ, conservation of momentum and energy fixes a unique magnitude of the angle α between γ_1 and the η (see Appendix B., Eq. (B-6). However, if one does not know which experimentally observed photon to call number 1, one cannot tell whether the meson is at position η or η'.

Presumably the way to resolve the ambiguity is to make a determination of the relative energy of the two photons by some measurement on the showers. In the configuration of Fig. 32, γ_1 would be more energetic than γ_2, and hence its shower would contain more energy. An attempt was made to study the characteristics of the showers as a function of the photon energy by using a sample of η events with opening angles within a few degrees of the minimum opening angle, where the two possible solutions converge on the bisector, and the ambiguity disappears. Figure 33 is a scatter plot of the measured length of these showers vs. the calculated laboratory energy of the photons. Showers which ended at an

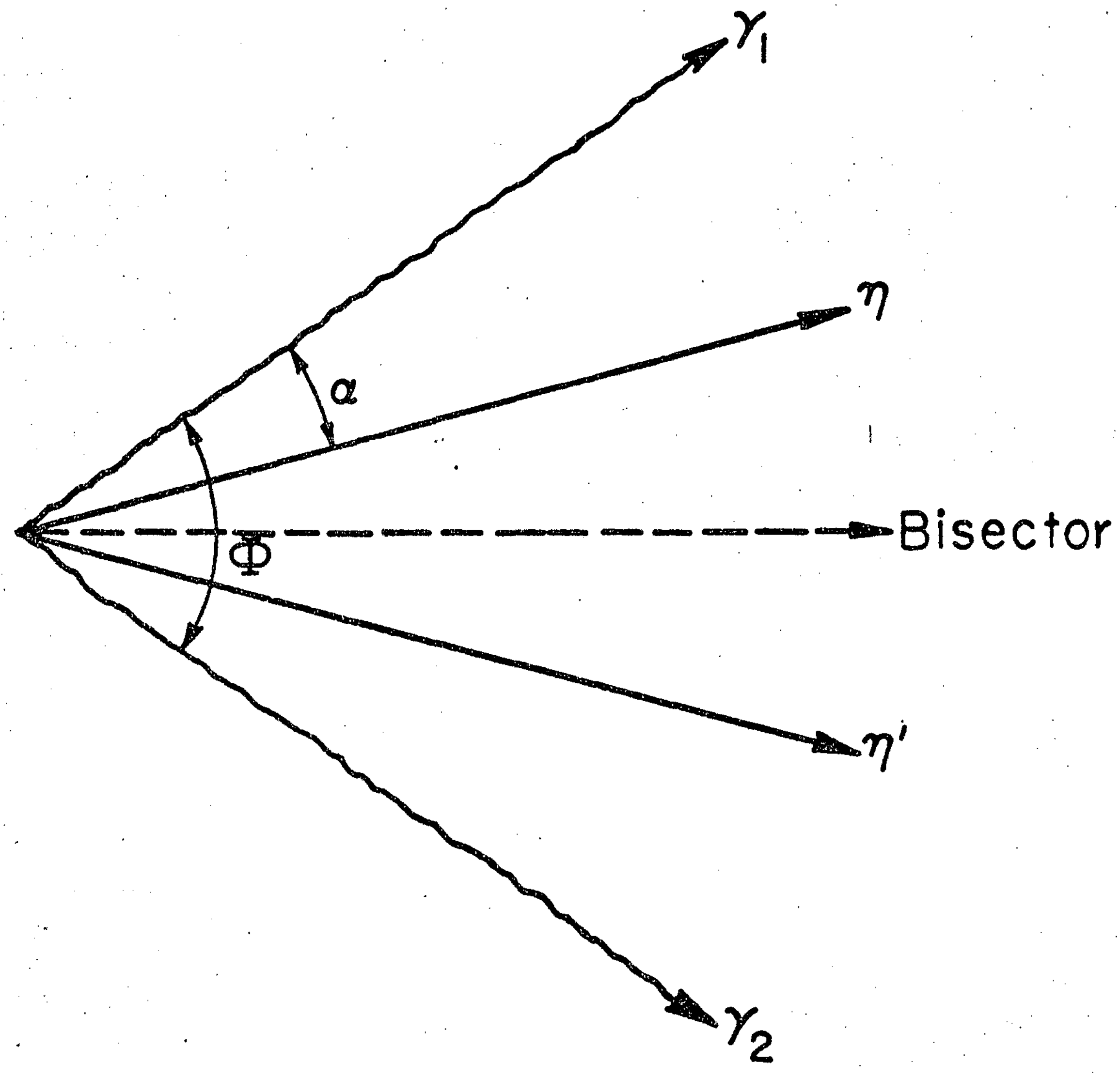

MU-36830

Figure 32. Illustration of kinematical ambiguity. See text for explanation

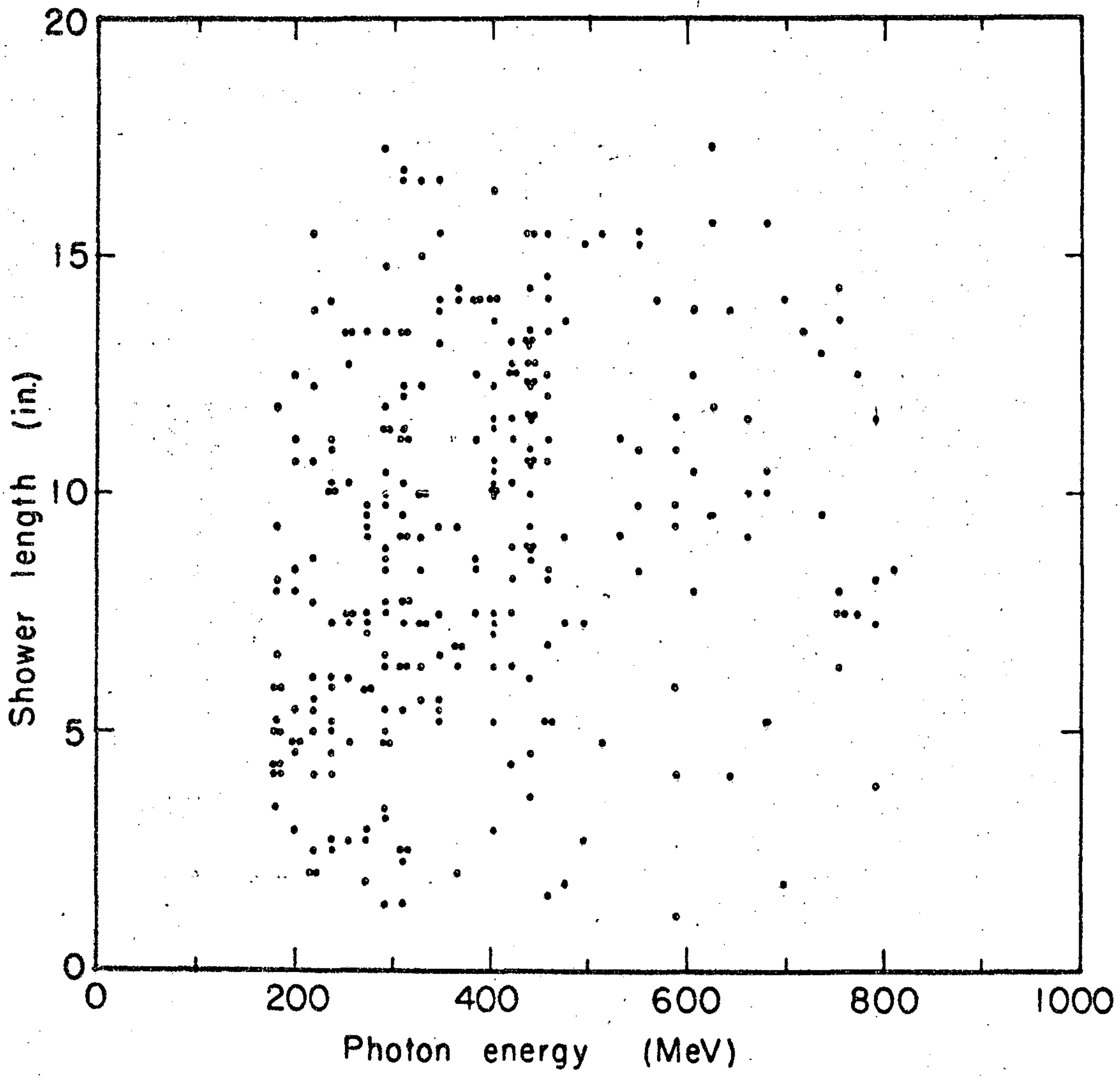

MU-36837

Figure 33. Scatter plot of the length of showers vs. the energy of the initiating photon.

edge of a chamber were eliminated from the sample on the possibility that they had run out of the chamber. Because of the straggling of the showers,[30] ambiguities in measurements of the length, and spark robbing of one track by other adjacent tracks, the scatter plot more nearly resembles a cloud than points clustering about a line. Even though the average shower length at a given energy did increase monotonically with photon energy, obviously it would be rather difficult to predict exactly how much energy is in any given ten-inch shower. Attempts to correlate with energy the number of sparks in the showers, the volume of the showers, and the solid angle of the showering particles also produced similar results, and this whole method of analysis was abandoned.

Instead, a slightly less direct method was used. In Appendix B it is shown that it is possible to derive the η angular distributions from the experimental distribution of the bisector between the two γ-rays. Since it is necessary to have a 4π sr detector to perform a direct conversion, our particular experimental arrangement is ideal for this analysis. To summarize the method, if the distribution of the bisectors has been fit by a sum of Legendre polynomials as

$$\left.\frac{d\sigma}{d\Omega}\right|_{\mathrm{Bis}} = \sum_i A_i P_i(\cos\theta_{\mathrm{Bis}}) \quad , \tag{14}$$

then the true η angular distribution is given by

$$\left.\frac{d\sigma}{d\Omega}\right|_{\eta} = \sum_i (A_i/\xi_i) P_i\,(\cos\theta_\eta). \tag{15}$$

The A_i are the coefficients of the bisector fit, and

$$\xi_i = \int_{\frac{1}{\beta}\cos\frac{\Phi_{max}}{2}}^{1} \frac{(1 - \beta^2)\, x\, P_i(x)dx}{\sqrt{1 - x^2}\left\{1 - \beta^2 x^2\right\}^{3/2}} \qquad (16)$$

where Φ_{max} is the upper limit of the opening angle interval from which the sample was taken, and β is the center-of-mass velocity of the meson. A derivation of these equations is given in Appendix B, along with a table of values of the ξ_i, as calculated by numerical integration for the energies of this experiment.

At each energy the events with opening angles in the η region formed the raw sample. The angular distribution of the bisectors in the c.m. system was made in ten bins of equal size in cos θ_{Bis}, from - 1 to 1. To the target-full and target-empty distributions the aluminum cutoff and the shower deviation angle cutoff were applied, and a full-empty subtraction of the surviving events was made.

Then a correction was made for background events. The same Monte Carlo programs that were used to estimate the backgrounds in the opening angle plots also made bisector distributions of background events with opening angles characteristic of η decay. The primary background is from the $2\pi^0 n$ final state, and the approximate shape of the Monte Carlo bisector distribution for this reaction varied from $(1 - 0.14 \cos\theta)$ to $(1 - 0.57 \cos\theta)$ at the lowest and highest energies, respectively. Other backgrounds were essentially isotropic. To calculate the fraction of the events in the η region attributable to each background final state, the fit to the opening angle curve for the total cross section was employed. This calculation furnished the normalization for the subtraction of the background bisector distributions.

Again, as in the case of the background in the opening angle distribution, the Monte Carlo estimates of the background bisector distributions could be compared with those made from two out of three showers in the sample of three-shower events, when the third shower was very short. At low energies the angular distribution of the bisector of the fake two-shower "events" with η-like opening angles compared very well with the Monte Carlo background calculation. However, at the highest two energies there were significantly fewer bisectors in the backward hemisphere in the selected three-shower sample than the Monte Carlo calculation had predicted. Because the phase space assumptions made in the Monte Carlo calculations become more liable to error as the energy increases, and because there were an adequate number of events in the experimental three-shower sample at the high energies, the experimental estimate of the background shape was used instead of the Monte Carlo at T_{π^-} = 1117 MeV and 1300 MeV.

After the background was subtracted, the number of events in each bin was multiplied by an efficiency factor to correct the shape of the bisector distribution for any distortions introduced by 1) the rejection of good events in the aluminum region, and 2) loss of events due to the inefficiency of the chambers. These correction factors were calculated by the Monte Carlo program described in Sec. III. E. 3. In view of the statistical errors in the data, this correction was almost of negligible effect, since the factors for all the bins in any distribution were the same within ± 2%.

Having made the above corrections, the bisector angular distributions were normalized to the partial cross section at each energy, and the results, together with the errors, are listed in Tables XI through

XVII.

A curve having the equation

$$\left.\frac{d\sigma}{d\Omega}\right|_{Bis} = \sum_{i=0}^{N} A_i P_i(\cos\theta_{Bis}) , \qquad (17)$$

was fitted to the ten data points in each distribution, using the method of least squares.[27] Table XVIII summarizes the results. The correct order of fit was determined using the standard χ^2 test as the main criterion. Another criterion that was used is that if a kth order fit is required at a particular energy, then at all higher energies, a fit of at least kth order should be used. This is based on the assumption that once a given partial wave is present, it should continue to be present at all higher energies as well, even though its contribution may become small. It was necessary to employ this criterion in deciding the order of fit only at 975 MeV, where, according to the χ^2 test, a first order fit would have been best; nevertheless, a second order fit was chosen because that order had been necessary at lower energies.

It may be pointed out that one of the outstanding advantages of fitting the data with Legendre polynomials rather than a simple cosine power series is that the conclusions do not depend so critically on the exact order of fit chosen. Because of the near orthogonality of the summed Legendre polynomials, the values of the low-order coefficients do not change very much as the order of fit is increased or decreased, in great contrast to the behavior of cosine power series coefficients. Thus, although argument is possible on whether or not to include a small high order coefficient, the final choice cannot change an inference based on large variations in the low order terms.

In Figs. 34 through 40 are presented the normalized angular distributions of the bisectors. The data points are the experimental results listed in the tables, and the solid line in each graph is the best χ^2 fit to the bisector data.

Table XI. Center-of-mass angular distribution of bisector, T_{π^-} = 592 MeV.

Cos θ_{Bis}	$\left.\frac{d\sigma}{d\Omega}\right\|_{\text{Bis}}$ (μb/sr)
0.9	58±22
0.7	43±19
0.5	38±20
0.3	62±22
0.1	28±16
-0.1	31±18
-0.3	59±21
-0.5	39±17
-0.7	39±17
-0.9	46±19

Number of events in original sample: 72

Number remaining after full-empty subtraction: 67

Final number after background subtraction: 64

The coefficients of the Legendre polynomial expansion of this curve were divided by the factors of Eq. (16), normalized in such a way that $\xi_0 = 1$; and the dotted line in each graph is a plot of the new expansion, which represents the true η differential cross section.

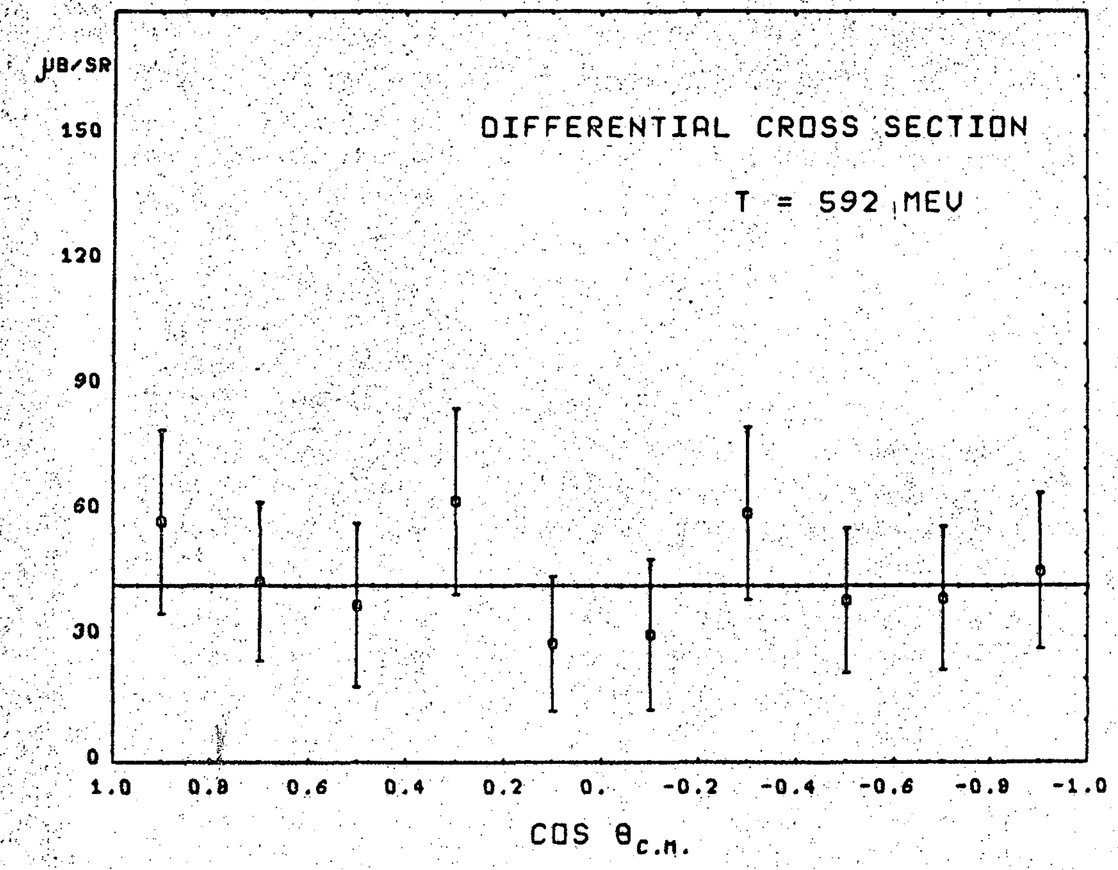

MU-36839

Figure 34. Partial differential cross section of η production at T_{π^-} = 592 MeV. The solid line is the best fit to the bisector distribution data points, and the dotted line is the η differential cross section.

Table XII. Center-of-mass angular distribution of bisector, $T_{\pi^-} = 655$ MeV

Cos θ_{Bis}	$\left.\frac{d\sigma}{d\Omega}\right\|_{Bis}$ (μb/sr)
0.9	134±22
0.7	129±22
0.5	95±20
0.3	42±14
0.1	60±16
-0.1	58±16
-0.3	78±18
-0.5	76±17
-0.7	65±16
-0.9	89±19

Number of events in original sample: 255

Number remaining after full-empty subtraction: 250

Final number after background subtraction: 237

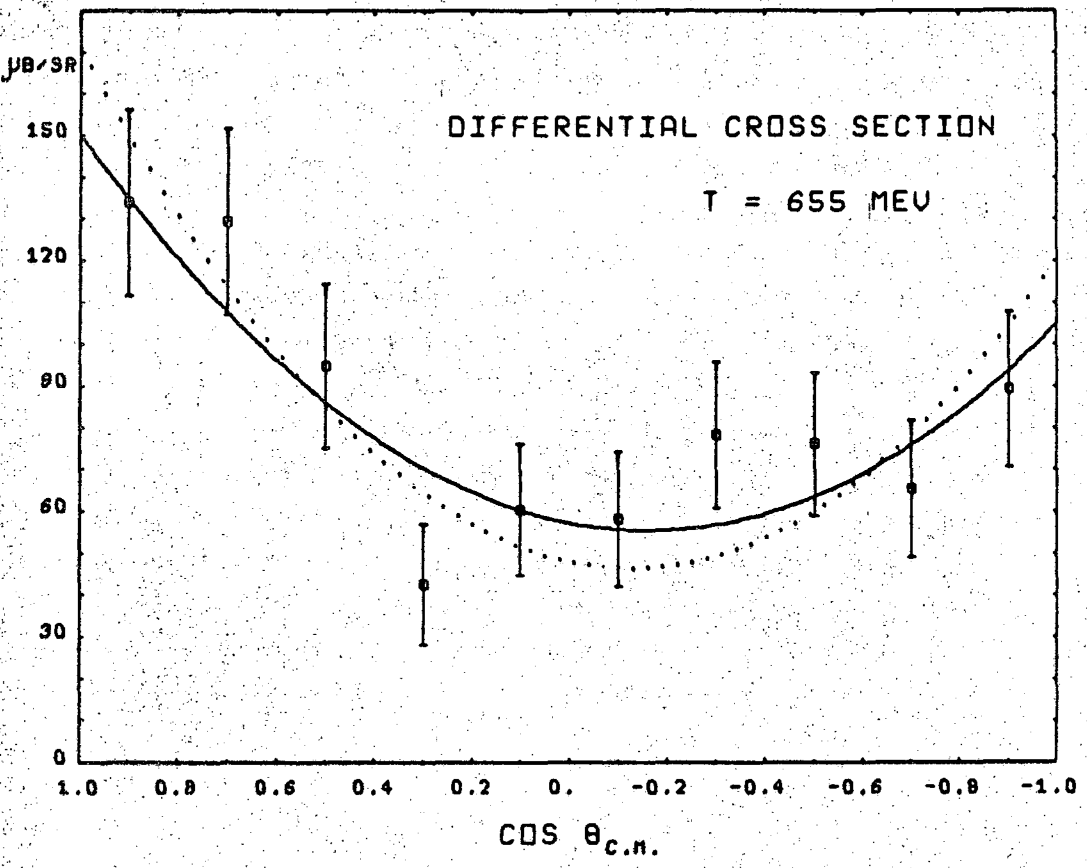

MU-36840

Figure 35. Partial differential cross section of η production at T_{π^-} = 655 MeV. The solid line is the best fit to the bisector distribution data points, and the dotted line is the η differential cross section.

Table XIII. Center-of-mass angular distribution of bisector, T_{π^-} = 704 MeV.

Cos θ_{Bis}	$\left.\frac{d\sigma}{d\Omega}\right\|_{\text{Bis}}$ (μb/sr)
0.9	141±17
0.7	93±15
0.5	90±14
0.3	49±12
0.1	67±12
-0.1	72±13
-0.3	68±13
-0.5	60±13
-0.7	65±13
-0.9	48±12

Number of events in original sample:	499
Number remaining after full-empty subtraction:	486
Final number after background subtraction:	425

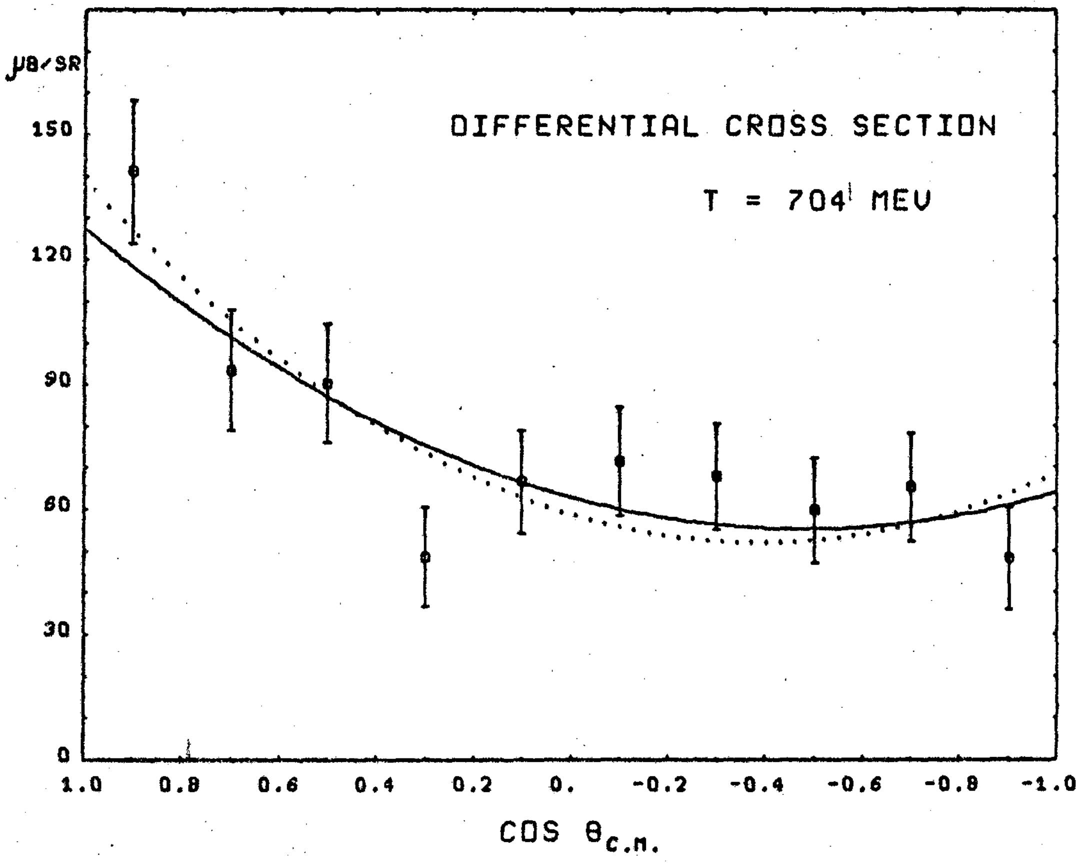

MU-36841

Figure 36. Partial differential cross section of η production at T_{π^-} = 704 MeV. The solid line is the best fit to the bisector distribution data points, and the dotted line is the η differential cross section.

Table XIV. Center-of-mass angular distribution of bisector, $T_{\pi^-} = 875$ MeV.

Cos θ_{Bis}	$\left.\frac{d\sigma}{d\Omega}\right\vert_{Bis}$ (μb/sr)
0.9	78±20
0.7	37±19
0.5	28±17
0.3	35±15
0.1	23±17
-0.1	25±14
-0.3	14±12
-0.5	21±14
-0.7	13±14
-0.9	37±17

Number of events in original sample:	97
Number remaining after full-empty subtraction:	91
Final number after background subtraction:	70

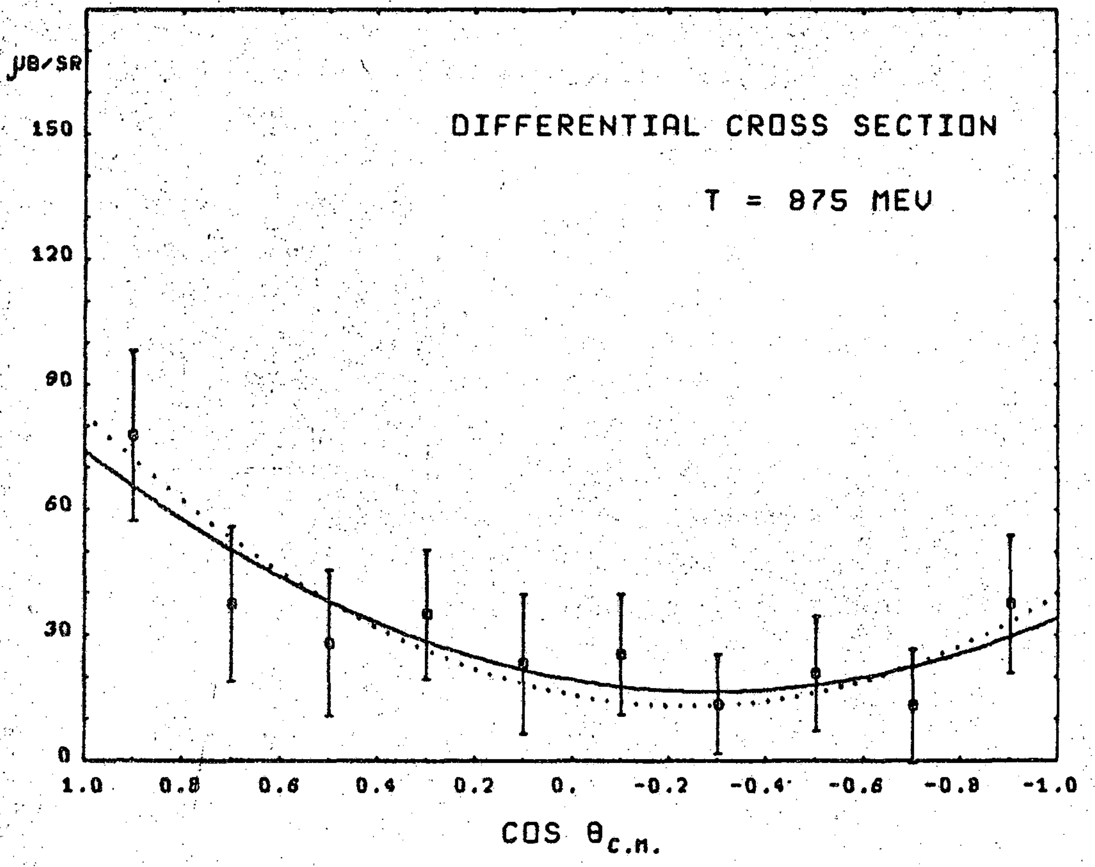

MU-36842

Figure 37. Partial differential cross section of η production at T_{π^-} = 875 MeV. The solid line is the best fit to the bisector distribution data points, and the dotted line is the η differential cross section.

Table XV. Center-of-mass angular distribution of bisector, T_{π^-} = 975 MeV.

Cos θ_{Bis}	$\left.\frac{d\sigma}{d\Omega}\right\|_{Bis}$ (μb/sr)
0.9	45±15
0.7	88±18
0.5	46±17
0.3	24±11
0.1	52±15
-0.1	16±9
-0.3	13±8
-0.5	3±8
-0.7	10±8
-0.9	0±8

Number of events in original sample:	130
Number remaining after full-empty subtraction:	115
Final number after background subtraction:	97

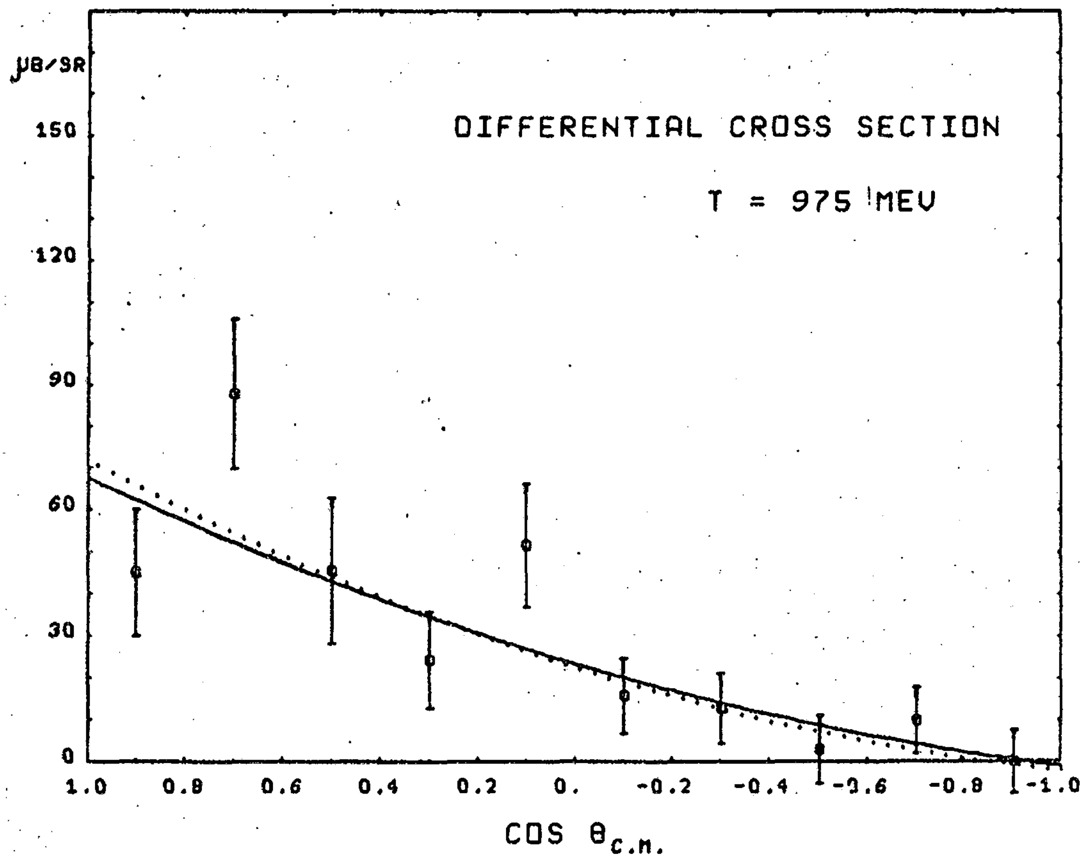

MU-36843

Figure 38. Partial differential cross section of η production at T_{π^-} = 975 MeV. The solid line is the best fit to the bisector distribution data points, and the dotted line is the η differential cross section. The negative section of the dotted curve is statistically consistent with being zero.

Table XVI. Center-of-mass angular distribution of bisector, T_{π^-} = 1117 MeV.

Cos θ_{Bis}	$\left.\frac{d\sigma}{d\Omega}\right\|_{Bis}$ (μb/sr)
0.9	49±10
0.7	49±12
0.5	60±11
0.3	52±11
0.1	43±12
-0.1	34±9
-0.3	19±7
-0.5	15±7
-0.7	7±5
-0.9	12±5

Number of events in original sample:	254
Number remaining after full-empty subtraction:	242
Final number after background subtraction:	209

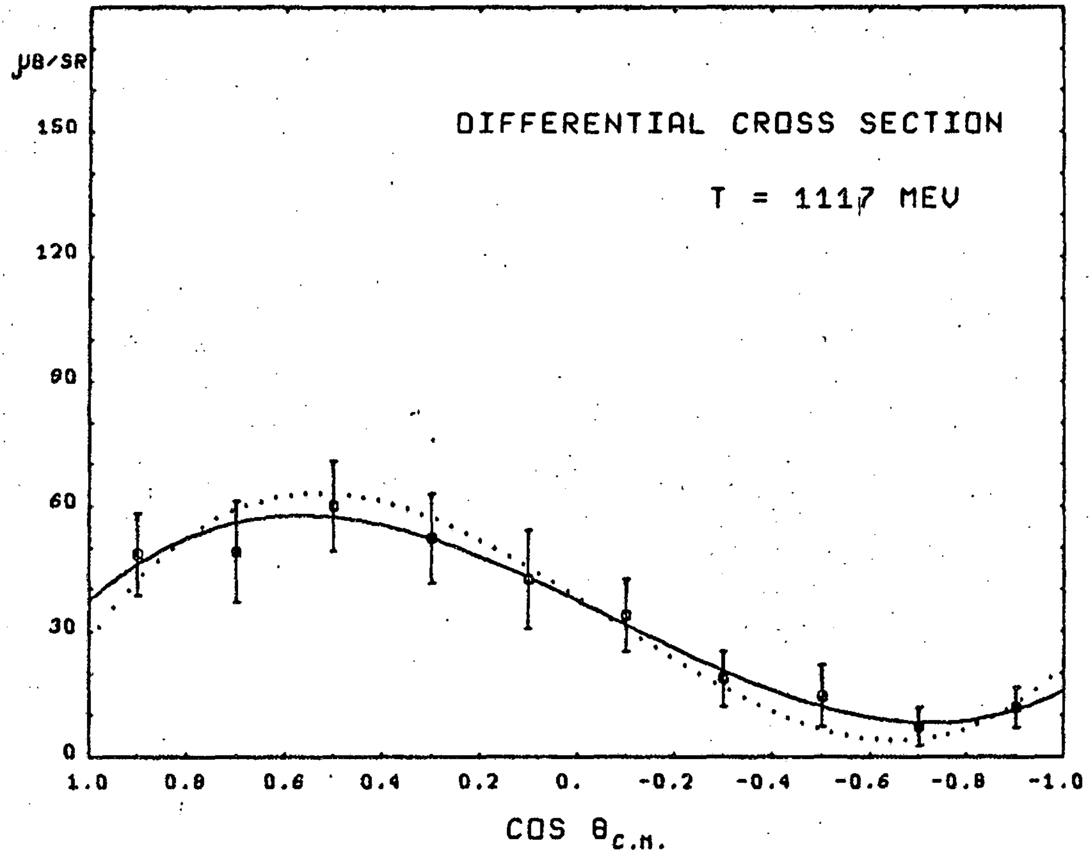

MU-36838

Figure 39. Partial differential cross section of η production at T_{π^-} = 1117 MeV. The solid line is the best fit to the bisector distribution data points, and the dotted line is the η differential cross section.

Table XVII. Center-of-mass angular distribution of bisector, $T_{\pi^-} = 1300$ MeV.

Cos θ_{Bis}	$\left.\frac{d\sigma}{d\Omega}\right\|_{Bis}$ (μb/sr)
0.9	37±7
0.7	48±7
0.5	41±7
0.3	36±6
0.1	21±5
-0.1	5±5
-0.3	3±4
-0.5	3±4
-0.7	4±3
-0.9	6±3

Number of events in original sample:	373
Number remaining after full-empty subtraction:	340
Final number after background subtraction:	276

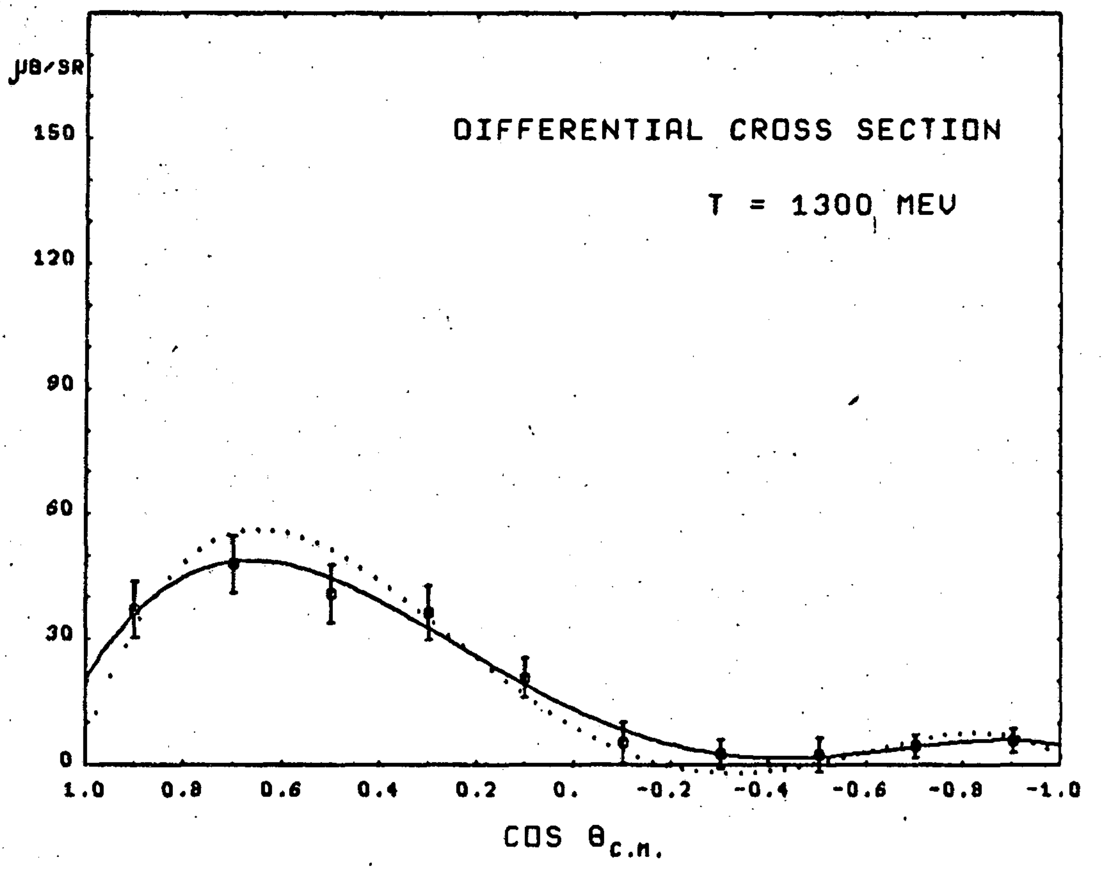

Figure 40. Partial differential cross section of η production at T_{π^-} = 1300 MeV. The solid line is the best fit to the bisector distribution data points, and the dotted line is the η differential cross section. The negative section of the dotted curve is statistically consistent with being zero.

Table XVIII. Summary of Legendre polynomial fits to the bisector distributions.

T_{π^-} (Mev)	Order of fit	$\sqrt{\chi^2/d}$	A_0 (μb/sr)	A_1 (μb/sr)	A_2 (μb/sr)	A_3 (μb/sr)	A_4 (μb/sr)
592	0	0.609	42±4				
655	2	1.029	81±6	22±11	47±14		
704	2	1.218	74±5	32±9	22±12		
875	2	0.590	31±3	20±5	23±7		
975	2	1.204	27±5	34±8	6±9		
1117	3	0.363	34±1	29±2	- 7±2	-18±3	
1300	4	0.487	20±1	27±1	5±2	-18±2	-12±3

Table XIX and Fig. 41 contain the Legendre polynomial expansion coefficients of the η differential cross section.

The errors quoted in this section are only the statistical error in the shape of the curve. The overall normalization error of all the data points and coefficients at each energy, which arises from the uncertainty in the partial cross section, is additional.

Table XIX. Coefficients in Legendre polynomial expansion of η differential cross section, normalized to partial cross section.

T_π (MeV)	A_0 (μb/sr)	A_1 (μb/sr)	A_2 (μb/sr)	A_3 (μb/sr)	A_4 (μb/sr)
592	42±4				
655	81±6	25±12	65±19		
704	74±5	35±10	30±17		
875	31±3	22±6	30±9		
975	27±5	37±9	8±12		
1117	34±1	31±2	-9±3	-29±4	
1300	20±1	28±2	6±2	-26±3	-22±4

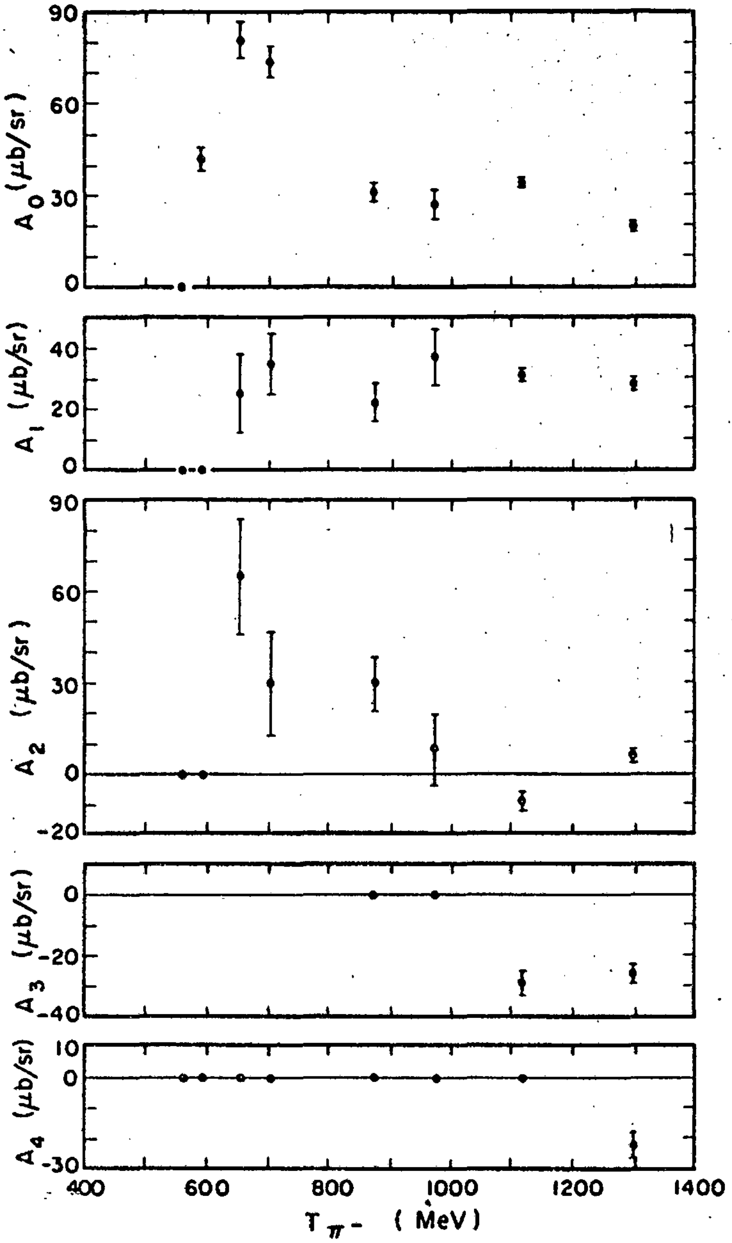

MUB-6544

Figure 41. Legendre polynomial expansion coefficients of the η differential cross section. The errors shown do not include the overall normalization error at each energy.

IV. DISCUSSION OF THE RESULTS

A. Comparison with Other Experiments

1. Total Cross Section

Shown in Fig. 42 are all the η production cross section measurements in the beam energy range from threshold to 1500 MeV known to the author at the present time, where the reaction studied was either $\pi^- p \rightarrow \eta n$ or $\pi^+ n \rightarrow \eta p$. Under the hypothesis of charge independence, the latter reaction is equivalent to the former. Measurements extending up to higher energies show that beyond 1500 MeV, the cross section decreases monotonically to about 10 μb at P_{π^-} = 18 GeV/c.[31-34] The branching ratios used to calculate the total η production cross section from the experimental observations of various final states are[2a]

$$\frac{\Gamma(\eta \rightarrow 2\gamma)}{\Gamma(\eta \rightarrow \text{all decays})} = 35\%, \qquad (17)$$

and

$$\frac{\Gamma(\eta \rightarrow \text{neutrals})}{\Gamma(\eta \rightarrow \text{charged})} = 2.25 \;. \qquad (18)$$

The curve in the figure was sketched by hand, favoring our own data.

The isolated measurement by Chretien et al.,[7] and the series of measurements beginning at 1.4 GeV by Barmin et al.[31] were made by observing the 2γ decay mode in heavy liquid bubble chambers. In view of the relatively low efficiency of the bubble chambers for converting photons and the consequent large correction, it is gratifying that their measurements agree within statistics with ours.

Liquid deuterium bubble chambers were used in the experiments of Meer et al.[35] and Pauli et al.[36] It was assumed that the proton in deuterium was only a spectator to the reaction

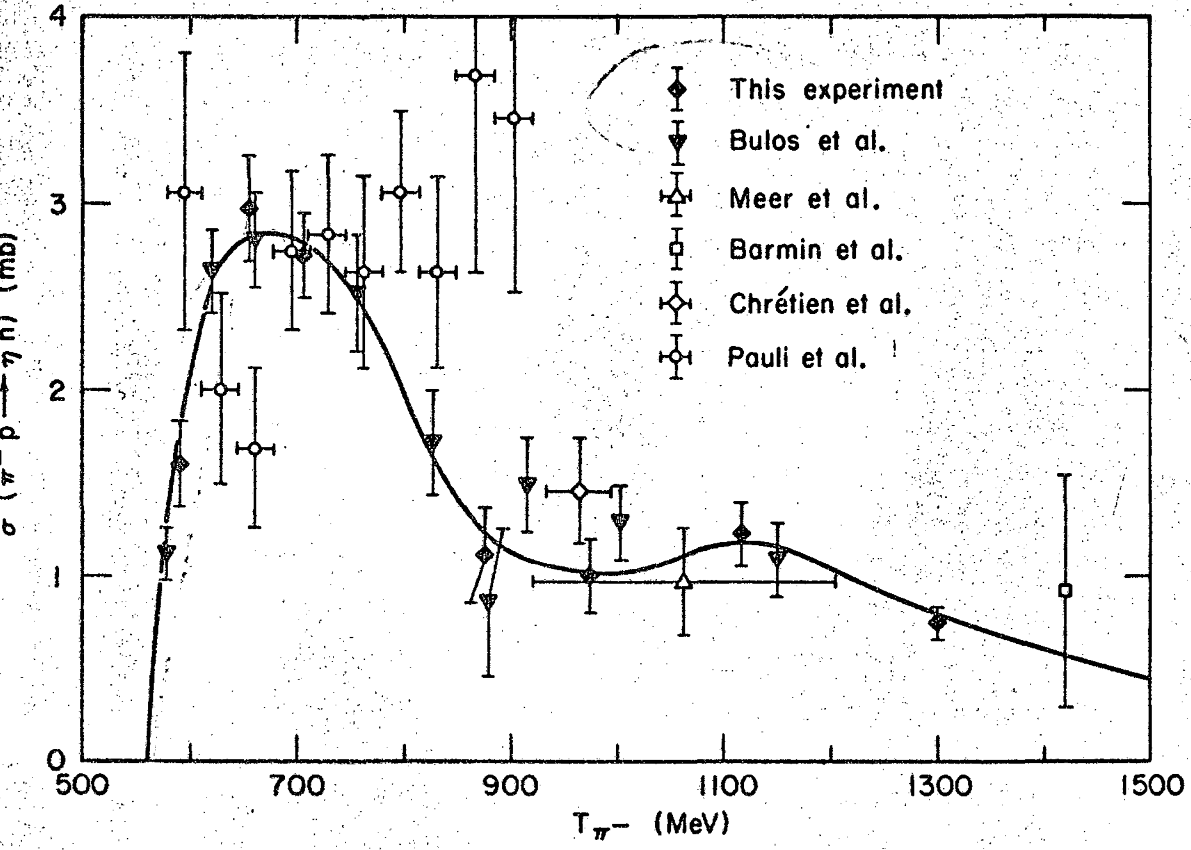

MUB-8590

Figure 42. η production total cross sections as determined by Bulos et al.,[37] Meer et al.,[35] Barmin et al.,[31] Chretien et al.,[7] Pauli et al.,[36] and this experiment.

$$\pi^+ n \rightarrow p + \text{neutrals}; \tag{19}$$

and events where the neutral final state particles had the effective mass of an η meson were utilized to calculate the η production cross section. In each event Pauli et al. subtracted the observed energy of the spectator proton to get the equivalent c.m. energy of the η - p system, and thus were able to find the production cross section as a function of c.m. energy. As Meer et al. did not do this, their result is an integrated cross section over all energies available to the η-p system. Our agreement with Meer et al. is good. In its preliminary form, the cross section of Pauli et al. is of the same order of magnitude as ours and indicates the sharp rise from threshold, but has a rather erratic energy dependence. Because of this behavior, the disagreement around 650 MeV and 900 MeV is not felt to be of any significance.

The experiment of Bulos et al.[37] was very similar to the one reported in this thesis, and was run almost concurrently at the Brookhaven National Laboratory. The only significant difference was that they had only four spark chambers, compared to our six. In their case, the chambers corresponding to the top and bottom of our cube were missing.[38] This forced them to make a correction for their detection geometry, and this correction was much larger for the η distributions than for the π^0 distributions, because the η's have such large opening angles.

Nevertheless, below 800 MeV our production cross sections agree extremely well; and everywhere above 800 MeV the two experiments agree within statistics, although our data alone suggest the existence of a small enhancement at $T_{\pi^-} = 1100$ MeV, while the data of Bulos et al. do not. Further speculation about the enhancement will be given in Sec. IV. B. 5. The point at 875 MeV is one of the most difficult to measure, because the charge exchange cross section is at the so-called 900 MeV resonance, while at the same time the $2\pi^0n$ cross section, which is the major source of background, is at some sort of maximum. Both phenomena tend to make the η peak in the opening angle plots relatively very small (cf. Figure 26). Therefore, any discrepancy there is not too mysterious.

In summary, all experiments show an extremely sharp rise of the production cross section from threshold, to almost 3 mb at $T_{\pi^-} \cong 650$ MeV. Beyond that there is a more gradual decline, with this experiment and the experiment of Bulos et al. yielding the best measurement of the energy dependence up to 1300 MeV.

2. Differential Cross Section

There have been fewer determinations of the η production differential cross section, as the number of η events in most experiments has been too small to make the subdivision into angular intervals meaningful. In another paper from the same experiment referred to above as Meer et al.,[35] Toohig et al.[39] give an angular distribution in η production, based on 30 events decaying by the charged 3π mode. This shows a forward peaking in agreement with our data in the same energy interval. Pauli et al.[36] give one angular distribution made from all 230 η events observed in their experiment, in an energy range which corresponds to a 600 to 900 MeV range of T_{π^-} in our experiment. Except for one data point at $\cos\theta_\eta$(c.m.) = 0, which is too high by 1.5 standard deviations, this distribution is clearly characterized by an important positive $\cos^2$ term, which is in agreement with our angular distributions.

The only other distributions to be considered are those of Bulos et al.,[37] and they present somewhat of a problem. Their results have been published with the best fit as isotropic at all energies from threshold up to $T_{\pi^-} = 1000$ MeV. Then, only a linear cosine term is used to fit the forward peak at their highest two energies. While the differences in the data points might not actually be too great in view of possible statistical fluctuations in the distributions, there is a very significant difference between the conclusion that the differential cross section is completely isotropic throughout such a great energy range, and our conclusion that higher terms are present.

Since their method of analysis seems to be logically correct, it is not entirely obvious to what to attribute the difference between their conclusions and ours. We have investigated the effect on our data of ignoring showers which occur in the top and bottom spark chambers. Even though the bisector distribution of the remaining events has markedly less structure than the original bisector distribution, this fact in itself is of little consquence, since presumably Bulos et al. correct for the geometrical effects in their analysis.

The correction they must make is not a trivial one, however. In particular, the correction to be made to the number of events in each bin depends on what the angular distribution happens to be. Although this is also true in the case of our simple transformation from the bisector distribution to the η differential cross section, the dependence is much more complex where the less favorable detection geometry is used, as will now be shown. Presented in Fig. 43 are the results of a Monte Carlo comparison of the two experiments, which illustrates the difficulties faced by Bulos et al. In two calculations, 6000 events each were generated, according to two different η angular distributions (isotropic and $1 + \cos^2 \theta$), and the bisector distributions that would be observed using four and six chambers were predicted. The geometry assumed in the four-chamber case was exactly the same as that used by Bulos et al.[38] In spite of the great difference between the initial distributions, Bulos et al. would see a forward peak as the dominant feature in both cases, because only in the forward direction is the minimum laboratory opening angle small enough for most of the events to be seen without the top and bottom chambers. Thus, in the rest of the distribution, statistical fluctuations at the points marked "critical bins" in the isotropic case could make the two net results distressingly similar.

Thus it seems apparent that with only four chambers an extremely large number of events would be required to be able to detect with certainty the presence of any non-isotropic terms in the η angular distribution, because the observables are so insensitive to these terms. From the fact that Bulos et al. were not able to divide the complete angular range into more than five bins, we conclude that they did not have a sufficient number of events to see the structure present in the η differential cross section.

A quick glance at the fine-dashed line in Fig. 43 shows that we do not suffer from the same difficulty, and hence we have confidence in our more straight-forward method and in our result.

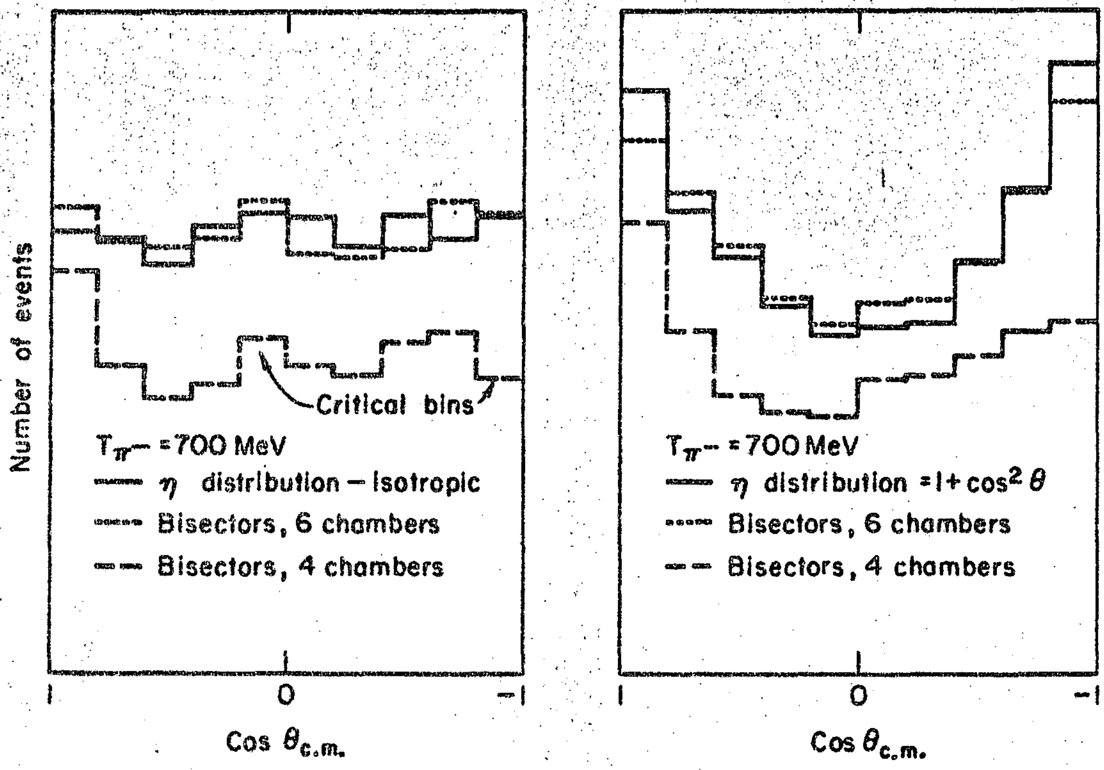

MUB-8587

Figure 43. Monte Carlo comparison of observed bisector distributions with four spark chambers and six spark chambers, for two different η angular distributions.

B. Interpretation of the Data

1. Identification of the Important Angular Momentum States up to 1 GeV.

The extremely fast rise from threshold of the total cross section immediately suggests that the production takes place predominantly with the η and the nucleon in a relative S state. Near threshold the center-of-mass momentum dependence of the cross section is of the form

$$\sigma \propto ka\, V_\ell(ka) \tag{20}$$

where k is the η wave number, a is the interaction radius, and the V_ℓ are the barrier penetration factors for orbital angular momentum ℓ.[40] The first few V_ℓ are

$$V_0(ka) = 1 \tag{21}$$

$$V_1(ka) = \frac{(ka)^2}{1 + (ka)^2} \tag{22}$$

$$V_2(ka) = \frac{(ka)^4}{9 + 3(ka)^2 + (ka)^4} \, . \tag{23}$$

Shown in Fig. 44 is the total cross section plotted as a function of the momentum in the c.m. system, with a straight line which was fit to the first five data points with $\sqrt{\chi^2/d} = 0.87$. Thus, up to P_η(c.m.) = 200 MeV/c, the total cross section is closely proportional to the wave number, as would be expected for an S state.

If one takes our data point at 116 MeV/c, and the point of Bulos et al.[37] at 158 MeV/c and inquires what interaction radius would be required in Eqs. (22) and (23) to make the curve pass through those points, one finds that a = 2.2 fermi for P wave (ℓ = 1) and that it is even larger for D wave (ℓ = 2). Since this interaction radius is larger than the pion Compton wavelength, which is characteristic of the longest range nuclear force, these possibilities may be discarded.

To get more information about the important partial waves, the differential cross section is considered. It can be shown that two complex amplitudes, f and g, are necessary to describe the scattering of a spin 0 particle on a spin 1/2 target. Spin-flip scattering is described by g, while the scattering without spin-flip is given by f.

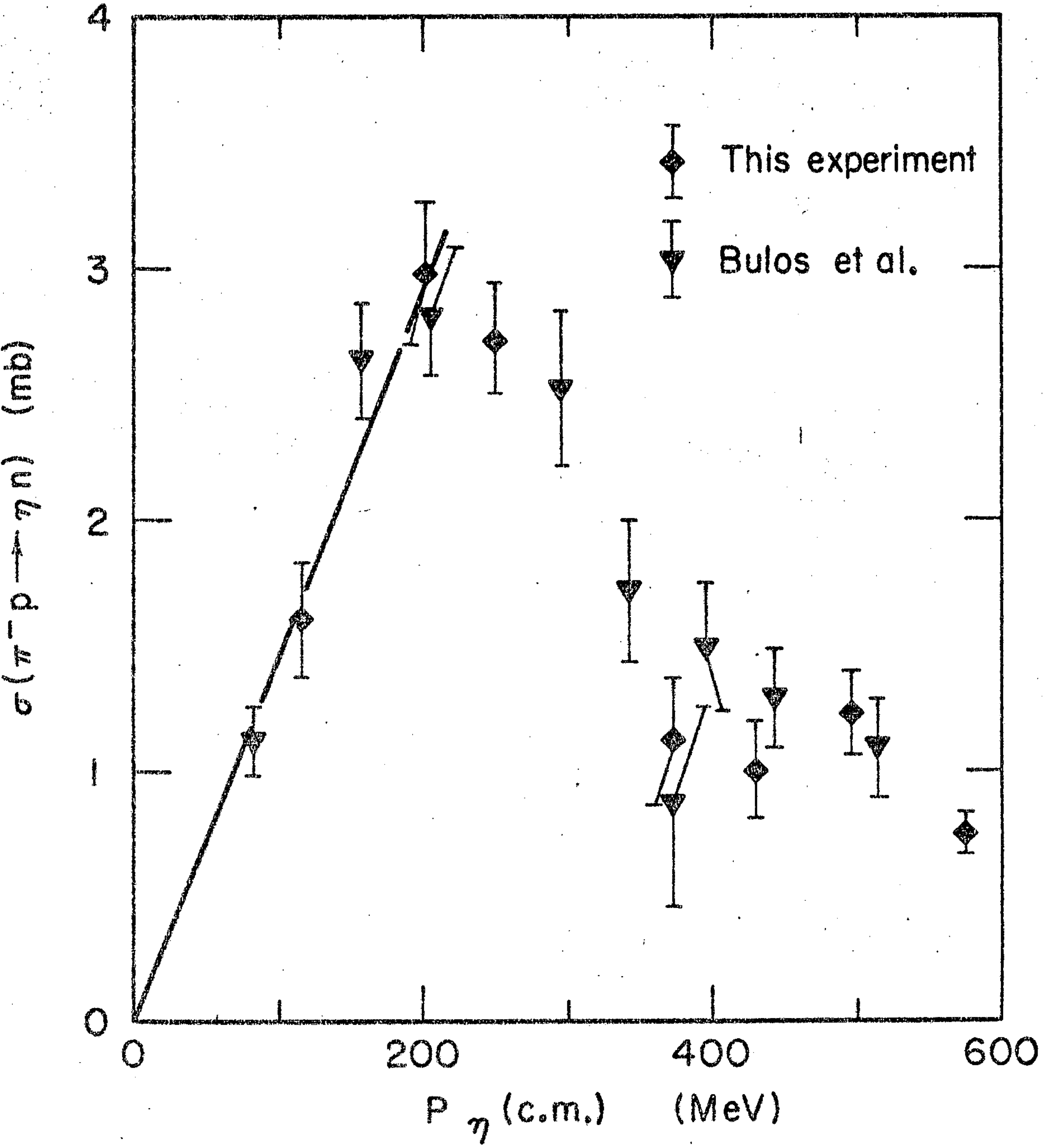

MUB-8589

Figure 44. η production cross section data of Bulos et al.,[37] and this experiment, plotted as a function of the momentum of the η in the c.m. system.

To make a partial wave expansion, one expresses the two amplitudes as a sum over orbital angular momentum states:[41]

$$f = \sum_{\ell} [(\ell + 1)A_{\ell + 1/2} + \ell A_{\ell - 1/2}]P_{\ell}(\cos\theta), \quad (24)$$

and

$$g = \sin\theta \sum_{\ell} [A_{\ell + 1/2} - A_{\ell - 1/2}] \frac{d}{d(\cos\theta)} P_{\ell}(\cos\theta). \quad (25)$$

Here the A's are the partial wave amplitudes, with the subscript indicating the total spin; $P_{\ell}(\cos\theta)$ is the ℓth order Legendre polynomial. In terms of these amplitudes, the differential cross section for scattering on an unpolarized target is

$$\frac{d\sigma}{d\Omega} = |f|^2 + |g|^2 . \quad (26)$$

The absolute square of Eqs. (24) and (25) may be inserted into Eq. (26) to yield the angular dependence of the differential cross section to be expected from any combinations of partial wave amplitudes, or angular momentum states. If states through $\ell = 3$ are included, and the differential cross section is expanded in a Legendre polynomial series, then the result is as given in Eq. (27).[42] The notation used for the partial wave amplitudes in this equation has been changed: the orbital angular momentum is indicated by spectroscopic symbols, with $\ell = 0, 1, 2, 3$ indicated by S, P, D, F, respectively, and the subscript is twice the total angular momentum or spin. Also, the complex multiplication is only implied: i.e., S_1P_1 is taken to mean Re $S_1^*P_1$.

Armed with this expression, we could proceed to examine the coefficients in the Legendre polynomial expansion of the experimentally observed η differential cross section, and try to guess which amplitudes best explain the data. However, the number of amplitudes which need to be considered can be reduced by making use of results from phase-shift analyses of the elastic π-nucleon scattering data, as will now be explained.

$$
\begin{aligned}
\frac{d\sigma}{d\Omega} = {} & P_0(\cos\theta)\left[S_1^2 + P_1^2 + 2P_3^2 + 2D_3^2 + 3D_5^2 + 3F_5^2 + 4F_7^2\right] \\
& + P_1(\cos\theta)\left[2P_1S_1 + 4P_3S_1 + 4D_3P_1 + 0.8\,D_3P_3 + 7.2\,D_5P_3\right. \\
& \qquad \left. + 7.2\,F_5D_3 + 0.5\,F_5D_5 + 10.3\,F_7D_5\right] \\
& + P_2(\cos\theta)\left[4\,P_3P_1 + 2P_3^2 + 4\,D_3S_1 + 2\,D_3^2 + 6\,D_5S_1 + 1.7\,D_5D_3\right. \\
& \qquad + 3.4\,D_5^2 + 6\,F_5P_1 + 1.7\,F_5P_3 + 3.4\,F_5^2 + 10.3\,F_7P_3 \\
& \qquad \left. + 1.1\,F_7F_5 + 4.8\,F_7^2\right] \\
& + P_3(\cos\theta)\left[7.2\,D_3P_3 + 6\,D_5P_1 + 4.8\,D_5P_3 + 6\,F_5S_1 + 4.8\,F_5D_3\right. \\
& \qquad \left. + 3.2\,F_5D_5 + 8\,F_7S_1 + 2.7\,F_7D_3 + 8\,F_7D_5\right] \\
& + P_4(\cos\theta)\left[10.3\,D_5D_3 + 2.5\,D_5^2 + 10.3\,F_5P_3 + 2.5\,F_5^2\right. \\
& \qquad \left. + 8\,F_7P_1 + 5.7\,F_7P_3 + 5.1\,F_7F_5 + 4.2\,F_7^2\right] \\
& + P_5(\cos\theta)\left[14.3\,F_5D_5 + 13.3\,F_7D_3 + 5.7\,F_7D_5\right] \\
& + P_6(\cos\theta)\left[18.2\,F_7F_5 + 3.0\,F_7^2\right] .
\end{aligned}
\tag{27}
$$

For purely elastic π-N scattering, it follows from unitarity of the S matrix that partial wave amplitudes of Eqs. (24) and (25) may be written

$$A_{\ell \pm 1/2} = \frac{e^{2i\,\Delta_{\ell\pm1/2}} - 1}{2\,i\,k} \tag{28}$$

where $\Delta_{\ell\pm1/2}$, a real number, is the phase shift in that partial wave, and k is the wave number of the pion in the π-nucleon c.m. system. If there are any inelastic final states which compete with the elastic scattering, their effect on the elastic scattering amplitude is to add a positive imaginary part to the phase shift. Then the amplitude is customarily written

$$A_{\ell \pm 1/2} = \frac{b_{\ell\pm1/2}\, e^{2i\delta_{\ell\pm1/2}} - 1}{2ik} \tag{29}$$

where

$$\delta_{\ell\pm1/2} = \mathrm{Re}\,\Delta_{\ell\pm1/2} \tag{30}$$

and

$$b_{\ell\pm1/2} = e^{-2\,\mathrm{Im}\,\Delta_{\ell\pm\,1/2}} . \tag{31}$$

The quantity, $b_{\ell\pm1/2}$, is called the absorption paramter and is 1 if the scattering in that wave is completely elastic, and goes to 0 in the limit of maximum absorption. With this expression for the partial wave amplitudes inserted into Eqs. (24) and (25), one can integrate Eq. (26) for the differential cross section over all solid angle and find the contribution to the elastic scattering total cross section from each partial wave. This turns out to be

$$\sigma_{el}(\ell, J) = \frac{\pi}{2k^2}\,(2J + 1)\left|1 - b_{\ell\pm1/2}\, e^{2i\delta_{\ell\pm1/2}}\right|^2 . \tag{32}$$

The total cross section, elastic plus inelastic, can be found using the optical theorem, which is valid for each individual partial wave,

$$\sigma_T(\ell,J) = \frac{4\pi}{k}\,\mathrm{Im}\,f(0)$$
$$= \frac{\pi}{k^2}(2J+1)(1 - b_{\ell\pm 1/2}\cos 2\delta_{\ell\pm 1/2})\,. \tag{33}$$

Hence, we can subtract Eq. (32) from Eq. (33) to get the inelastic cross section in each partial wave:

$$\sigma_{\mathrm{inel}}(\ell,J) = \frac{\pi}{2k^2}(2J+1)(1 - b_{\ell\pm 1/2}{}^2). \tag{34}$$

It follows that in the analysis of an inelastic channel, one's attention may be confined to those partial waves which phase shift analyses of the elastic data have shown to have an absorption parameter less than unity.

All available information on elastic π-nucleon scattering has been analyzed by several workers to find the values of the phase shifts and absorption parameters as a function of energy.[12] While their results are not in complete agreement, it is generally accepted that around 600 MeV S_{11}, P_{11}, and D_{13} waves (notation: $\ell_{2I,2J}$) have large absorptive parts. (Since an η-N state necessarily has isotopic spin 1/2, only the amplitudes for π-N scattering in that I-spin state need be considered.)

We see that precisely these waves suffice to explain our observed angular distribution in η production below 1 GeV. As already deduced from the shape of the total cross section, production appears to take place exclusively in a relative S state immediately above threshold. The isotropic angular distributions support this conclusion.

Beginning at 655 MeV, we suggest that the linear cosine coefficient is due to either a P_1S_1 interference or a D_3P_1 interference, or both; and that the coefficient of the second order Legendre polynomial is mainly due at first to the D_3S_1 interference and the D_3^2 term. By 800 MeV, the S_1 wave becomes less important, although the D_3 wave still prevails up to about 1 GeV. These conclusions are to be compared especially with the phase shift analysis of Bareyre et al.[12a]

Even though this analysis of Bareyre et al. shows that at the I = 1/2 900 MeV resonance, F and D waves are also highly absorptive, the lack of any enhancement in the total cross section plus the absence of high order terms in the angular distribution for η production at this energy show that this resonance does not decay with an observable rate into the η-N state. In view of the large numerical coefficients multiplying these amplitudes (cf. 14.3 F_5D_5 in the $P_5(\cos\theta)$ coefficient of Eq. (27)) the angular distribution provides especially strong negative evidence here. It has been pointed out that this fact suggests that the $N_{1/2}^*(1688)$ should be assigned to an SU(3) octet, which could be the Regge recurrence of the baryon octet, rather than a $\underset{\sim}{27}$ multiplet.[43,44]

2. Quantitative Comparison with Phase-Shift Analyses Up to 1 GeV.

It is of interest to see if η production alone can completely account for the observed absorption in any of the π-N partial waves near the η threshold. One aim of this investigation is an attempt to clarify the role played by the $N_{1/2}^*(1512)$ in η production, and vice-versa.

The procedure to be followed is merely to calculate the inelastic cross section in the various angular momentum states, using Eq. (34) with $b_{\ell\pm1/2}$ as given by the several phase-shift analyses. Before the result can be compared directly with our data, an isotopic spin projection factor of 2/3 must be included, because the π^-p initial state is in an isotopic spin 1/2 state only 2/3 of the time.

Shown in Fig. 45 are the absorption cross sections in the S_{11} π-N state, calculated, as explained above, from the absorption parameters of several different phase shift analyses. Also in the same graph are plotted the η production cross section data from this experiment and from Bulos et al.[37] Although the phase-shift predictions are not in complete agreement, this graph strongly suggests that the observed S_{11} absorption is due almost completely to η production. The fact that the data points do not fall off as rapidly as do the S_{11} absorption cross sections above 700 MeV may be attributed to the contribution from the P_1 and D_3 states, which become important there.

The inelastic cross section in the D_{13} π-N state also reaches a maximum in the vicinity of the η production peak, but because of the (2J + 1) factor of Eq. (34), this cross section is about twice as big as the η production cross section. Even though some D_3-wave is present in the η-N system, we must conclude that the main inelastic decay mode of the $N_{1/2}^*(1512)$ is not into an η-N state, since the η production seems to be predominantly in the S state, as indicated above. This is consistent with the small amount of phase space available for $N_{1/2}^*(1512)$ decay into η-N.

If the absorption in the S_{11} state is indeed to be attributed to η production, an evaluation of one aspect of the various approaches to phase shift analyses may be made here as an aside. In the phase shift searches, two general schemes have been used. The first involves

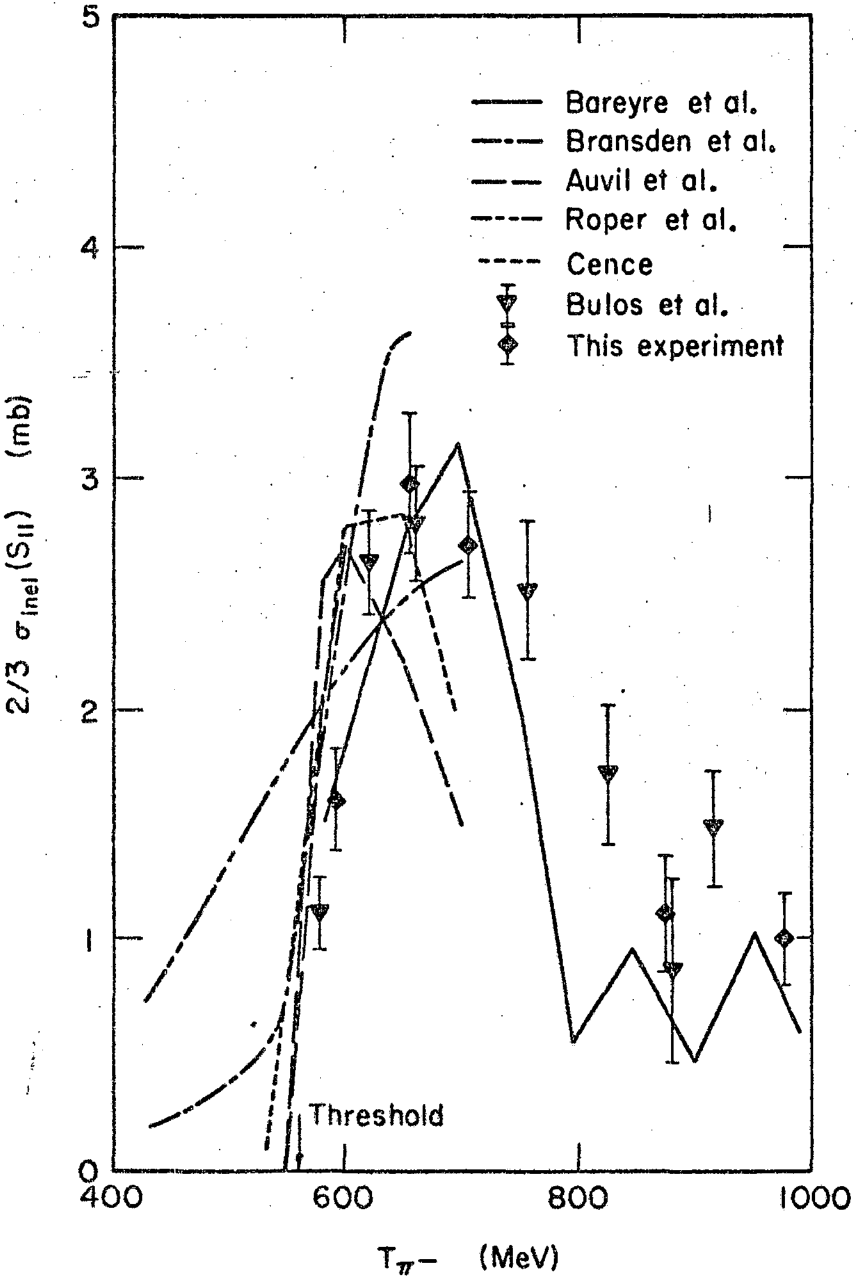

MUB-8588

Figure 45. Inelastic cross section in the S_{11} state calculated from the absorption parameters published by Bareyre et al.,[12a] Bransden et al.,[12b] Auvil et al.,[12c] Roper et al.,[12d] and Cence.[12e] To be compared with them are the η production cross section data measured by Bulos et al.,[37] and this experiment.

expanding the phase shifts and absorption parameters as a power series, or some other function of the c.m. momentum, and then evaluating the parameters of the expansion by fitting to all data at all energies at once. This procedure, used by Roper[12d] and by Bransden et al.[12b] enforces a smooth energy variation of the phase shifts and absorption parameters. The second scheme is to search for the best phases at each energy, separately, with no functional connection between the solutions. The criticism to be made is that it is very difficult to choose a parametrization for the first approach which will allow for the possible sharp changes in the absorption at new inelastic thresholds. Roper's results,[12d] for example, do not show the effect of the η threshold on the S_{11} absorption as clearly as those of Auvil,[12c] Bareyre,[12a] or Cence.[12e] Since there is always the danger inherent in the energy-dependent approach that the parametrization might bias the results, the second approach is to be preferred.

3. Discussion of the S-wave η-N State and its Effect on the π-N System

A natural question to be asked is whether or not the peak in the η production cross section just above threshold is the manifestation of a resonance in the η-N state. This would be difficult to understand, because of the absence of angular momentum in the S state to provide a centrifugal barrier. As an alternative to the resonance hypothesis, S. F. Tuan has shown, using a two-channel K-matrix formalism, that this phenomenon may be understood in terms of bound or virtual states of the η-nucleon system, corresponding to well-defined S-matrix poles.[45] From the point of view of S-matrix theory, this could also be called a "particle," to be placed on a Regge trajectory, and included in higher symmetry schemes, as are resonances.

Frazer and Hendry,[46] in an extension of the work of Ball and Frazer,[47] have shown that such an S-matrix pole associated with the opening of an inelastic S-wave channel can produce sizable effects on the cross section in the elastic cross section--a peak for the bound state case and a cusp in the virtual state case.

The phase shift analysis of Auvil et al.[12c] indicates the presence of a cusp in the S_{11} phase shift at the η threshold. Bareyre et al.[12a] show a cusp in the same phase shift, slightly above the η threshold. Dobson[48] has shown that the S_{11} phase shift of Cence[12e] is consistent with a cusp due to a virtual η-N state. In contrast with these, Uchiyama-Campbell[49] has analyzed the data, and finds no pole in the vicinity of the inelastic threshold. Hendry and Moorhouse[50] find an η-N S-wave resonance just above the threshold, which, as mentioned before, is not easily understood because there is no centrifugal barrier.

It was stated in the Introduction that a similar rapid rise in η production near threshold had been noticed in the reaction $K^- p \rightarrow \eta\Lambda$.[10] Berley et al.[51] have raised the question whether this might be an indication of an S-wave bound state of the $\eta\Lambda$ system. The similarity between production of the η-N final state and the η-Λ final state has led Gyuk and Tuan[52] to postulate the existence of an octet of virtual η-baryon states associated with the thresholds of η production in association with all members of the baryon octet. According to them, this would fall naturally into a place in SU(6) symmetry, where in the $\underline{70}^-$ representation, an octet of $J^P = 1/2^-$ baryon states is called for.

It is hoped that the data from this experiment will contribute toward a clarification of the η-N interaction near the η threshold.

4. Speculations about 1100 MeV

Our measurement of the total η production cross section suggests that there might be a small bump at $T_{\pi^-} = 1100$ MeV. The data point there is approximately two standard deviations from lying on a straight line between the adjacent measurements. Although this by itself might not be considered significant, it happens that at this same energy, the Legendre series coefficient A_2 temporarily dips slightly negative, and the negative coefficient A_3 becomes important for the first time. It is intriguing to assume that something real is happening there and to attempt to figure out what partial wave is responsible for the observed behavior.

Since all of the elements in the general Legendre expansion of the differential cross section as given in Eq. (27) are connected by plus signs, the negative terms must come from interference between two different amplitudes directed oppositely when plotted in the complex plane. We do not think that the D_5 or F_5 amplitudes are responsible, because they should have been important in the region of the 900 MeV resonance, if they were to have played any part at all. Also, barring a conspiracy among the amplitudes, there would be a $P_4(\cos\theta)$ and a $P_5(\cos\theta)$ variation in the differential cross section. Higher waves are also ruled out because they would have contributed more structure to the differential cross section.

A more likely candidate is the P_3 wave. The phase-shift analysis of Bareyre et al.[12a] showsthat the P_3 amplitude is beginning to be definitely absorptive at 1000 MeV--the upper limit of their analysis--after somewhat unsteady behavior at lower energies. Interference with the tail of the D_3 amplitude could provide a negative A_3 term, while interference with the still absorptive P_1 amplitude, partially cancelled by P_3^2, could drive A_2 slightly negative.

It will be interesting to see if this bump remains after the other half of the data, presently being measured by the High Energy Group at the University of Hawaii, is added to the present sample. If it does, the situation at 1100 MeV will deserve a more quantitative study.

ACKNOWLEDGEMENTS

I would like to express my sincere appreciation to Professors A. C. Helmholz and Burton J. Moyer who have directed my research with personal concern. I am indebted to all the members of the Moyer-Helmholz Group for their support during the past three years.

In particular, I owe much to Dr. Robert W. Kenney, Dr. Vincent Z. Peterson, Dr. Robert J. Cence, and Dr. Richard D. Eandi for their hard work during the experimental run and for many profitable discussions. Dr. John A. Poirier designed the beam.

Sincere thanks go to my co-worker, Dr. Charles B. Chiu, for the major part he has played in the whole project.

Competent and enthusiastic work was done by the Scanning and Measuring Group under the direction of Mr. Charles A. Welsh and Mr. C. Jon Kiiskinen.

Without the excellent cooperation of the Bevatron crew and the Computer Center, this work could not have been done.

I am very grateful for the cheerful and conscientious work performed by Miss Miriam L. Machlis, who typed the final draft of this thesis.

Last, but not least, I am deeply indebted to my wife, Jean, who typed the first draft of my thesis and suggested numerous stylistic improvements. She has maintained a lively interest in this project, not because she understands or even likes physics, but because it was my work.

This work was done under the auspices of the U. S. Atomic Energy Commission.

APPENDICES

A. Normalization of Full-Empty Subtraction

In this Appendix the normalization factor of the target-empty distributions, used in making a full-empty subtraction, is derived.

Given a sample of data taken with the target full, and another sample taken with the target empty, it is to be shown first that the target-empty distribution should be multiplied by a factor such that the total number of events in the distribution would result from the same number of incoming pions as that producing the target-full distribution. Then the two distributions may be subtracted to remove from the target-full distribution the effect of interactions which did not take place in the hydrogen.

Let us define three regions of interaction: a) Region A contains all material where interactions might take place before the liquid hydrogen. This would be primarily the last monitor counter and the entrance window to the vacuum dome of the target. b) Region H consists only of the liquid hydrogen. c) Region B is the remaining material between the hydrogen and the detectors; that is, the exit window and downstream part of the vacuum dome, and the anticounter.

In each region there is a given probability that an incoming pion will interact and produce a neutral event. For example, the probability of interaction in the hydrogen is approximately

$$p_H = \sigma \rho \frac{N_a}{A} \ell , \qquad \text{(A-1)}$$

where σ is the neutrals cross section per nucleon, ρ is the density of liquid hydrogen, N_a is Avagadro's number, A is the atomic number of molecular hydrogen, and ℓ is the path length traveled by the pions through the hydrogen. This probability is of the order of 0.1%. Similarly, smaller probabilities exist for production of neutral events in regions A and B. Also for each region a fraction f_A, f_B, or f_H must be defined. These are the fractions of the neutral events produced in each region that qualify for inclusion in the distribution under consideration. This may be the fraction of all events that are two-shower events, or that have a two-shower opening angle in a given region, etc.

Now, with hydrogen in the target, let us suppose that N pions in the beam enter the apparatus. The number of suitable events produced in region A is

$$p_A f_A N \ . \tag{A-2}$$

This number of pions is also removed from the beam, as is a similar number, $p_A'N$, which is removed by any other interaction in region A. Thus the number of pions entering region H is $N - p_A f_A N - p_A'N$, and the number of suitable events produced in the second region is

$$p_H f_H N(1 - p_A f_A - p_A') \ . \tag{A-3}$$

Again, that number of pions, together with the $p_H'N(1 - p_A f_A - p_A')$ removed by other interactions in region H, are not available in region B. The exact expressions soon become unwieldy, but it is clear that the number entering region B may be represented as

$$N(1 - O(p) + O(p^2)) \ . \tag{A-4}$$

In this notation, $O(p)$ is a sum of all the terms which are linear in some interaction probability, and $O(p^2)$ contains only terms with p^2. So finally, the number of events produced in region B is

$$p_B f_B N(1 - O(p) + O(p^2)) \ . \tag{A-5}$$

The simplifying approximation to be made is that the probabilities p_A, p_H, and p_B are all small enough that powers higher than the first may be safely ignored. This is an extremely good approximation. It must be assumed that p_A', p_H', and p_B' are also this small. Neglecting these small quadratic and cubic terms, then, we get

$p_A f_A N$ background events from region A, (A-6)

$p_H f_H N$ events from the hydrogen, and (A-7)

$p_B f_B N$ background events from region B. (A-8)

Now we may take data again, sending in N' pions, with no hydrogen in the target. This is equivalent to setting $p_H = 0$. In the same approximations, the result of this experiment must be

$p_A f_A N'$ background events from region A, and (A-9)

$p_B f_B N'$ background events from region B. (A-10)

It is therefore a trivial result that if $N' = N$, one gets the same number and distribution of background events from the target-empty data that are present in the target-full data, so that with this normalization, a full-empty subtraction of all distributions removes from the final result the effect of any interactions in substances other than the liquid hydrogen.

Ordinarily counter data on the number of incoming pions and the number of neutral events would be taken simultaneously with the pictures, so that the number of pions per picture could be calculated. In our case, the spark gaps and chambers produced so much electrical noise that the counter data taken while the chambers were on was not considered reliable. Consequently, the chambers were turned off periodically, and the counters were run alone to measure the neutral cross section.

Now that the proper normalization has been derived, we must see how to actually calculate the normalization factor for any given sample of data from a specific number of frames of film. To begin with, a number of symbols need to be defined. In all definitions with an asterisk, another definition, with a superscript I on all symbols, is to be understood, to stand for the analogous property of events produced by interacting beams.

Let us take a large sample of pictures, and let

* B = the number of frames with a good single incoming beam in sample. (A-11)

These divide into

* $B = B_n + B_c$, (A-12)

where

* B_n = the number of these frames with a neutral event, (A-13)

and

* B_c = the number of these frames with a charged particle in the final state. (A-14)

All of the distributions are made from the set $\{B\}$, so the problem is to calculate

* N = the number of incoming pions associated with B frames. (A-15)

If

R_{el} = the neutrals/monitors ratio as measured by the counters, (A-16)

one might think that $N = B/R_{el}$ is the answer, but it is not because the neutrals/monitors ratio includes the charged particles in an unequal distribution between B and B^I. If

$N_{tot} = N + N^I$ (A-17)

what is true is that

$$N_{tot} = \frac{B + B^{I}}{R_{el}} \quad . \qquad \text{(A-18)}$$

We must define the probability of interaction;

* p_n = probability that a good single beam particle produces a neutral event, (A-19)

* p_c = probability that a good single beam particle produces a charged final state, (A-20)

that is,

* $B_n = Np_n$, (A-21)

and

* $B_c = Np_c$. (A-22)

We make the assumption that $p_n \cong p_n^{I}$; in other words, the probability that an interacting beam particle produces a neutral event is the same as for a good beam particle; it is only the charged particle production which is different.

Then we may put

$$N_{tot} = N + N^{I} = N + \frac{B_n^{I}}{p_n^{I}} = N + \frac{B_n^{I}}{p_n} = N(1 - \frac{B_n^{I}}{B_n}) \qquad \text{(A-23)}$$

Hence

$$N = N_{tot} \frac{B_n}{B_n + B_n^{I}} = \frac{B_n}{R_{el}} \left[\frac{B + B^{I}}{B_n + B_n^{I}} \right] \qquad \text{(A-24)}$$

is the number of incoming pions associated with the sample of B frames.

Only one further modification remains. The number of monitors for the given sample is calculated using the totals for the various beam types as determined by the scanners. Then a subset of the good frames is measured and put on a computer data tape for analysis. This might be all of the j-shower events, where j = 1, 2, or 3. Not all of the j-shower events in the original sample get to the data tape, however, because of mismeasurements, or computer malfunctions. Consequently, when the number of monitors for the events on the tape are calculated, the number as derived above must be multiplied by the fraction, F_j, of the original subset that survive.

Hence, the complete procedure is to 1) form some distribution, g_F, from target-full events, and calculate the number of incoming pions, $N_F F_{jF}$, associated with the sample of full events, and 2) get the corresponding target-empty quantities, g_{MT} and $N_{MT} F_{jMT}$. The final distribution, corrected for interactions which did not occur in the liquid hydrogen, is then

$$g = g_F - \frac{N_F \, F_{jF}}{N_{MT} F_{jMT}} \quad \cdot \quad g_{MT} \; . \tag{A-25}$$

B. Kinematics of Two-Gamma Decay

In this Appendix the equations will be derived which are used in the analysis of η angular distributions, relating the distribution of the bisector of the γ-rays to the distribution of the η. The treatment will be of a neutral meson, X, with a 2γ decay mode, which could be either a π^0 or an η, for instance, and the units will be such that $c = 1$.

The analysis is only useful in an inertial frame where every meson, X, in the sample of data has the same velocity, because the velocity, β, is the main parameter of the equations. Such a frame is the so-called center-of-mass system of a two-body final state like the one of this experiment, where the vector sum of the two momenta is zero, and the velocity of X is fixed by momentum and energy conservation independently of the scattering angle. From now on, then, if there is no special comment, all quantities are evaluated in the center-of-mass frame.

One of the principal ingredients of the derivation is the distribution in the magnitude of the angle, δ, between the direction of the X-meson and the bisector of the decay gamma rays. This angle is shown in Fig. B-1a, along with Φ, the opening angle. The distribution in δ may be expressed

$$\frac{dn}{d\delta} = \frac{dn}{d\Phi} \cdot \frac{d\Phi}{d\delta} \quad , \tag{B-1}$$

where $dn/d\Phi$ is the opening angle distribution, repeated here for completeness,

$$\frac{dn}{d\Phi} = \frac{1}{2\gamma^2\beta} \quad \frac{\cos \Phi/2}{\sin^2\Phi/2 \sqrt{\beta^2 - \cos^2 \Phi/2}} . \tag{B-2}$$

This is slightly rewritten from the form derived in Ref. 8, and has been

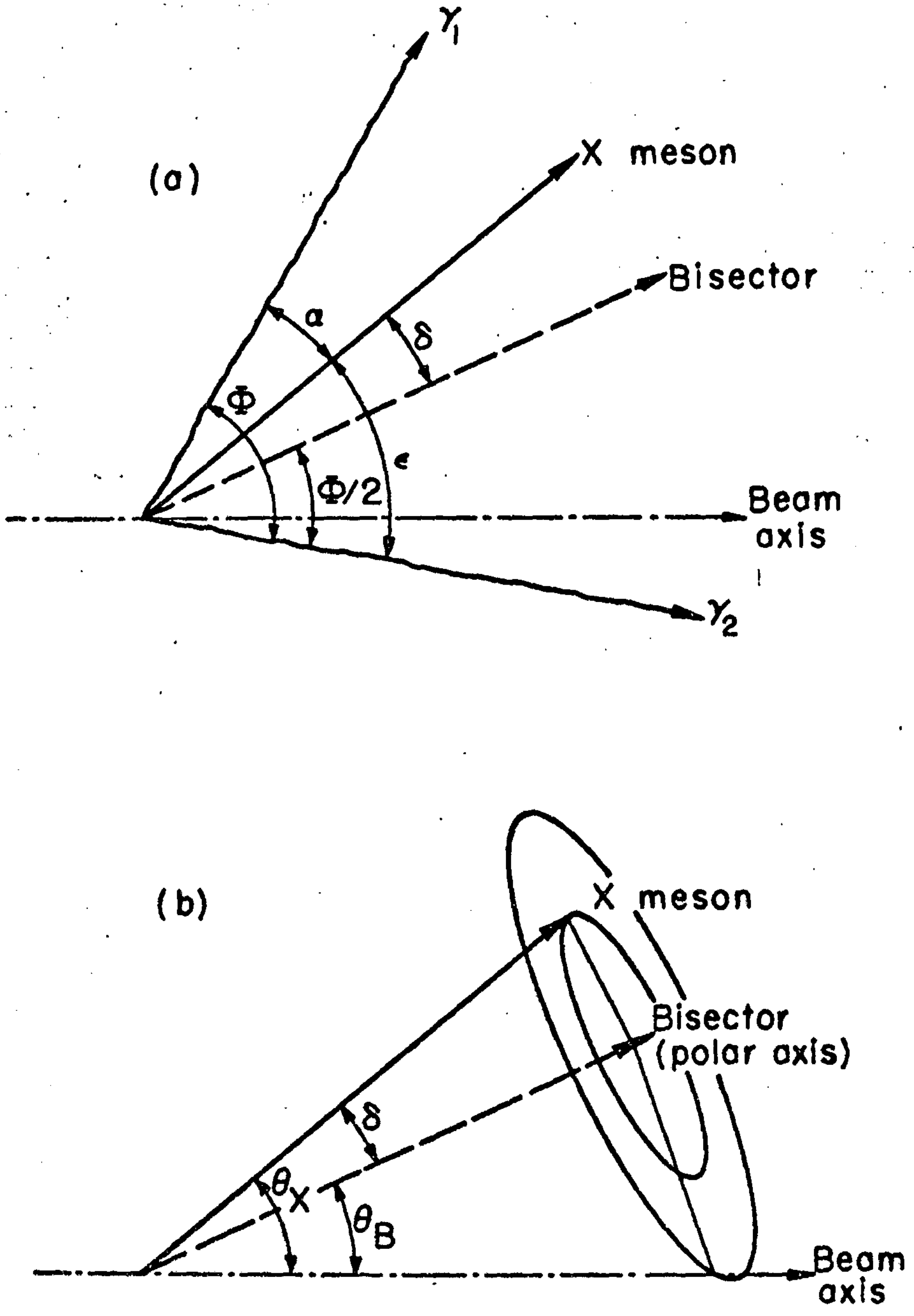

MU-36829

Figure B-1. a. Angles used in kinematical equations.

b. Coordinate system for integration of bisector equation.

multiplied by a factor of two so that

$$\int_{\Phi_{\min}}^{180^{\circ}} \frac{dn}{d\Phi}\, d\Phi = 1 \ . \qquad \text{(B-3)}$$

In Eq. (B-2), β is the velocity of meson X, and $\gamma = \dfrac{1}{\sqrt{1 - \beta^2}}$.

To get the second factor in Eq. (B-1), we must derive the relationship between Φ and δ. This can be easily done by applying energy and momentum conservation to the decay illustrated in Fig. B-1a. We write

$$\frac{p_x}{E_x} = \frac{p_1 \cos \alpha + p_2 \cos \epsilon}{E_1 + E_2} \ , \qquad \text{(B-4)}$$

where the numerator expresses longitudinal momentum conservation and the denominator is conservation of energy in this decay. Since in our units

$E_1 = p_1$, $E_2 = p_2$, and $p_x/E_x = \beta$, this can be written

$$\beta = \frac{\cos \alpha + \dfrac{p_2}{p_1} \cos \epsilon}{1 + \dfrac{p_2}{p_1}} \ . \qquad \text{(B-5)}$$

Eliminating the ratio, p_2/p_1, by using the condition of transverse momentum balance, we get finally

$$\beta = \frac{\cos \Phi/2}{\cos(\Phi/2 - \alpha)} \ , \qquad \text{(B-6)}$$

or

$$\beta \cos \delta = \cos \Phi/2 \ . \qquad \text{(B-7)}$$

Differentiation of this yields

$$\frac{d\Phi}{d\delta} = \frac{2\beta \sin \delta}{\sin \Phi/2} \ . \tag{B-8}$$

Hence, multiplying Eqs. (B-2) and (B-8), and using Eq. (B-7) to eliminate Φ, we get the desired result, namely:

$$\frac{dn}{d\delta} = \frac{\cos \delta}{\gamma^2 \left\{1 - \beta^2 \cos^2 \delta\right\}^{3/2}} \ . \tag{B-9}$$

We can choose to differentiate with respect to cos δ, instead, giving

$$\frac{dn}{d(\cos \delta)} = -\frac{1}{\sin \delta} \frac{dn}{d\delta} = \frac{-(1 - \beta^2) \cos \delta}{\sqrt{1 - \cos^2 \delta} \left\{1 - \beta^2 \cos^2 \delta\right\}^{3/2}} \ . \tag{B-10}$$

Now we can write down and evaluate an expression for the angular distribution of the bisectors, given the distribution in angle of the meson, X. First we put

$$\frac{d\sigma}{d\Omega_B} = \int \frac{d^2\sigma}{d\Omega_B d\Omega_X} \quad d\Omega_X \ . \tag{B-11}$$

Here

$$\frac{d^2\sigma}{d\Omega_B d\Omega_X} \ d\Omega_B d\Omega_X$$

is the joint probability that an event occurs in which the X meson is in the element of solid angle, $d\Omega_X$, and at the same time the bisector of the decay γ-rays is in the solid angle, $d\Omega_B$. The directions of the bisector and the incoming beam axis (from which the scattering angles are measured) are held fixed, and the integration is over all possible directions of scattering of X.

The joint probability may be expressed

$$\frac{d^2\sigma}{d\Omega_X d\Omega_B} = \frac{d\sigma}{d\Omega_X} \cdot \frac{dn}{d\Omega_B} , \tag{B-12}$$

where

$$\frac{d\sigma}{d\Omega_X} \, d\Omega_X = \sum_{\ell} C_\ell P_\ell(\cos\theta_X) d\Omega_X \tag{B-13}$$

is the probability of an X scattering into the solid angle $d\Omega_X$; and $\frac{dn}{d\Omega_B} d\Omega_B$ is the probability of finding the bisector in $d\Omega_B$ at the same time, a function of the angular separation δ of the X and the bisector. Thus, Eq. (B-11) is expanded to the following

$$\frac{d\sigma}{d\Omega_B} = \sum_{\ell} C_\ell \int P_\ell(\cos\theta_X) \frac{dn}{d\Omega_B}(\cos\delta) \, d\Omega_X \tag{B-14}$$

The choice of coordinate system in which to integrate cannot affect the result, so we choose the somewhat peculiar spherical coordinate system which has its polar axis in the direction of the bisector under consideration. This system is illustrated in Fig. B-1b. In this coordinate system, the factor, $\frac{dn}{d\Omega_B} d\Omega_X$, of Eq. (B-14), is the probability of having the X meson at a solid angle, $d\Omega_X$, with respect to the bisector, which is given by the distribution of Eq. (B-10); i.e.,

$$\frac{dn}{d\Omega_B} \, d\Omega_X = \frac{1}{2\pi} \frac{dn}{d(\cos\delta)} \, d(\cos\delta) d\phi_X , \tag{B-15}$$

where ϕ_X is the azimuthal angle of the X meson with respect to the bisector polar axis. Thus we have so far

$$\frac{d\sigma}{d\Omega_B} = \frac{1}{2\pi} \sum_{\ell} C_\ell \iint P_\ell(\cos\theta_X) \frac{dn}{d(\cos\delta)} \, d(\cos\delta) d\phi_X . \tag{B-16}$$

We can carry out the integration if we recall the addition theorem for spherical harmonics which can be written in the following way for the vectors of Fig. B-1b.[53]

$$P_\ell(\cos\theta_x) = P_\ell(\cos\delta)P_\ell(\cos\theta_B) + 2\sum_{m=1}^{\ell} \frac{(\ell-m)!}{(\ell+m)!} P_\ell^{\,m}(\cos\delta)P_\ell^{\,m}(\cos\theta_B) \times \cos\left[m(\phi_x - \phi_B)\right]. \qquad \text{(B-17)}$$

Again, ϕ_B is the azimuthal angle of the beam direction with respect to the bisector.

If we substitute this into Eq. (B-16), the integration over $d\phi_x$ can be done. All of the terms in the expansion of $P_\ell(\cos\theta_x)$, except the first, are multiplied by $\cos\left[m(\phi_x - \phi_B)\right]$, and these drop out when integrating over $d\phi_x$ from 0 to 2π. The first term is multiplied by 2π, which cancels out the $(2\pi)^{-1}$ of Eq. (B-16). After this step the bisector distribution is

$$\frac{d\sigma}{d\Omega_B} = \sum_\ell \left[C_\ell \int P_\ell(\cos\delta)\ \frac{dn}{d(\cos\delta)}\ d(\cos\delta)\right] P_\ell(\cos\theta_B)\ . \qquad \text{(B-18)}$$

Or, writing $u = \cos\delta$, and putting in distribution (B-10),

$$\frac{d\sigma}{d\Omega_B} = \sum_\ell \left[C_\ell \int_{\frac{1}{\beta}\cos\frac{\Phi_{max}}{2}}^{1} \frac{(1-\beta^2)u\,P_\ell(u)du}{\sqrt{1-u^2}\,\{1-\beta^2u^2\}^{3/2}}\right] P_\ell(\cos\theta_B)\ . \qquad \text{(B-19)}$$

The limits of integration correspond to taking δ from 0 to some maximum angle, less than 90 deg, which is related by Eq. (B-7) to the maximum opening angle one wishes to consider when selecting events.

This is the result we seek. The integrals

$$\xi_\ell = \int_{\frac{1}{\beta}\cos\frac{\Phi_{max}}{2}}^{1} \frac{(1 - \beta^2)\ u\ P_\ell(u)du}{\sqrt{1 - u^2}\left\{1 - \beta^2u^2\right\}^{3/2}} \quad , \tag{B-20}$$

have been done numerically, resulting in Table B-I. These express the relationship between the coefficients of a Legendre polynomial expansion of the differential cross section for X production, namely C_ℓ, and the expansion coefficients of the γ-ray bisector distribution, given by $\xi_\ell C_\ell$.

Table B-I. Values of ξ_ℓ at the energies of this experiment

T_{π^-} (MeV)	592	655	704	875	975	1117	1300
β_η(c.m.)	0.2067	0.3468	0.4155	0.5622	0.6161	0.6724	0.7241
Φ_{max}(deg)	168	154	148	134	126	120	110
ξ_0	0.8675	0.7811	0.7785	0.7811	0.7587	0.7721	0.7451
ξ_1	0.7439	0.6998	0.7016	0.7137	0.7024	0.7178	0.7026
ξ_2	0.5489	0.5618	0.5701	0.5963	0.6021	0.6207	0.6249
ξ_3	0.3557	0.4059	0.4193	0.4571	0.4791	0.5005	0.5250
ξ_4	0.2190	0.2698	0.2845	0.3261	0.3568	0.3794	0.4182
ξ_5	0.1528	0.1769	0.1888	0.2252	0.2545	0.2762	0.3192
ξ_6	0.1372	0.1309	0.1380	0.1632	0.1832	0.2019	0.2388
ξ_7	0.1466	0.1201	0.1227	0.1363	0.1439	0.1585	0.1822

FOOTNOTES AND REFERENCES

* This work was supported by the U. S. Atomic Energy Commission.

1. C. M. G. Lattes, H. Muirhead, G. P. S. Occhialini, and C. F. Powell, Nature 159, 694 (1947).

2. a. A. H. Rosenfeld, A. Barbaro-Galtieri, W. H. Barkas, P. L. Bastien, J. Kirz, and M. Roos, Rev. Mod. Phys. 36, 977 (1964).

   b. G. F. Chew, M. Gell-Mann, and A. H. Rosenfeld, Scientific American 210, 74 (February, 1964).

3. G. Puppi, Ann. Rev. Nuc. Sci. 13, 287 (1963).

4. A. Pevsner, R. Kraemer, M. Nussbaum, C. Richardson, P. Schlein, R. Strand, T. Toohig, M. Block, A. Engler, R. Gessaroli, and C. Meltzer, Phys. Rev. Letters 7, 421 (1961).

5. C. Mencuccini, R. Querzoli, G. Salvini, and V. G. Silvestrini, Proceedings of the International Conference on High Energy Physics at CERN, p. 33 (1962).

6. L. Behr, P. Mittner, and P. Musset, Phys. Letters 4, 22 (1963).

7. Brandeis-Brown-Harvard-M.I.T-Padua collaboration, Phys. Rev. Letters 9, 127 (1962).

8. B. Rossi, High Energy Particles (Prentice-Hall, Inc. Englewood Cliffs, N. J. 1952) p. 200.

9. Some of the ideas in the next two paragraphs are taken from: V. Silvestrini, Photoproduction and Neutral Decay Modes of the η Particle, in Strong, Electromagnetic, and Weak Interactions, edited by A. Zichichi (W. A. Benjamin, Inc. New York, 1964) p. 217.

10. a. P. L. Bastien, J. P. Berge, O. I. Dahl, M. Ferro-Luzzi, D. H. Miller, J. J. Murray, A. H. Rosenfeld, and B. Watson,

Phys. Rev. Letters 8, 114 (1962).

b. P. L. Bastien, J. P. Berge, Phys. Rev. Letters 10, 188 (1963). (See also Ref. 51.)

11. The curve in Fig. 3 was calculated using the formula

$$\sigma_{1/2} = 3/2\ \sigma^- - 1/2\ \sigma^+$$

with the experimental data of T. J. Devlin, J. Solomon, and G. Bertsch, Phys. Rev. Letters 14, 1031 (1965).

12. a. P. Bareyre, C. Brickman, A. V. Stirling and G. Villet, Phys. Letters 18, 342 (1965).

b. B. H. Bransden, P. J. O'Donnell and R. G. Moorhouse, Phys. Letters 11, 339 (1964).

c. P. Auvil, C. Lovelace, A. Donnachie, and A. T. Lea, Phys. Letters 12, 76 (1964).

d. L. D. Roper, Phys. Rev. Letters 12, 340 (1964).
L. D. Roper, R. M. Wright, and B. T. Feld, Phys. Rev. 138B, B190 (1965).

e. R. J. Cence, π-N Phase-Shifts from 300 to 700 MeV, University of Hawaii Report HEPG-3-65 (unpublished).

13. Elementary remarks on resonance theory are contained in M. B. Watson, M. Ferro-Luzzi, and R. D. Tripp, Phys. Rev. 131, 2248 (1963).

14. a. C. B. Chiu, Pion-Proton Charge Exchange, 500 to 1300 MeV (Ph. D. Thesis) UCRL-16209 (unpublished).

b. Papers on this experiment have been presented at several American Physical Society Meetings by some combination of the following authors: R. J. Cence, C. B. Chiu, R. D. Eandi, R. W. Kenney, B. J. Moyer, J. A. Poirier, V. Z. Peterson,

W. B. Richards, N. K. Sehgal, and V. J. Stenger, Abstracts H8, H9, Bull. Amer. Phys. Soc. *8*, 603 (Dec. 1963); Abstracts CB9, CB10, *ibid*, *9*,409 (April 1964); Abstracts CE6, CE11, *ibid*, *10*, 701 (Sept. 1965).

W. B. Richards and C. B. Chiu, Total and Differential Cross Sections for the Reaction $\pi^- p \rightarrow \eta n$, UCRL-16140 (unpublished).

c. See also, V. Z. Peterson et al., *Proceedings of the International Conference on Physics of High Energy Particles,* Dubna, U. S. S. R., 1964 (to be published).

B. J. Moyer, *ibid*.

15. B. Rossi, *op. cit.*, Ch. 5.

16. John A. Poirier (Dept. of Physics University of Notre Dame, Notre Dame, Indiana (private communication) April, 1963.

17. V. O. Brady (Lawrence Radiation Laboratory, Berkeley) (private communication) 1961.

18. D.C. Giancoli, Differential Distribution of π^+ in the Reaction $\pi^- p \rightarrow \pi^+ \pi^- n$ from 500 to 700 MeV (Ph. D. Thesis) UCRL-16282 (unpublished).

19. T. J. Devlin, OPTIK: An IBM 709 Computer Program for the Optics of High Energy Particle Beams, UCRL-9729 (unpublished).

20. C. H. Moore, S. K. Howry, H. S. Butler (Stanford Linear Accelerator Center, Stanford, California) (private communication) 1963.

21. J. Kirz (Lawrence Radiation Laboratory, Berkeley) (private communication) 1963.

22. Lawrence Radiation Laboratory Counting Handbook, UCRL-3307 (unpublished).

23. B. Rossi, op. cit., p. 68.

24. R. R. Wilson, Phys. Rev. 86, 261 (1952).

25. Charles Rey (Lawrence Radiation Laboratory, Berkeley)(private communication) 1965.

26. W. Heitler, The Quantum Theory of Radiation, (University Press, Oxford, 1954), Third Ed., p. 262.

27. a. J. Orear, Notes on Statistics for Physicists, UCRL-8417, (unpublished).

    b. P. Cziffra and M. J. Moravcsik, A Practical Guide to the Method of Least Squares, UCRL-8523 (unpublished).

28. V. Z. Peterson (University of Hawaii, Department of Physics) (private communication) 1965.

29. L. Bertanza, P. L. Connolly, B. B. Culwick, F. R. Eisler, T. Morris, R. Palmer, A. Prodell, and N. P. Samios, Phys. Rev. Letters 8, 332 (1962).

30. R. R. Wilson, Phys. Rev. 84, 100 (1951).

31. V. V. Barmin, A. G. Dolgolenko, Yu. S. Krestnikov, A. G. Meshkovskii, and V. A. Shebanov, Sov. Phys. JETP, 19, 102 (1964).

32. O. Guisan, J. Kirz, P. Sonderegger, A. V. Stirling, P. Borgeaud, C. Bruneton, P. Falk-Vairant, B. Amblard, C. Caversasio, J. P. Guillaud, and M. Yvert, Phys. Letters 18, 200 (1965).

33. H. Faissner, F. Ferrero, H. J. Gerber, M. Reinharz, and J. Stein, Phys. Letters 11, 178 (1964).

34. F. Bruyant, M. Goldberg, G. Vegni, H. Winzeler, P. Fleury, J. Huc, R. Lestienne, G. DeRosny, and R. Vanderhaghen, Phys. Letters 12, 278 (1964).

35. M. Meer, R. Strand, R. Kraemer, L. Madansky, M. Nussbaum, A. Pevsner, C. Richardson, T. Toohig, M. Block, S. Orenstein and T. Fields, Proceedings of the International Conference on High Energy Physics at CERN, (1962) p. 103.

36. E. Pauli, A. Muller, R. Barloutaud, L. Cardin, J. Meyer, M. Beneventano, G. Gialanella, L. Paoluzi, and R. Finzi, Proceedings of the Sienna International Conference on Elementary Particles, Vol. 1, p. 92 (1963). This group also gave a paper at the 1964 Dubna Conference, but I have not yet seen those results.

37. Brandeis-Brown-Harvard-M.I.T.-Padua Collaboration, Phys. Rev. Letters 13, 486 (1964).

38. C. Calvelli, P. Kusstatscher, L. Guerriero, C. F. Voci, F. Waldner, I. A. Pless, L. Rosenson, G.A. Salandin, F. Bulos, R. Lanou, and A. Shapiro, Rev. Sci. Instr. 35, 1642 (1964).

39. T. Toohig, R. Kraemer, L. Mandansky, M. Meer, M. Nussbaum, A. Pevsner, C. Richardson, R. Strand, and M. Block, Proceedings of the International Conference on High Energy Physics at CERN p. 99 (1962).

40. J. M. Blatt and V. F. Weisskopf, Theoretical Nuclear Physics, (John Wiley and Sons, Inc., New York, 1952) p. 394.

41. J. Ashkin, Nuovo Cimento Suppl. 14, 221 (1959).

42. P. Auvil and C. Lovelace, πp Phenomenology, 300 - 1300 MeV, Physics Dept. Imperial College, London, Report ICTP/64/37 (1964) (unpublished).

43. C. A. Heusch, C. Y. Prescott, E. D. Bloom, and L. S. Rochester,

Photoproduction of Eta Mesons around 1 BeV, CALT-68-64 (unpublished); paper presented at the International Symposium on Electron and Photon Interactions at High Energies, June 8-12, 1965, Hamburg.

44. G. Altarelli, F. Buccella, and R. Gatto, Nuovo Cimento 35, 331 (1965).

45. S. F. Tuan, Phys. Rev. 139B, B1393 (1965).

46. W. R. Frazer and A. W. Hendry, Phys. Rev. 134B, B1307 (1964).

47. J. S. Ball and W. R. Frazer, Phys. Rev. Letters 7, 204 (1961).

48. P. N. Dobson, Zero Effective Range Analysis of Pion-Nucleon Reactions Near the η^0 Production Threshold, University of Hawaii Report HEPG-5-65, (unpublished) (1965).

49. F. Uchiyama-Campbell, Phys. Letters 18, 189 (1965).

50. A. W. Hendry and R. G. Moorhouse, Physics Letters 18, 171 (1965).

51. a. D. Berley, P. L. Connolly, E. L. Hart, D. C. Rahm, D. L. Stonehill, B. Thevenet, W. J. Willis, and S. S. Yamamoto, Threshold Phenomena in the Reaction $K^-p \to \Lambda\eta$, *Proceedings of the Dubna International Conference on High Energy Physics, Dubna, USSR,* (1964) (to be published). Also, BNL-8233, (unpublished).

    b. D. Berley, P. L. Connolly, E. L. Hart, D. C. Rahm, D. L. Stonehill, B. Thevenet, W. J. Willis and S. S. Yamamoto, Phys. Rev. Letters 15, 641 (1965).

52. I. P. Gyuk and S. F. Tuan, Phys. Rev. Letters 14, 121 (1965).

53. J. D. Jackson, *Classical Electrodynamics* (John Wiley and Sons, Inc. New York, 1962) p. 69.